공학박사 학위논문

Isogeometric Shape Design Optimization of Continuum-Nanoscale Structures considering Size Effects

크기 효과를 고려한 연속체-나노스케일 구조물의 아이소-지오메트릭 형상 최적설계

2016년 8월

서울대학교 대학원

산업·조선공학부

안 승 호

Isogeometric Shape Design Optimization of Continuum-Nanoscale Structures considering Size Effects

크기 효과를 고려한 연속체-나노스케일 구조물의
아이소-지오메트릭 형상 최적설계

지도 교수 조 선 호

이 논문을 공학박사 학위논문으로 제출함
2016년 7월

서울대학교 대학원
산업·조선공학부
안 승 호

안승호의 공학박사 학위논문을 인준함
2016년 7월

위 원 장 _____ (인)

부위원장 _____ (인)

위 원 _____ (인)

위 원 _____ (인)

위 원 _____ (인)

Isogeometric Shape Design Optimization of Continuum-Nanoscale Structures considering Size Effects

by

Seung-Ho, Ahn

A dissertation submitted for the degree of

DOCTOR OF PHILOSOPHY

in the

Department of Industrial Engineering and Naval Architecture

of

SEOUL NATIONAL UNIVERSITY, KOREA

August 2016

Abstract

Seung-Ho Ahn
Department of Industrial Engineering and Naval Architecture
College of Engineering
Seoul National University

Recently, in both academic and industrial environment including naval architecture and ocean engineering, atomistic level design and analysis is essential to overcome the limitations in conventional continuum based approach. Conventionally, molecular dynamics (MD) simulation is used to obtain the physical properties and behaviour of atomistic level structures. However, the applications of MD simulation are restricted by its excessive computational time. Especially the limitation of MD simulation is more obvious in shape design optimization field. It is difficult to apply continuum-based shape design sensitivity analysis which is essential for shape design optimization due to the discrete nature of shape variations at the atomic level of MD simulation. Shape design optimization scheme requires repeated analysis process, which requires tremendous computational cost.

In the thesis, an isogeometric shape design optimization method considering size effects in nanoscale structures is developed. We introduced continuum based model considering size effects for the analysis of nanoscale structures. Surface elasticity incorporating surface effects developed by Gurtin and Murdoch (1975) and nonlocal theory developed by Eringen (1983) are introduced, respectively. For experimental validation of developed method, three-point bending test of silver nanowires using atomic force microscope (AFM) are performed. Shape design optimization of curved structures is performed using continuum based Naghdi shell formulation in numerical examples. Isogeometric analysis (IGA) framework is used for numerical analysis method. A direct differentiation method is employed for the DSA and the design variables are selected as the control

points defining the geometry for flexible modeling of free-form shell surfaces. Exact solutions derived from curved beam theory are presented to verify the numerical examples. It is shown that size effects affect the behaviour of the nanoscale structures and its optimal shape.

The influence of surface effects in nanoscale is shown through three-point bending test of silver nanowires using AFM instruments. The behaviours of nanowires obtained from experimental results are compared with those obtained from theoretical calculation and good agreement is observed between them. Not only the behaviour of nanowires but the design sensitivity is validated through experimental results. The design sensitivity values obtained from fitting curve of experimental data are compared with those obtained by DSA based on continuum formulation considering surface effects, and it shows fairy good agreement.

The isogeometric method has numerous advantages over the classical finite element analysis (FEA) due to its convenience of Non-Uniform Rational B-Spline (NURBS) basis functions. In the isogeometric method, the NURBS basis functions in CAD system are directly used in the response analysis, which enables an incorporation of exact geometry and higher continuity into the computational framework. Also, IGA provides more accurate design sensitivity for complex geometries including higher order geometric information such as normal vector and curvature. Especially for shell structures, exact geometry is more important issue and application of IGA gives more accurate computation results than FEA.

Keywords: Isogeometric analysis, Nanoscale, Size effects, Shape design sensitivity, Shape design optimization, Experimental validation

Student number : 2009-21131

Table of Contents

List of Tables

List of Figures

Nomenclature

ξ	Knots
Ξ	Set of knots
R_i^p	NURBS basis function
$\mathbf{B}_i$	Control point
Ω	Open domain
$\mathbf{b}$	Body force
T_x, T_z	Traction on the surface
E	Young's modulus
E_{eff}	Effective Young's modulus
G	Shear modulus
ν	Poisson's ratio
μ_0, λ_0	Surface Lame constants
τ_0	Residual surface stress
σ_{ij}	Stress tensor
$\tau^{\alpha\beta}$	Surface stress tensor
μ	Nonlocal parameter
$\mathbf{n}$	Normal vector
$\mathbf{V}$	Shape design velocity field
N	Axial force

M	Bending moment
Q	Shear force
κ	Shear correction factor
D	Diameter of circular cross section
A	Area of circular cross section
I	Second moment of inertia
$\mathbf{E}^n$	n-dimensional Euclidean space
$\mathbf{R}^n$	n-dimensional Vector space
$\mathbf{a}^3$	Surface unit normal vector
$\mathbf{a}_\alpha$	Covariant basis vector
$\mathbf{a}^\alpha$	Contra variant basis vector
u_α	In-plane displacement measure
w	Out-of-plane displacement measure
ψ_α	Rotational angle measure
$b_{\alpha\gamma}$	Covariant curvature tensor
b_α^γ	Mixed curvature tensor
$\Gamma_{\alpha\beta}^\mu$	Christoffel symbol
$\varepsilon_{\alpha\beta}$	Strain measure of membrane part
$\omega_{\alpha\beta}$	Strain measure of bending part
γ_α	Strain measure of shear part
a	Determinant of the metric tensor

Chapter 1. Introduction

1.1 Motivation

Recently, construction of nanoscale structures became possible due to the development of MEMS (Micro Electro Mechanical Systems) and NEMS (Nano Electro Mechanical Systems) technologies. Nanoscale structures such as resonator, mass sensor and bio-chemical sensor are used in numerous engineering fields and they are expected to be used more widely in the near future. Especially, in naval architecture and ocean engineering, nanoscale technology is required for various applications. For instance, organisms such as algae and barnacles sticking on the lower structure of large sized ships influence the propulsion power by increasing the ship resistance. By releasing of several biocides embedded in a film forming nanocomposites, antifouling can be achieved by slowing the growth of subaquatic organisms as shown in figure 1.1-(a). Figure 1.1-(b) shows Danish Knud Rasmussen Class inspection ship in the ice region. Nano-based surfaces have the potential to completely preventing icing and ice can be removed from composite structures through the use of conductive carbon fibres in the composite. Nanotechnology is also applied for the application in shipbuilding such as nano fillers for enhancement, thermal barrier materials for engines, fuel cells, embedded sensors and cloaking for warship. (McGrail 2011) Especially, stress distribution near the nano-sized crack is observed in this paper. The behavior of crack initiation and its growing process is very crucial for the safety of ship and marine structures. Also, the observation on the behavior of nano-sized beam and shell structures can be used for the study of mechanical polishing on the surface of ship and marine structure. To obtain the physical properties and behavior of nanoscale structures, MD

simulation is used conventionally. MD simulation is a computer simulation of physical movements of atoms and molecules using inter-atomic potential. Therefore, accurate analysis including the information at the atomic scale is possible, which is not able to be handled using conventional continuum based approach. Even though MD simulation of nanoscale structures can give accurate results, they are computationally expensive for systems with practical structures having relatively large sizes.

To overcome the difficulty of computational cost in MD simulation, continuum based formulations of nanoscale structures have been developed. A nanoscale structure is assumed as one of the continuum model and numerical analysis method such as FEA is applied to analyze the continuum model. Although the conventional continuum models provide simple formulas and have advantage on computational time, applying these continuum models directly to practical model is questionable due to the size effects. Size effects in this research mean material properties are influenced by the effect of small size range. Material properties change as the thickness or total volume of the structure decrease to nanometer range. To analyze nanoscale structures based on continuum model considering size effects, the conventional elasticity theory has been extended from various viewpoints such as surface elasticity theory (Gurtin and Murdoch 1975), nonlocal theory (Eringen 1983), strain gradient elasticity (Lam et al. 2003) and couple stress theory (Mindlin and Tiersten 1962). In this research, surface elasticity incorporating surface effects developed by Gurtin and Murdoch (1975) and nonlocal theory developed by Eringen (1983) are used to develop shape optimization scheme for nanoscale structures.

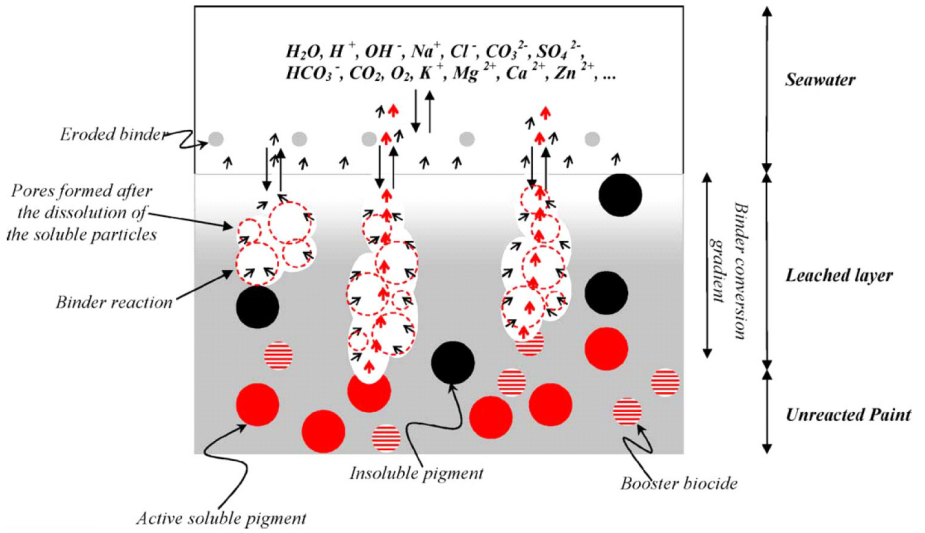

(a) Antifouling of organisms using nanoparticles (Yebra et al. 2004)

(b) Anti-icing technology using nano-composites used in Danish Knud Rasmussen class inspection ship (Ryerson 2013)

Figure 1.1 Examples of nanotechnologies in naval architecture and ocean engineering

The continuum mechanics models for nanoscale structures are also advantageous in structural optimization areas. Because most optimization schemes require repeated analysis process, applying MD simulation which requires large computational cost to the optimization process is almost impossible. Furthermore, it is difficult to apply continuum-based shape DSA which is essential for shape optimization to the methodology based on MD simulation due to the discrete nature of shape variations at the atomic level. To overcome the difficulty of discrete nature in atomic structures, Jang and Cho (2015) transformed the discrete spatial variation into a non-shape variation of the GLE system. However, well-developed conventional shape optimization schemes can be applied directly for nanoscale structures regardless of discrete nature in atomic structures by using developed method.

1.2 Literature survey

1.2.1 Experimental validation of size effects in nanoscale

Some researchers show that size effects exist in nanoscale structures through MD simulation or experiments. They also verified these size effects can be explained by continuum-based theory considering surface effects or nonlocal effects.

Molecular dynamics simulation

Miller and Shenoy (2000) and Dingreville et al. (2005) showed that material properties have size dependence due to the increasing importance of surfaces as the scale of structures become comparable with the atomic scale. Figure 1.2 shows variation of plate modulus with respect to thickness.

Miller and Shenoy (2000) also showed that continuum formulations of plate in the nanoscale are reliable by comparing with MD simulation results. However, it is observed that accuracy is somewhat decreased in considering bending energy. Wang et al. (2010) showed that decreased accuracy can be improved by considering residual surface stress in the formulation. Jin and Yuan (2005a, b) discussed the macroscopic fracture parameters from both MD simulation and the continuum model, indicating that the near-tip stress calculated from MD simulation agrees well with the continuum one. Tsai and Sie (2015) compared the maximum stress of crack tip problem obtained by MD simulation with that obtained by nonlocal elasticity. It was shown that there is a good agreement between them.

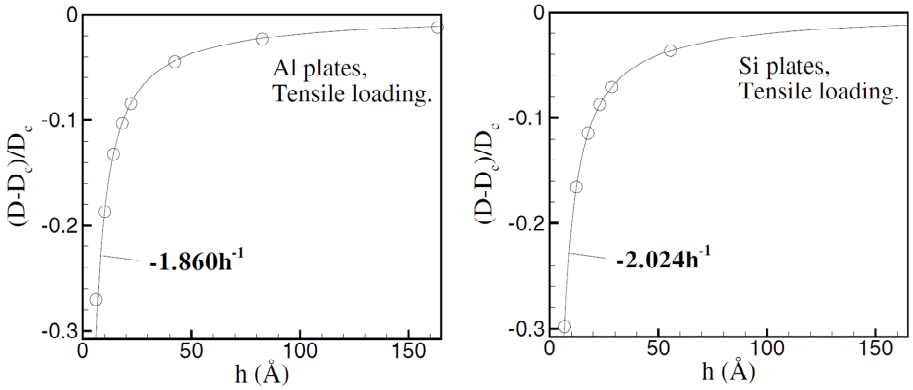

(a) Al plates (b) Si plates

Figure 1.2 Variation of plate modulus with respect to thickness

Three-point bending test using AFM

Development of AFM facilitates three-point bending test in nanoscale. Some researchers discovered size effects in nanoscale through three-point bending test using AFM, and analyzed the experimental results using several continuum-based theories considering size effects.

In order to account for the size-dependent mechanical properties, some researchers applied strain gradient theory. Li et al. (2009) pointed out that Eringen's nonlocal theory is not adequate for three-point bending test of nanowire. Nonlocal theory does not capture the variation of area and size effects cannot be predicted for bending of a nanobeam under a concentrated force, which is called paradox. They suggested two second-order material constants to describe the size effect for nanowires. Developed theoretical predictions for Young's modulus of CNTs are in consistence with the corresponding three-point bending experimental results by other researchers.

There have been many researchers who applied surface effects theory to explain the size effects of the nanowire. Cuenot et al. (2004) analyzed the elastic properties of silver and lead nanowires using three-point bending test as shown in figure 1.3-(a). The elastic properties of the silver nanowires with outer diameters ranging from 20 to 140 nm were measured using AFM. The size dependence of the Young's modulus is discussed using surface effects theory. Jing et al. (2006) measured elastic properties of the silver nanowires with outer diameters ranging from 20 to 140 nm using AFM as shown in figure 1.3-(b). They showed the size dependence of the apparent Young's modulus of the silver nanowires is attributed to the surface effect.

He et al. (2008) analyzed the mechanical behavior of silver nanowires using Euler-Bernoulli beam theory via the Young-Laplace equation. They derived deflection of the beam and obtained effective Young's modulus considering size effects. Derived solutions agree well with size dependent Young's moduli observed from three-point bending tests by other researchers. Chiu and Chen (2011) suggest higher-order surface stress which considers not only the effect of in-plane membrane surface stresses, but also the surface moments induced from the non-uniform surface stress across the

layer thickness. It allows that the stress could be linearly varying across the layer thickness, which results in surface stress as well as surface moment. They show that developed method predicts more accurate results with the experimental data reported by Jing et al. (2006) compared with original method without high-order surface stress. Some other researchers also extended the Gurtin-Murdoch theory to account for the flexural resistance. Steigmann and Ogden (1999) point out that Gurtin-Murdoch theory cannot be used for a compressive stress-state and in particular surface wrinkling or roughening. They incorporate intrinsic flexural resistance of a surface to overcome aforementioned issues. Chhapadia et al. (2011) introduce a simplified and linearized version of a theory proposed by Steigmann and Ogden (1999) to capture curvature-dependence of surface energy. They propose an unambiguous definition of the thickness of a crystalline surface. Hu et al. (2014) discuss that the thickness of surface layer is related to such factors as defects, surface roughness, loading conditions and experimental temperature. They suggest core-shell model to depict the size effect of Young's modulus. The effect of high order surface stress with experimental data will be discussed clearly in chapter 4.1.3.

Many researchers have discussed the mechanical behavior of nanoscale structures using three-point bending test. However, as far as authors know, research on experimental validation of DSA is limited. The design sensitivity values obtained from fitting curve of experimental data are compared with those obtained by DSA based on continuum formulation considering surface effects. Manufacturing structures with variation in nanoscale for obtaining adjacent experimental data is not easy due to the limitation of manufacturing techniques. In this research, we performed three-point bending test of silver nanowires having various diameter and length as far as possible. In this way,

DSA based on continuum-based theory considering size effects can be validated.

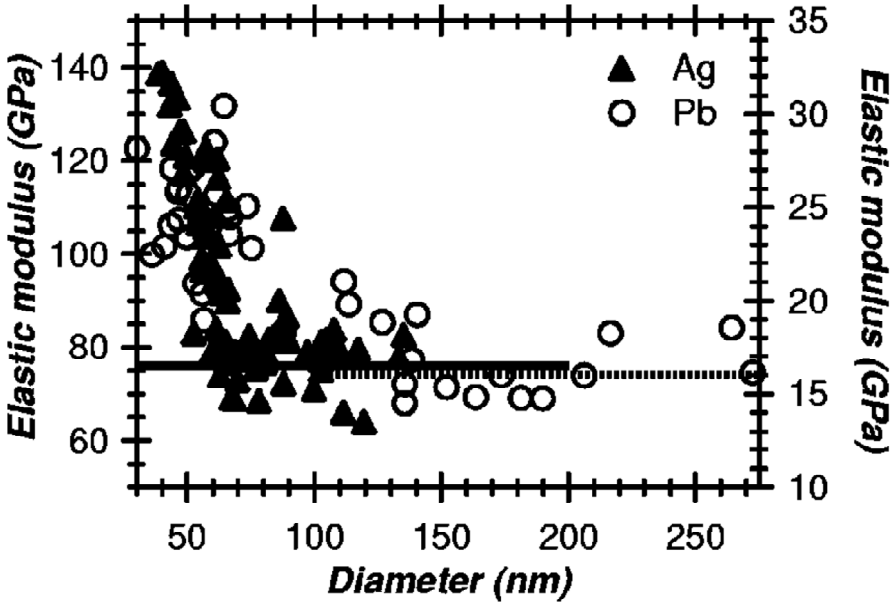

(a) Young's modulus obtained by Cuenot et al. (2004)

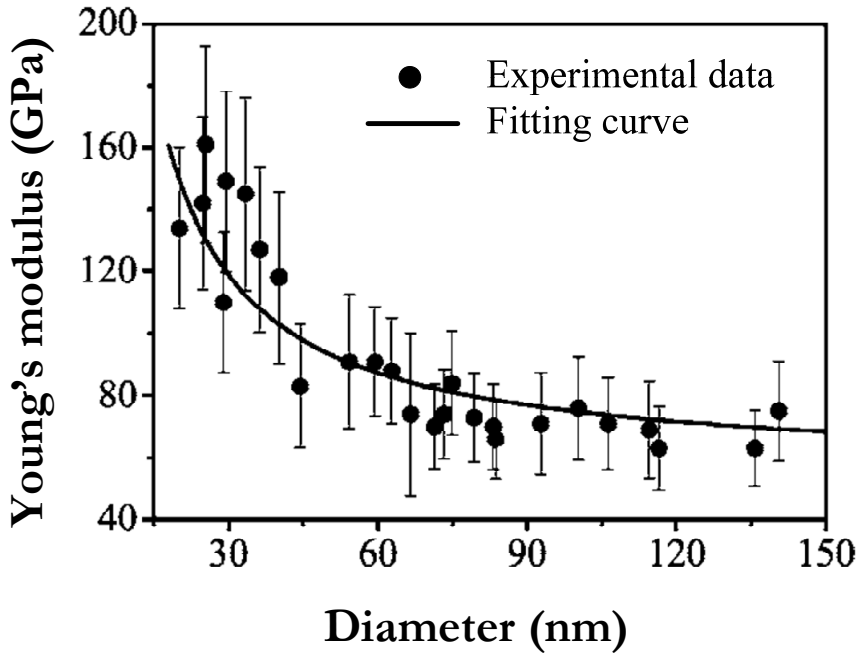

(b) Young's modulus obtained by Jing et al. (2006)

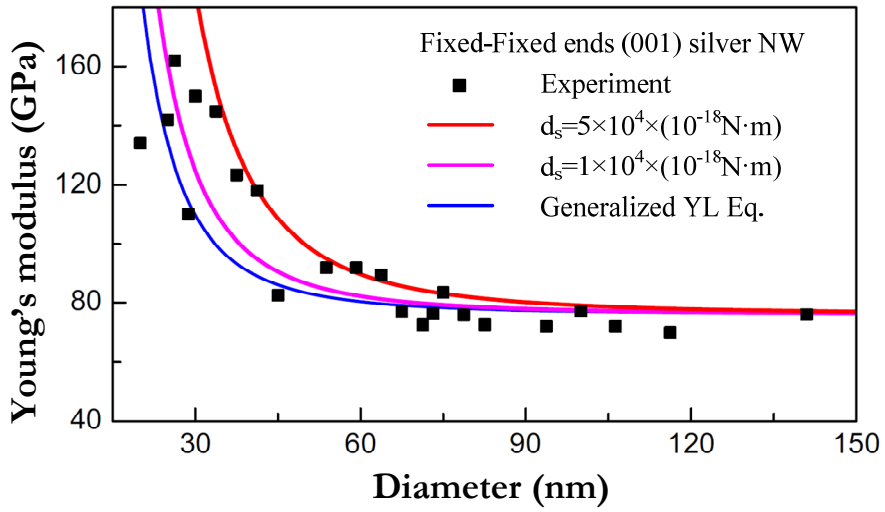

(c) Effect of high order surface stress (Chiu and Chen 2011)

Figure 1.3 Variation of the measured Young's modulus of silver nanowires

1.2.2 Isogeometric framework

Finite element analysis which is one of widely used numerical analysis method has difficulties in dealing with curved structures due to geometric approximation which is inherent in the finite element mesh. IGA framework is introduced to overcome this difficulty. Hughes et al. (2005) developed IGA method, which is an analysis framework employing the same basis function as used in the CAD system. It enables the seamless incorporation of higher order continuity and exact geometry such as curvature and normal vector into the computational framework. IGA provides a more accurate sensitivity of complex geometries including higher order geometric information such as normal vector and curvature. The higher order NURBS functions offer a more compact representation of response than FEA. Therefore, it is possible for IGA to obtain a more accurate computation results than FEA, even with less DOFs. Further, Cho and Ha (2009)

performed shape optimization based on IGA and showed that IGA could prevent the loss of higher-order geometric information, such as normal and curvature in design sensitivity expressions. Also, developed isogeometric shape optimization scheme applied to the area such as heat conduction (Yoon and Cho 2013), crack propagation problem (Choi and Cho 2014) and built up structures (Lee and Cho 2015).

Some researchers extended the IGA for micro or nano scale problems considering size effects. Fischer et al. (2011) extended IGA towards the numerical solution of the problem of gradient elasticity in two dimensions for representing size effects. Introduction of higher order gradients of the strains into the constitutive relation requires partial differential equation of higher order. NURBS in IGA naturally includes higher order continuity of the approximation of the displacements and the geometry. Rudraju et al. (2014) introduced IGA for three-dimensional solutions using finite strain gradient elasticity. They solved problems on martensitic microstructures with size effects driven by non-convex free energy in strain space.

1.2.3 Curved structures in nanoscale

Curved structures are generalized form in nanoscale and curved graphene is one example to show the importance of curvature in nanoscale structures. Graphene is a one-atom-thick planar sheet of carbon atoms, densely packed together into a honeycomb shaped crystal lattice. Several methods to make graphene are developed and recently Kosynkin et al. (2009) produced graphene nanoribbons structures by lengthwise cutting and unravelling of multi-walled carbon nanotube side walls as shown in figure 1.4-(a), and it shows high crystallinity and interesting semimetal electronic

properties. The curved graphene obtained by unzipping carbon nanotubes is intermediate structure between flat graphene sheet and carbon nanotube. Some researchers show that curvature of the curved graphene affects the properties of the graphene. It is shown that the curvature of the graphene changes the electron density, so the electrical properties can be improved. (Kolesnikov and Osipov, 2008) Gosálbez et al. (2011) discusses that curved graphene with constant curvature is generated by unzipping carbon nanotubes as shown in figure 1.4-(b), and the curvature affects the spin-orbit coupling and bandwidth. In this way, since the curvature of nanoscale structures fairly affect the properties of the structure, the representation of exact geometry and the accurate prediction of mechanical behaviors in continuum modeling are highly significant. In this paper, to analyze the curved structure in nanoscale such as curved graphene, continuum shell formulations considering size effects are introduced based on IGA framework.

Surface elasticity is applied to the modeling of shells by other researchers. Gurtin and Murdoch (1975) modeled the interfacial surface as a membrane, but we modeled the interfacial surface as a shell as in Steigmann and Ogden (1999). Altenbach and Eremeyev (2011) discussed the derivation of the governing nonlinear shell equations considering surface effects. Zhang et al. (2014) presented general equations of piezoelectric shells considering surface effects in an orthogonal curvilinear coordinate system. Nonlocal theory is also applied to the modeling of shells by other researchers. Hu et al. (2008) discussed that the wave dispersion predicted by the nonlocal elastic shell theory shows good agreement with that of the MD simulation results. Nonlocal parameter is determined based on the MD result to predict the dispersion of transverse wave in CNTs through the nonlocal shell models.

Arash and Ansari (2010) studied vibration characteristics of single-walled carbon nanotubes (SWCNTs) with different boundary conditions subjected to initial strain based upon a nonlocal shell model accounting for the small-scale effects.

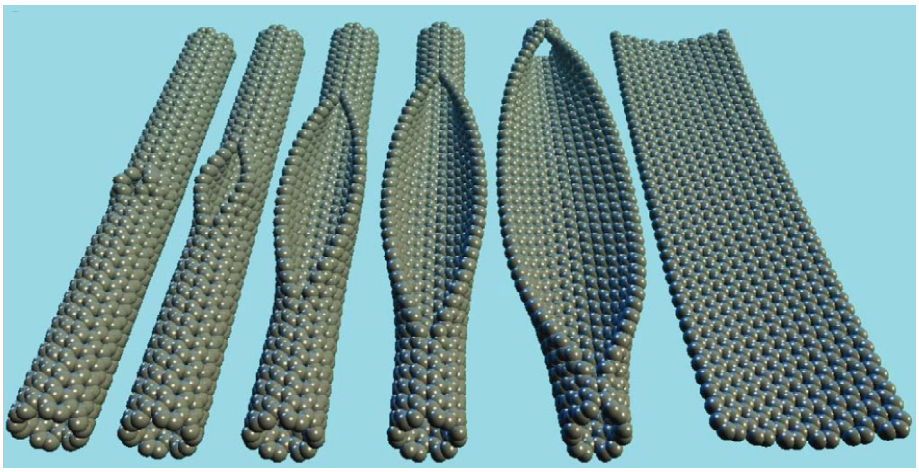

(a) Gradual unzipping of one wall of a carbon nanotube to form a graphene (Kosynkin et al. 2009)

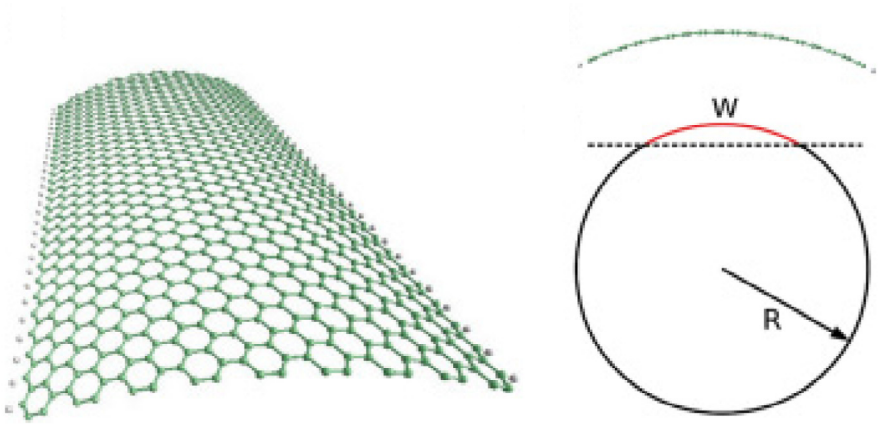

(b) Obtaining a curved graphene as fraction of a nanotube (Gosálbez et al. 2011)

Figure 1.4 Generation of a curved graphene from a nanotube

1.2.4 Design optimization in nanoscale

Some continuum based optimization methods considering nanoscale effects have been presented in recent year. Evgrafov et al. (2009) considered the kinetic theory to topology optimization of heat conducting devices at nano-scale as shown in figure 1.5. An average distance travelled by a particle between collisions with other particles is considered in continuum formulation to consider nano scale effects. Nanthakumar et al. (2015) introduced a coupled XFEM/level set methodology to perform topology optimization of nanostructures considering nanoscale surface effects as shown in figure 1.6. They showed different optimal topology by considering surface effects, but physical interpretations for the obtained optimal topology under nanoscale are not presented. Glavardanov et al. (2012) deals with optimal shapes against buckling of an elastic beams considering nonlocal effects, but they only deals with optimization problems with cross sectional areas which are sizing variables.

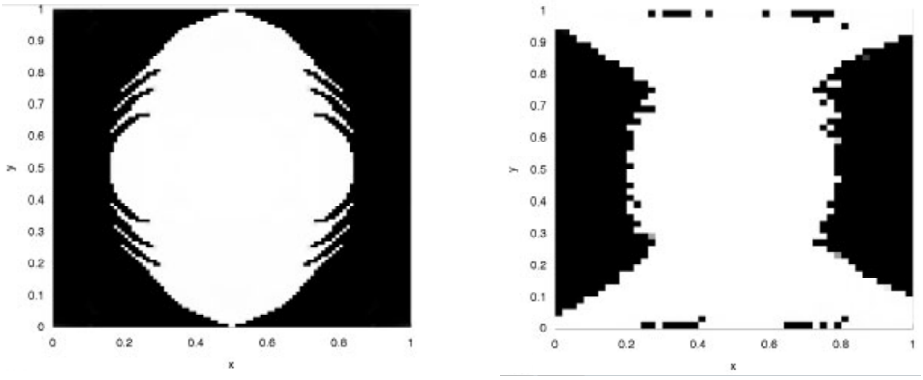

(a) Without kinetic theory (b) With kinetic theory

Figure 1.5 Different optimal material distributions by considering kinetic theory (Evgrafov et al. 2009)

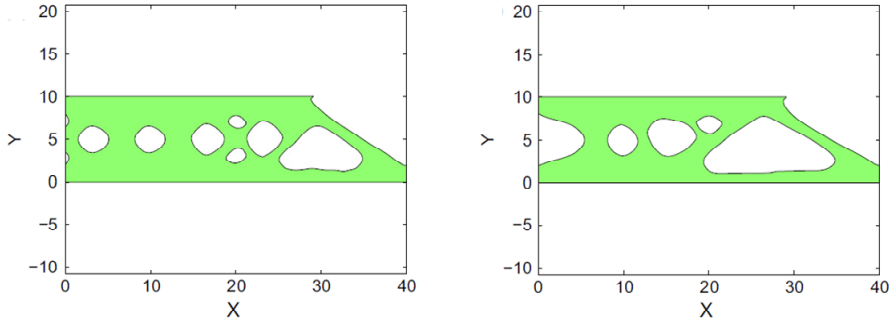

(a) Without surface effects (b) With surface effects

Figure 1.6 Different optimal topology by considering surface effects (Nanthakumar et al. 2015)

1.2.5 Organization of thesis

The paper is organized as follows: in Chapter 2, we explain the equilibrium equations of beam and shell theory considering size effects based on IGA, respectively. In this research, surface elasticity incorporating surface effects developed by Gurtin and Murdoch (1975) and nonlocal theory developed by Eringen (1983) are introduced, respectively. In Chapter 3, isogoemetric shape DSA formulation of beam and shell with size effects is given, respectively. A direct differentiation method is employed for the DSA and the design variables are selected as the control points defining the geometry for flexible modeling of free-form shell surfaces. In Chapter 4, three-point bending test of silver nanowires are given to validate developed method. Also, the influence of size effects for the numerical solution is shown and it is verified through exact solutions. Shape optimization problems minimizing strain energy are given and the optimal solutions are verified through exact optimal solution. Finally, we draw some conclusions, which present the importance of the proposed method.

Chapter 2. Isogeometric Analysis considering Size Effects

2.1 NURBS basis function

In the IGA, we use same NURBS basis functions to represent solution space and geometry. Consider a set of knots ξ in an *n*-dimensional parametric space. In the one-dimensional case, it is written as

$$\xi = \{\xi_1, \xi_2, \cdots, \xi_{n+p+1}\}, \tag{2.1}$$

where *p* and *n* are the order of the basis function and the number of control points, respectively. The B-spline basis functions can be defined, recursively, as

$$N_i^0(\xi) = \begin{Bmatrix} 1 & if\ \xi_i \le \xi \le \xi_{i+1} \\ 0 & otherwise \end{Bmatrix} \quad (p=0) \tag{2.2}$$

and

$$N_i^p(\xi) = \frac{\xi - \xi_i}{\xi_{i+p} - \xi_i} N_i^{p-1}(\xi) + \frac{\xi_{i+p+1} - \xi}{\xi_{i+p+1} - \xi_{i+1}} N_{i+1}^{p-1}(\xi), (p = 1,2,3,\cdots,). \tag{2.3}$$

A general quadratic B-spline basis functions are shown in figure 2.1.

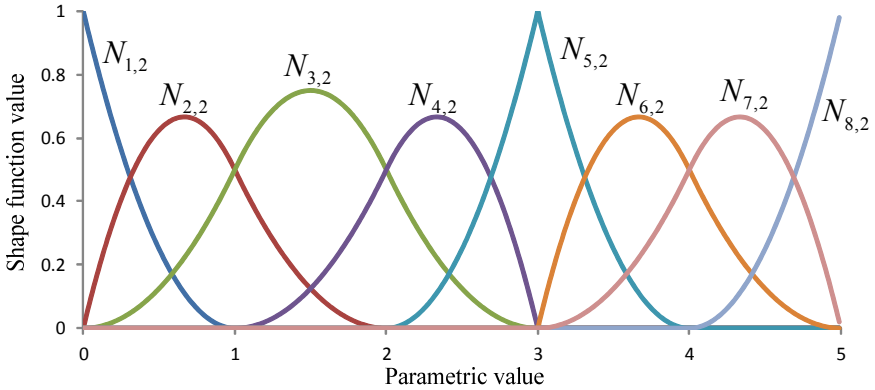

Figure 2.1 Quadratic B-spline basis functions, **Ξ**={0,0,0,1,2,3,3,4,5,5,5}

The shape functions are completely different from those in the FEM and guarantee p-1 continuous derivatives. The B-spline has some useful properties as a basis function such as partition of unity, compactness and non-negativity. Using the B-spline basis function $N_i^p(\xi)$ and weight w_i, the NURBS basis function $R_i^p(\xi)$ is defined as

$$R_i^p(\xi) = \frac{N_i^p(\xi) w_i}{\sum_{j=1}^{n} N_j^p(\xi) w_j}. \tag{2.4}$$

For the given l pairs of the p-th order NURBS basis function R_i^p and the corresponding control point $\mathbf{B}_i$, the NURBS curve $\mathbf{C}$ is obtained as

$$\mathbf{C}(\xi) = \sum_{i=1}^{l} R_i^p(\xi) \mathbf{B}_i. \tag{2.5}$$

Similarly, NURBS surface $\mathbf{S}$ is defined as a tensor product of coordinates,

$$\mathbf{S}(\boldsymbol{\Xi}) = \sum_{i=1}^{l} \sum_{j=1}^{m} R_i^p(\xi,\eta) R_j^q(\xi,\eta) \mathbf{B}_{i,j} = \sum_{I}^{CP} W_I(\boldsymbol{\Xi}) \mathbf{B}_I, \tag{2.6}$$

where $\mathbf{B}_I = \mathbf{B}(\mathbf{x})$ are locations of the control points and W_I is introduced for the brevity of expression. CP denotes the number of control points and $\boldsymbol{\Xi}$ is the parametric domain of surface.

2.2 Beam structures considering surface effects

Nanoscale beam with circular cross section is considered as shown in Figure 2.2. The Bernoulli-Euler beam is considered and shear effect is ignored. A beam based on surface elasticity is considered to have an elastic surface bonded to its bulk part. Due to the interaction between the surface and bulk material, the traction T_x and T_z exist on the surface.

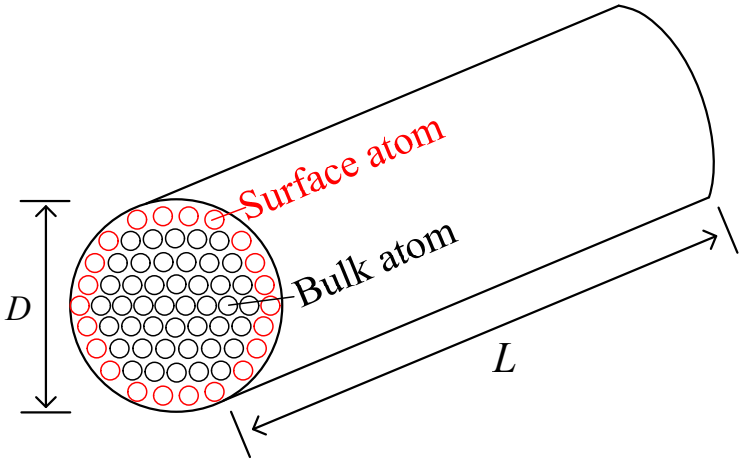

Figure 2.2 Cross sectional view of circular beam

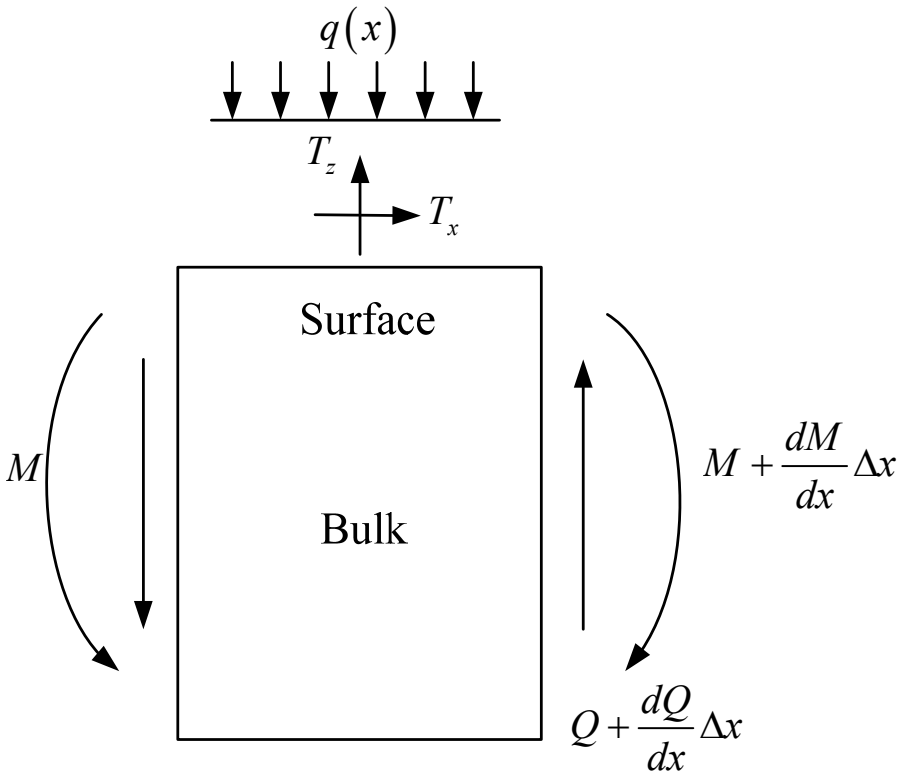

Figure 2.3 Free-body diagram of incremental beam element

The bending moment and vertical force equilibrium equations of the element shown in figure 2.3 are obtained as

$$\frac{d^2M}{dx^2}+\frac{d}{dx}\int_s T_x z ds = q(x)+\int_s T_z ds \tag{2.7}$$

where M is bending moment, $q(x)$ is distributed vertical force and s is the perimeter of the cross section. Bending moment M is defined as

$$M=\int_A \sigma_{xx} z dA=\int_A \left(Ez\frac{\partial^2 w}{\partial x^2}\right) z dA = EI\frac{\partial^2 w}{\partial x^2} \tag{2.8}$$

where I is obtained as $\pi D^4/64$ for a circular cross section, D is a diameter of circular cross section. The surface constitutive relations are obtained as

$$\tau_{xx}=\tau_0+(2\mu_0+\lambda_0)u_{x,x} \tag{2.9}$$

and

$$\tau_{nx}=\tau_0 w_{,x} \tag{2.10}$$

where μ_0 and λ_0 are surface Lame constants and τ_0 is the residual surface stress under unstrained conditions. $\tau_0 w_{,x}$ given in equation (2.10) is distributed transverse force along the beam longitudinal direction caused by generalized Young-Laplace equation, which accounts for out of plane stresses induced from residual surface stress and curvature in deformed shape of a beam. (Chen et al. 2006) Using the equations (2.9) and (2.10), the equilibrium relations for the surface are expressed as

$$T_x=\tau_{xx,x}=(2\mu_0+\lambda_0)\frac{\partial^2 w}{\partial x^2}z \tag{2.11}$$

and

$$T_z=\tau_{nx,x}n_z=\tau_0\frac{\partial^2 w}{\partial x^2}n_z \tag{2.12}$$

Chiu and Chen (2011) suggest that higher-order surface stress which considers not only the effect of in-plane membrane surface stresses, but also the surface moments induced from the non-uniform surface stress across the

layer thickness. Therefore, equation (2.12) is rewritten as

$$T_z = \left(\tau_0 \frac{\partial^2 w}{\partial x^2} + d_s \frac{\partial^2 m^s}{\partial x^2} \right) n_z = \left(\tau_0 \frac{\partial^2 w}{\partial x^2} + d_s \frac{\partial^4 w}{\partial x^4} \right) n_z \tag{2.13}$$

where m^s is surface moment and d_s is surface bending stiffness parameter. High-order term with respect to deflection w is considered with d_s term. Substituting equations (2.8)-(2.13) into equation (2.7) yields

$$\left\{ EI + \frac{\pi D^3}{8} E_s + 2 d_s D \right\} \frac{\partial^4 w}{\partial x^4} = q(x) - 2\tau_0 D \frac{\partial^2 w}{\partial x^2} \tag{2.14}$$

where E_s is $2\mu_0+\lambda_0$. From equation (2.14), following governing equilibrium equation is obtained as

$$EI^* \frac{\partial^4 w}{\partial x^4} + 2\tau_0 D \frac{\partial^2 w}{\partial x^2} = q(x) \tag{2.15}$$

where EI^* is defined as $EI+(\pi D^3/8)E_s+2d_sD$. Equation (2.15) is multiplied by an weight functions $\bar{w}$ and integrated over the structural domain to obtain

$$\int_0^L \left\{ EI^* \frac{\partial^4 w}{\partial x^4} + 2\tau_0 D \frac{\partial^2 w}{\partial x^2} - q(x) \right\} \bar{w} dx = 0 \tag{2.16}$$

where L is the length of the beam. Integrating equation (2.16) by part and applying the boundary conditions give the governing equation as

$$a_\Omega(\mathbf{z}, \bar{\mathbf{z}}) = l_\Omega(\bar{\mathbf{z}}), \ ^\forall \bar{\mathbf{z}} \in \bar{Z}, \tag{2.17}$$

where the bilinear strain energy and load linear forms are obtained as

$$a_\Omega(\mathbf{z}, \bar{\mathbf{z}}) = \int_0^L \left\{ EI^* \frac{\partial^2 w}{\partial x^2} \frac{\partial^2 \bar{w}}{\partial x^2} + 2\tau_0 D \frac{\partial w}{\partial x} \frac{\partial \bar{w}}{\partial x} \right\} dx \tag{2.18}$$

and

$$l_\Omega(\bar{\mathbf{z}}) = \int_0^L q(x) \bar{w} dx \tag{2.19}$$

$\bar{Z} \subset [H^2(\Omega)]^d$ is d-dimensional variational spaces of kinematically admissible displacements. Using an isoparametric mapping, approximated response and virtual response are expressed, in terms of NURBS basis functions and the response coefficients at control points, as

$$\mathbf{z}^h(\Xi) = \sum_I^{CP} W_I(\Xi)\mathbf{y}_I \tag{2.20}$$

and

$$\overline{\mathbf{z}}^h(\Xi) = \sum_I^{CP} W_I(\Xi)\overline{\mathbf{y}}_I, \tag{2.21}$$

where $\mathbf{z}^h \in Z^h \subset Z$ and $\overline{\mathbf{z}}^h \in \overline{Z}^h \subset \overline{Z}$. For brevity of notation for discrete response and function space, $\mathbf{z}$ and Z will be used instead of $\mathbf{z}^h$ and Z^h, hereafter. Also, same notation is applicable for the virtual ones. Using equations (2.20) and (2.21), the variational equation (2.17) is rewritten as

$$a_\Omega(\mathbf{z}, \overline{\mathbf{z}}) = l_\Omega(\overline{\mathbf{z}}), \ {}^\forall\overline{\mathbf{z}} = \sum_I^{CP} W_I(\Xi)\overline{\mathbf{y}}_I \in \overline{Z}, \tag{2.22}$$

where

$$a_\Omega(\mathbf{z}, \overline{\mathbf{z}}) = \int_x \sum_{I,K}^{CP} \overline{\mathbf{y}}_I^T \left\{ EI^* W_{I,xx}^T W_{K,xx} + 2\tau_0 D W_{I,x}^T W_{K,x} \right\} \mathbf{y}_K dx \tag{2.23}$$

and

$$l_\Omega(\overline{\mathbf{z}}) = \int_x \sum_I^{CP} \left(\mathbf{f}^T W_I \overline{\mathbf{y}}_I \right) dx, \tag{2.24}$$

where $\mathbf{f}$ is force component matrix. Detailed derivation on the beam formulation including surface stress may refer to He and Lilley (2008), Liu and Rajapakse (2010) and Chiu and Chen (2011).

2.3 Shell structures

2.3.1 Kinematics of deformation of shell

Consider a three-dimensional solid structure $\hat{\Omega}^*$ in domain $\mathbf{E}^3$ that is a three-dimensional Euclidean space. The space $\mathbf{E}^3$ is endowed with an orthonormal basis vectors $\hat{e}^j$. Let $\hat{x}_i^*$ denote the cartesian coordinates of a point $\hat{\mathbf{x}}^* \in \mathbf{E}^3$. Here, * means the domain or material point in thickness direction. Also, the space $\mathbf{R}^3$ is three-dimensional vector space in which

three vectors $\mathbf{e}^i \ (i=1,2,3)$ form a basis. Let there be given a domain $\hat{\Omega}^*$ of $\mathbf{E}^3$ and assume that there exist an domain Ω^* of $\mathbf{R}^3$ and an one-to-one mapping $\boldsymbol{\Theta}:\Omega^* \to \mathbf{E}^3$ such that $\boldsymbol{\Theta}(\Omega^*)=\hat{\Omega}^*$. Then each point $\hat{\mathbf{x}}^* \in \hat{\Omega}^*$ can be expressed as

$$\hat{\mathbf{x}}^* = \boldsymbol{\Theta}(\mathbf{x}^*),\ \mathbf{x}^* \in \Omega^*, \tag{2.25}$$

and the three coordinates $x_i^* \ (i=1,2,3)$ of $\mathbf{x}^* \in \mathbf{R}^3$ denote the curvilinear coordinates of the point $\hat{\mathbf{x}}^* \in \mathbf{E}^3$.

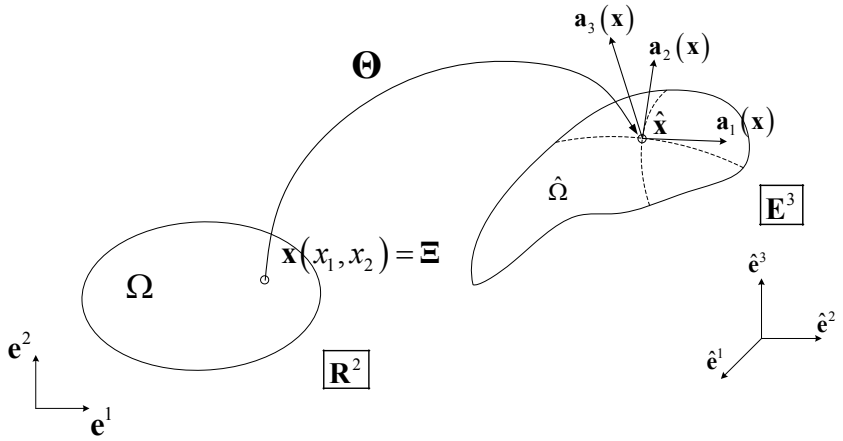

Figure 2.4 Definition of the middle surface of the shell

The middle surface of the shell is often represented by a surface geometry Ω, which uses two curvilinear coordinates (x_1,x_2) as shown in figure 2.4. Therefore, the reference domain Ω of the surface is composed of x_1 and x_2, while x_3 is the coordinate in thickness direction that is defined as $-0.5h \le x_3 \le 0.5h$ with h is the shell thickness. Thus, the material point $\hat{\mathbf{x}}^*$ of the undeformed shell is given as

$$\hat{\mathbf{x}}^*\left(x_1,x_2,x_3\right)=\hat{\mathbf{x}}\left(x_1,x_2\right)+x_3\mathbf{a}^3\left(x_1,x_2\right), \tag{2.26}$$

where $\hat{\mathbf{x}}(x_1,x_2)$ is the material point on the middle surface, and $\mathbf{a}^3(x_1,x_2)$ is the surface unit normal vector. The corresponding covariant basis vectors are

$$\mathbf{g}_\alpha=\hat{\mathbf{x}}^*_{,\alpha}=\left(\hat{\mathbf{x}}+x_3\mathbf{a}^3\right)_{,\alpha}=\mathbf{a}_\alpha+x_3\mathbf{a}^3_{,\alpha}, \tag{2.27}$$

in which $(\cdot)_{,\alpha}$ denotes partial differentiation with respect to the curvilinear coordinates x_α and Greek indices take values 1 and 2. $\mathbf{a}_\alpha$ and $\mathbf{a}^\alpha$ are covariant and contravariant basis vector on the middle surface, respectively. The covariant and contravariant components of the surface metric tensors are given as

$$a_{\alpha\beta}=\mathbf{a}_\alpha\cdot\mathbf{a}_\beta,\ a^{\alpha\beta}=\mathbf{a}^\alpha\cdot\mathbf{a}^\beta. \tag{2.28}$$

In the Naghdi's shell model, the displacement vector is assumed as

$$\hat{\mathbf{z}}^*=u_\alpha\mathbf{a}^\alpha+x_3\psi_\alpha\mathbf{a}^\alpha+w\mathbf{a}^3=\left(u_\alpha+x_3\psi_\alpha\right)\mathbf{a}^\alpha+w\mathbf{a}^3, \tag{2.29}$$

where u_α and w are in-plane and out-of-plane displacement measure and ψ_α are rotational angle measure. The membrane, bending, and shear strain measures are obtained as

$$\varepsilon_{\alpha\beta}=\frac{1}{2}\left(u_\alpha\|_\beta+u_\beta\|_\alpha-2b_{\alpha\beta}w\right), \tag{2.30}$$

$$\omega_{\alpha\beta}=\frac{1}{2}\left(\psi_\alpha\|_\beta+\psi_\beta\|_\alpha\right)-\frac{1}{2}b^\gamma_\alpha\left(u_\mu\|_\beta-b_{\beta\gamma}w\right)-\frac{1}{2}b^\gamma_\beta\left(u_\gamma\|_\alpha-b_{\alpha\gamma}w\right), \tag{2.31}$$

and

$$\gamma_\alpha=w_{,\alpha}+\psi_\alpha+b^\lambda_\alpha u_\lambda, \tag{2.32}$$

where $b_{\alpha\gamma}$ is covariant curvature tensor and b^γ_α is mixed curvature tensor. $(\cdot)_\alpha\|_\beta=(\cdot)_{\alpha,\beta}-\Gamma^\mu_{\alpha\beta}(\cdot)_\mu$ means covariant differentiation in which $\Gamma^\mu_{\alpha\beta}=\mathrm{a}_{\alpha,\beta}\cdot\mathrm{a}^\mu$ is christoffel symbol defined at the middle surface. These higher order geometric quantities such as christoffel symbol and curvature tensor are

exactly represented in IGA. For more details of Naghdi's shell formulation, interested readers may refer to Naghdi (1973).

Because only specific shapes such as cylinder or sphere are generally represented by using curvilinear coordinates in Naghdi's shell, it is difficult to model the arbitrary shape of shell surface. NURBS basis functions are composed by two parameters and Naghdi shell element has two curvilinear coordinates. Therefore, by choosing the NURBS parameter as curvilinear coordinates and placing control points as we want, arbitrary shape of shell surface can be modeled in IGA (Rho and Cho 2004). Also, this approach has advantage on shape optimization due to its flexible shape change. In this paper, NURBS parameter will be used as curvilinear coordinates in all numerical examples for shell.

2.3.2 Equilibrium equations considering surface effects

Based on the kinematics of deformation of Naghdi's shell, the equilibrium equations considering surface effects in nanoscale are presented. Consider the domain of the shell component $\hat{\Omega}^* \subset \mathbf{E}^3$ mapped into the domain $\Omega \times \mathbf{R}, \Omega \subset \mathbf{R}^2$. Upper and lower surface of shell are defined as Ω^+ and Ω^-, respectively as shown in figure 2.5. The bulk strain energy W_{bulk} is given as

$$W_{bulk} = \int_{\Omega^*} \left(\frac{1}{2} \sigma^{\alpha\beta} E_{\alpha\beta} + \sigma^{\alpha 3} E_{\alpha 3} \right) \sqrt{a} d\Omega^*, \tag{2.33}$$

where $\sigma^{\alpha\beta}$ is bulk stress and $E_{\alpha\beta}$ is the bulk strain measure. $\sigma^{\alpha 3}$ and $E_{\alpha 3}$ are for shear deformation, respectively. a is the determinant of the metric tensor.

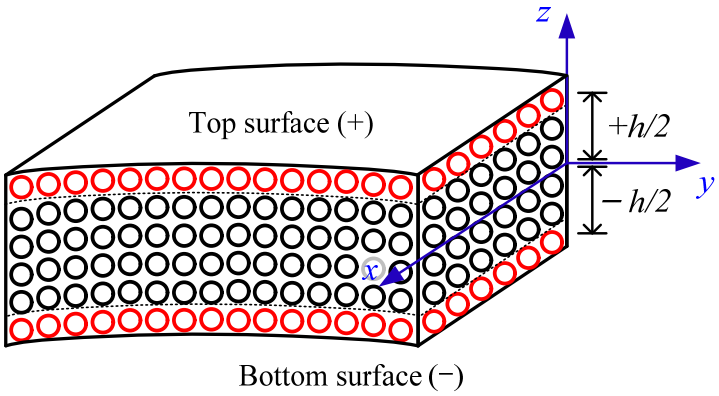

Figure 2.5 The alignments of bond chains of an atom in surface and bulk

Surface energy on the upper and lower surface is given as

$$W_{surf} = \int_{\Omega^+}\left(\frac{1}{2}\tau_{(+)}^{\alpha\beta}E_{\alpha\beta} + \tau_{(+)}^{\alpha 3}E_{\alpha 3}\right)\sqrt{a}d\Omega^+ + \int_{\Omega^-}\left(\frac{1}{2}\tau_{(-)}^{\alpha\beta}E_{\alpha\beta} + \tau_{(-)}^{\alpha 3}E_{\alpha 3}\right)\sqrt{a}d\Omega^-, \tag{2.34}$$

where $\tau_{(+)}^{\alpha\beta}$ and $\tau_{(-)}^{\alpha\beta}$ are surface stresses on the upper and lower surface, respectively. The total potential energy is obtained as

$$\Pi = \int_{\Omega^*}\left(\frac{1}{2}\sigma^{\alpha\beta}E_{\alpha\beta} + \sigma^{\alpha 3}E_{\alpha 3}\right)\sqrt{a}d\Omega^* - \int_{\Omega^*}\left(f^{\alpha}\overline{z}_{\alpha} + f^{n}\overline{w}\right)\sqrt{a}d\Omega^* + \int_{\Omega^+}\left(\frac{1}{2}\tau_{(+)}^{\alpha\beta}E_{\alpha\beta} + \tau_{(+)}^{\alpha 3}E_{\alpha 3}\right)\sqrt{a}d\Omega^+ + \int_{\Omega^-}\left(\frac{1}{2}\tau_{(-)}^{\alpha\beta}E_{\alpha\beta} + \tau_{(-)}^{\alpha 3}E_{\alpha 3}\right)\sqrt{a}d\Omega^-, \tag{2.35}$$

where f^{α} and f^{n} are, respectively, in-plane and out-of-plane external body force intensities per unit volume on the middle surface. $\overline{z}_{\alpha}$ and $\overline{w}$ are, respectively, in-plane and out-of-plane virtual displacements on the middle surface. The constitutive equations of the shell component for the bulk stress are given as

$$\sigma^{\alpha\beta} = C^{\alpha\beta\gamma\mu}E_{\gamma\mu} = C^{\alpha\beta\gamma\mu}\left(\varepsilon_{\gamma\mu} + x_3\omega_{\gamma\mu}\right) \tag{2.36}$$

and

$$\sigma^{\alpha 3} = C^{\alpha 3 \beta 3} E_{\beta 3} = C^{\alpha 3 \beta 3} \gamma_{\beta}, \tag{2.37}$$

where

$$C^{\alpha\beta\gamma\mu} = \lambda a^{\alpha\beta} a^{\gamma\mu} + \mu\left(a^{\alpha\gamma} a^{\beta\mu} + a^{\alpha\mu} a^{\beta\gamma}\right) \tag{2.38}$$

and

$$C^{\alpha 3 \beta 3} = \mu a^{\alpha\beta}, \tag{2.39}$$

where μ and λ are Lame constants. Surface Lame constants are different from the Lame constants of the bulk used in equations (2.38) and (2.39). The constitutive equations on the upper and lower surfaces of the shell component are given as

$$\tau_{(\pm)}^{\alpha\beta} = \tau_0 a^{\alpha\beta} + C_{(s)}^{\alpha\beta\gamma\mu}\left(\varepsilon_{\gamma\mu} \pm \frac{h}{2}\omega_{\gamma\mu}\right) \text{ and } \tau_{(\pm)}^{\alpha 3} = C_{(s)}^{\alpha 3 \beta 3}\gamma_{\beta} \tag{2.40}$$

where

$$C_{(s)}^{\alpha\beta\gamma\mu} = \lambda_0 a^{\alpha\beta} a^{\gamma\mu} + \mu_0\left(a^{\alpha\gamma} a^{\beta\mu} + a^{\alpha\mu} a^{\beta\gamma}\right) \tag{2.41}$$

and

$$C_{(s)}^{\alpha 3 \beta 3} = \mu_0 a^{\alpha\beta}, \tag{2.42}$$

where μ_0 and λ_0 are surface Lame constants and τ_0 is the residual surface stress under unstrained conditions. Chiu and Chen (2001) suggest that higher-order surface stress which considers not only the effect of in-plane membrane surface stresses, but also the surface moments. Surface moments are given as

$$m_{(\pm)}^{\alpha\beta} = d_s \frac{1-\nu^2}{E} C^{\alpha\beta\gamma\mu}\omega_{\gamma\mu} \tag{2.43}$$

where $m_{(+)}^{\alpha\beta}$ and $m_{(-)}^{\alpha\beta}$ are surface moments on the upper and lower surface,

respectively. They are induced from the non-uniform surface stress across the layer thickness. d_s is surface bending stiffness parameter. Applying the above constitutive equations and using the principle of minimum total potential energy, an equilibrium equation is expressed as

$$a_\Omega(\mathbf{z},\overline{\mathbf{z}}) = l_\Omega(\overline{\mathbf{z}}),\ {}^\forall\overline{\mathbf{z}} \in \overline{Z}, \tag{2.44}$$

where the bilinear strain energy and load linear forms are obtained as

$$\begin{aligned} a_\Omega(\mathbf{z},\overline{\mathbf{z}}) \equiv & \int_\Omega \left\{ \left(C^{\alpha\beta\mu\lambda} h + 2C_{(s)}^{\alpha\beta\gamma\mu} \right) \varepsilon_{\alpha\beta}(\mathbf{z}) \varepsilon_{\mu\lambda}(\overline{\mathbf{z}}) \right\} \sqrt{a} d\Omega \\ & + \int_\Omega \left\{ \left(\frac{h^3}{12} C^{\alpha\beta\mu\lambda} + \frac{h^2}{2} C_{(s)}^{\alpha\beta\gamma\mu} + 2d_s \frac{1-\nu^2}{E} C^{\alpha\beta\mu\lambda} \right) \omega_{\alpha\beta}(\mathbf{z}) \omega_{\mu\lambda}(\overline{\mathbf{z}}) \right\} \sqrt{a} d\Omega \\ & + \int_\Omega \left\{ \left(C^{\alpha 3\beta 3} h + 2C_{(s)}^{\alpha 3\beta 3} \right) \gamma_\alpha(\mathbf{z}) \gamma_\beta(\overline{\mathbf{z}}) \right\} \sqrt{a} d\Omega \end{aligned} \tag{2.45}$$

and

$$l_\Omega(\overline{\mathbf{z}}) \equiv \int_\Omega \left(f^\alpha \overline{z}_\alpha + f^n \overline{w} - 2\tau_0 a^{\alpha\beta} \varepsilon_{\alpha\beta}(\overline{\mathbf{z}}) \right) \sqrt{a} d\Omega, \tag{2.46}$$

$\overline{Z} \subset [H^1(\Omega)]^d$ is d-dimensional variational spaces of kinematically admissible displacements. From equation (2.45), the change of effective membrane, bending and shear modulus are observed by considering surface effects.

Using an isoparametric mapping, approximated response and virtual response are expressed, in terms of NURBS basis functions and the response coefficients at control points as equations (2.20) and (2.21). Using equations (2.20) and (2.21), the variational equation (2.44) can be rewritten as

$$a_\Omega(\mathbf{z},\overline{\mathbf{z}}) = l_\Omega(\overline{\mathbf{z}}),\ {}^\forall\overline{\mathbf{z}} = \sum_I^{CP} W_I(\Xi)\overline{\mathbf{y}}_I \in \overline{Z}, \tag{2.47}$$

where

$$a_\Omega(\mathbf{z},\overline{\mathbf{z}}) = \int_\Omega \sum_{I,K}^{CP} \overline{\mathbf{y}}_I^T \left\{ \mathbf{B}_I^{\mathrm{m}T} \left(\mathbf{C}h + 2\mathbf{C}_{\mathrm{surf}} \right) \mathbf{B}_K^{\mathrm{m}} \right\} \mathbf{y}_K \sqrt{a} d\Omega$$

$$+\int_{\Omega}\sum_{I,K}^{CP}\overline{\mathbf{y}}_I^T\left\{\mathbf{B}_I^{\mathrm{b}T}\left(\frac{h^3}{12}\mathbf{C}+\frac{h^2}{2}\mathbf{C}_{\mathrm{surf}}+2d_s\frac{1-\nu^2}{E}\mathbf{C}\right)\mathbf{B}_K^{\mathrm{b}T}\right\}\mathbf{y}_K\sqrt{a}d\Omega$$

$$+\int_{\Omega}\sum_{I,K}^{CP}\overline{\mathbf{y}}_I^T\left\{\mathbf{B}_I^{\mathrm{s}T}\left(\mathbf{C}^{\mathrm{s}}h+2\mathbf{C}_{\mathrm{surf}}^{\mathrm{s}}\right)\mathbf{B}_K^{\mathrm{s}T}\right\}\mathbf{y}_K\sqrt{a}d\Omega \tag{2.48}$$

and

$$l_{\Omega}\left(\overline{\mathbf{z}}\right)=\int_{\Omega}\sum_{I}^{CP}\left(\mathbf{f}^T W_I\overline{\mathbf{y}}_I-\mathbf{f}_{\tau_0}^T\mathbf{B}_I^{\mathrm{m}}\overline{\mathbf{y}}_I\right)\sqrt{a}d\Omega, \tag{2.49}$$

where $\mathbf{B}^{\mathrm{m}}$, $\mathbf{B}^{\mathrm{b}}$ and $\mathbf{B}^{\mathrm{s}}$ are membrane, bending and shear strain-displacement matrix. $\mathbf{C}$ and $\mathbf{C}^{\mathrm{s}}$ are constitutive matrices for the plane stress homogeneous linear elastic isotropic materials. $\mathbf{C}_{\mathrm{surf}}$ and $\mathbf{C}^{\mathrm{s}}{}_{\mathrm{surf}}$ are those of the surface. $\mathbf{f}$ is force component matrix and $\mathbf{f}_{\tau_0}$ is force component matrix by residual surface stress. The membrane $\mathbf{B}^{\mathrm{m}}$, bending $\mathbf{B}^{\mathrm{b}}$ and shear strain-displacement matrix $\mathbf{B}^{\mathrm{s}}$ are given as

$$\mathbf{B}_I^m=\begin{bmatrix} W_{I,\xi}-\Gamma_{11}^1W_I & -\Gamma_{11}^2W_I & -b_{11}W_I & 0 & 0\\ -\Gamma_{22}^1W & W_{I,\eta}-\Gamma_{22}^2W_I & -b_{22}W_I & 0 & 0\\ 2W_{I,\eta}-2\Gamma_{12}^1W_I & 2W_{I,\xi}-2\Gamma_{12}^1W_I & -2b_{12}W_I & 0 & 0\end{bmatrix}, \tag{2.50}$$

$$\mathbf{B}_I^b=\begin{bmatrix} 0 & 0 & 0 & W_{I,\xi}-\Gamma_{11}^1W_I & -\Gamma_{11}^2W_I\\ 0 & 0 & 0 & -\Gamma_{22}^1W_I & W_{I,\eta}-\Gamma_{22}^2W_I\\ 0 & 0 & 0 & 2W_{I,\eta}-2\Gamma_{12}^1W_I & 2W_{I,\xi}-2\Gamma_{12}^2W_I\end{bmatrix}, \tag{2.51}$$

and

$$\mathbf{B}_I^s=\begin{bmatrix} b_1^1W_I & b_1^2W_I & W_{I,\xi} & W_I & 0\\ b_2^1W_I & b_2^2W_I & W_{I,\eta} & 0 & W_I\end{bmatrix}. \tag{2.52}$$

Also, the constitutive matrices for the plane stress homogeneous linear elastic isotropic materials are given in matrix form as

$$\mathbf{C}=\frac{E}{2\left(1+\nu\right)}\begin{bmatrix} 2a^{11}a^{11}+\dfrac{2\nu}{1-\nu}a^{11}a^{11} & 2a^{12}a^{12}+\dfrac{2\nu}{1-\nu}a^{11}a^{22} & 2a^{11}a^{12}+\dfrac{2\nu}{1-\nu}a^{11}a^{12} \\ & 2a^{22}a^{22}+\dfrac{2\nu}{1-\nu}a^{22}a^{22} & 2a^{22}a^{12}+\dfrac{2\nu}{1-\nu}a^{22}a^{12} \\ \textit{sym.} & & a^{11}a^{22}+a^{12}a^{12}+\dfrac{2\nu}{1-\nu}a^{12}a^{12} \end{bmatrix}, \tag{2.53}$$

$$\mathbf{C}_{\text{surf}}=\begin{bmatrix} 2\mu_0 a^{11}a^{11}+\lambda_0 a^{11}a^{11} & 2\mu_0 a^{12}a^{12}+\lambda_0 a^{11}a^{22} & 2\mu_0 a^{11}a^{12}+\lambda_0 a^{11}a^{12} \\ & 2\mu_0 a^{22}a^{22}+\lambda_0 a^{22}a^{22} & 2\mu_0 a^{22}a^{12}+\lambda_0 a^{22}a^{12} \\ \textit{sym.} & & \mu_0\left(a^{11}a^{22}+a^{12}a^{12}\right)+\lambda_0 a^{12}a^{12} \end{bmatrix}, \tag{2.54}$$

$$\mathbf{C}^{\text{s}}=\frac{E}{2\left(1+\nu\right)}\begin{bmatrix} a^{11} & a^{12} \\ a^{12} & a^{22} \end{bmatrix}, \tag{2.55}$$

and

$$\mathbf{C}^{\text{s}}_{\text{surf}}=\mu_0\begin{bmatrix} a^{11} & a^{12} \\ a^{12} & a^{22} \end{bmatrix}. \tag{2.56}$$

Force component matrix by residual surface stress is given as

$$\mathbf{f}_{\tau_0}=\begin{bmatrix} 2\tau_0 a^{11} \\ 2\tau_0 a^{22} \\ 2\tau_0 a^{12} \end{bmatrix}. \tag{2.57}$$

The integration of the bilinear energy form and load linear form in equation (2.47) can be evaluated using numerical integration methods as Gaussian quadrature. The four-point Gaussian quadrature formula is used for numerical integration.

2.3.3 Equilibrium equations considering nonlocal effects

The theory of nonlocal elasticity states that the stress at a given reference point depends not only on the stress at this point, but also on the stress at other points in the body. This way, the influence of the long range forces between the atoms is taken into consideration, and thus the internal length scale is considered in the constitutive equations. The nonlocal stress tensor at point **x** is expressed as

$$\sigma_{\alpha\beta}(\mathbf{x}) = \int \alpha\left(\left|\mathbf{x}' - \mathbf{x}\right|, \tau\right)\bar{\sigma}_{\alpha\beta}(\mathbf{x}')d\mathbf{x}' \tag{2.58}$$

where $\bar{\sigma}_{\alpha\beta}$ are the components of the classical local stress tensor, which are related to the componenets of the linear strain tensor $\varepsilon_{\gamma\mu}$ by the conventional constitutive relations as

$$\bar{\sigma}_{\alpha\beta} = C^{\alpha\beta\gamma\mu}\varepsilon_{\gamma\mu} \tag{2.59}$$

The kernel function $\alpha(|\boldsymbol{x}`\text{-}\boldsymbol{x}|,\tau)$ represents the nonlocal modulus. $|\mathbf{x}`\text{-}\mathbf{x}|$ being the Euclidean distance and $\tau = e_0 a / l$ is a scale factor, where e_0 is an adjusting constant which needs to be determined from experiments or MD simulation results. a is a characteristic internal length such as C-C bond of lattice parameter and l is the external characteristic length such as crack length or wave length. It is possible to represent the integral constitutive relations given by equation (2.57) in an equivalent differential form as (Eringen 1983)

$$\left(1 - \mu\nabla^2\right)\sigma_{\alpha\beta} = \bar{\sigma}_{\alpha\beta}. \tag{2.60}$$

where nonlocal parameter $\mu=e_0^2a^2$ is introduced. Based on the kinematics of deformation of Naghdi's shell, the equilibrium equations considering

nonlocal effects in nanoscale are presented. In Eringen's theory, equilibrium is expressed in terms of nonlocal resultants $N^{\alpha\beta}$,$M^{\alpha\beta}$and V^{α} as

$$N^{\alpha\beta}\Big\|_{\beta} - b_{\alpha}^{\lambda}V^{\alpha} + f^{\alpha} = 0, \tag{2.61}$$

$$M^{\alpha\beta}\Big\|_{\beta} - V^{\alpha} = 0, \tag{2.62}$$

and

$$b_{\alpha\beta}N^{\alpha\beta} + V^{\alpha}\Big\|_{\alpha} + f^{n} = 0. \tag{2.63}$$

The relations between local stress and nonlocal stress are given as

$$N^{\alpha\beta} - \mu\nabla^2 N^{\alpha\beta} = \bar{N}^{\alpha\beta} = hC^{\alpha\beta\gamma\mu}\varepsilon_{\gamma\mu}(\mathbf{z}), \tag{2.64}$$

$$M^{\alpha\beta} - \mu\nabla^2 M^{\alpha\beta} = \bar{M}^{\alpha\beta} = \frac{h^3}{12}C^{\alpha\beta\gamma\mu}\omega_{\gamma\mu}(\mathbf{z}) \tag{2.65}$$

and

$$V^{\alpha} - \mu\nabla^2 V^{\alpha} = \bar{V}^{\alpha} = hC^{\alpha 3\beta 3}\gamma_{\beta}(\mathbf{z}) \tag{2.66}$$

where resultants with bar $\bar{N}^{\alpha\beta}$, $\bar{M}^{\alpha\beta}$ and $\bar{V}^{\alpha}$ mean local resultants. Equations (2.61)-(2.63) and equations (2.64)-(2.66) are coupled and must thus be solved simultaneously. Governing equations (2.61)-(2.63) are given in its weak form as

$$\begin{aligned}&\int_{\Omega}\left[\left(N^{\lambda\beta}\Big\|_{\beta} - b_{\alpha}^{\lambda}V^{\alpha} + f^{\alpha}\right)\bar{u}_{\lambda} + \left(M^{\alpha\beta}\Big\|_{\beta} - V^{\alpha}\right)\bar{\psi}_{\alpha}\right]\sqrt{a}d\Omega \\ &+\int_{\Omega}\left[\left(b_{\alpha\beta}N^{\alpha\beta} + V^{\alpha}\Big\|_{\alpha} + f^{n}\right)\bar{w}\right]\sqrt{a}d\Omega = 0\end{aligned} \tag{2.67}$$

Embedding the equations (2.64)-(2.66) into equation (2.67) yields

$$\begin{aligned}&\int_{\Omega}\left[\bar{N}^{\alpha\beta}\Big\|_{\beta}\bar{u}_{\alpha} + b_{\alpha\beta}\bar{N}^{\alpha\beta}\bar{w} + \bar{M}^{\alpha\beta}\Big\|_{\beta}\bar{\psi}_{\alpha} + \bar{V}^{\alpha}\Big\|_{\alpha}\bar{w}\right]\sqrt{a}d\Omega \\ &+\int_{\Omega}\left[-\bar{V}^{\alpha}\bar{\psi}_{\alpha} - b_{\alpha}^{\lambda}\bar{V}^{\alpha}\bar{u}_{\lambda} + f^{\alpha}\bar{u}_{\lambda} + f^{n}\bar{w}\right]\sqrt{a}d\Omega\end{aligned}$$

$$+\mu\int_{\Omega}\left[\nabla^2 N^{\alpha\beta}\big\|_{\beta}\,\overline{u}_{\alpha}+b_{\alpha\beta}\nabla^2 N^{\alpha\beta}\overline{w}+\nabla^2 M^{\alpha\beta}\big\|_{\beta}\,\overline{\psi}_{\alpha}\right]\sqrt{a}d\Omega$$

$$+\mu\int_{\Omega}\left[\nabla^2 V^{\alpha}\big\|_{\alpha}\,\overline{w}-\nabla^2 V^{\alpha}\overline{\psi}_{\alpha}-b_{\alpha}^{\lambda}\nabla^2 V^{\alpha}\overline{u}_{\lambda}\right]\sqrt{a}d\Omega=0. \tag{2.68}$$

Also, the following relations are valid for the terms dependent on μ term.

$$\int_{\Omega}\left[\left(\nabla^2 N^{\alpha\beta}\big\|_{\beta}-b_{\alpha}^{\lambda}\nabla^2 V^{\alpha}\right)\overline{u}_{\alpha}\right]\sqrt{a}d\Omega$$

$$=\int_{\Omega}\left[f^{\alpha}\big\|_{\beta}\,\overline{u}_{\alpha}\big\|_{\beta}-b_{\beta}^{\alpha}\,f^{n}\big\|_{\beta}\,\overline{u}_{\alpha}\right]\sqrt{a}d\Omega, \tag{2.69}$$

$$\int_{\Omega}\left[\left(\nabla^2 M^{\alpha\beta}\big\|_{\beta}-\nabla^2 V^{\alpha}\right)\overline{\psi}_{\alpha}\right]\sqrt{a}d\Omega=\int_{\Omega}\left[f^{n}\big\|_{\alpha}\,\overline{\psi}_{\alpha}+f^{n}\,\overline{\psi}_{\alpha}\big\|_{\alpha}\right]\sqrt{a}d\Omega \tag{2.70}$$

and

$$\int_{\Omega}\left[\left(b_{\alpha\beta}\nabla^2 N^{\alpha\beta}+\nabla^2 V^{\alpha}\big\|_{\alpha}\right)\overline{w}\right]\sqrt{a}d\Omega=\int_{\Omega}\left[b_{\alpha\beta}\,f^{\alpha}\big\|_{\beta}\,\overline{w}-f^{n}\big\|_{\delta}\,\overline{w}\big\|_{\delta}\right]\sqrt{a}. \tag{2.71}$$

Embedding the equations (2.69)-(2.71) into equations (2.68) and applying divergence theorem yields final governing equations as

$$a_{\Omega}(\mathbf{z},\overline{\mathbf{z}})\equiv\int_{\Omega}\left[C^{\alpha\beta\mu\lambda}\varepsilon_{\alpha\beta}(\mathbf{z})\varepsilon_{\mu\lambda}(\overline{\mathbf{z}})h+\frac{h^3}{12}C^{\alpha\beta\mu\lambda}\omega_{\alpha\beta}(\mathbf{z})\omega_{\mu\lambda}(\overline{\mathbf{z}})\right]\sqrt{a}d\Omega$$

$$+\int_{\Omega}\left[C^{\alpha 3\beta 3}\gamma_{\alpha}(\mathbf{z})\gamma_{\beta}(\overline{\mathbf{z}})h\right]\sqrt{a}d\Omega$$

$$=\int_{\Omega}\left[\mu\left\{f_{,\beta}^{\alpha}\varepsilon_{\alpha\beta}(\overline{\mathbf{z}})+f^{n}\omega_{\alpha\alpha}(\overline{\mathbf{z}})+f_{,\alpha}^{n}\gamma_{\alpha}(\overline{\mathbf{z}})\right\}\right]\sqrt{a}d\Omega$$

$$+\int_{\Omega}\left[f^{\alpha}\overline{z}_{\alpha}+f^{n}\overline{w}\right]\sqrt{a}d\Omega\equiv l_{\Omega}^{\mu}(\overline{\mathbf{z}}),\ {}^{\forall}\overline{\mathbf{z}}\in\overline{Z} \tag{2.72}$$

$\overline{Z}\subset[H^1(\Omega)]^d$ is d-dimensional variational spaces of kinematically admissible displacements. Using equations (2.20) and (2.21), the variational equation (2.72) can be rewritten as

$$a_{\Omega}(\mathbf{z},\overline{\mathbf{z}})=l_{\Omega}(\overline{\mathbf{z}}),\ {}^{\forall}\overline{\mathbf{z}}=\sum_{I}^{CP}W_I(\Xi)\overline{\mathbf{y}}_I\in\overline{Z}, \tag{2.73}$$

where

$$a_{\Omega}\left(\mathbf{z},\overline{\mathbf{z}}\right)=\int_{\Omega}\sum_{I,K}^{CP}\overline{\mathbf{y}}_I^T\left\{\mathbf{B}_I^{\mathrm{m}T}\mathbf{C}\mathbf{B}_K^{\mathrm{m}}h+\frac{h^3}{12}\mathbf{B}_I^{\mathrm{b}T}\mathbf{C}\mathbf{B}_K^{\mathrm{b}T}+\mathbf{B}_I^{\mathrm{s}T}\mathbf{C}^{\mathrm{s}}\mathbf{B}_K^{\mathrm{s}T}h\right\}\mathbf{y}_K\sqrt{a}d\Omega \qquad (2.74)$$

and

$$l_{\Omega}\left(\overline{\mathbf{z}}\right)=\int_{\Omega}\sum_{I}^{CP}\left(\mathbf{f}^T W_I\overline{\mathbf{y}}_I+\mu\left(\mathbf{B}_I^{mT}\mathbf{f}^{\tan(')}+\mathbf{B}_I^{bT}\mathbf{f}^{\mathrm{nor}}+\mathbf{B}_I^{sT}\mathbf{f}^{\mathrm{nor}(')}\right)\right)\sqrt{a}d\Omega, \qquad (2.75)$$

where $\mathbf{B}^{\mathrm{m}}$, $\mathbf{B}^{\mathrm{b}}$ and $\mathbf{B}^{\mathrm{s}}$ are membrane, bending and shear strain-displacement matrix. $\mathbf{C}$ and $\mathbf{C}^{\mathrm{s}}$ are constitutive matrices for the plane stress homogeneous linear elastic isotropic materials. $\mathbf{f}$ is force component matrix. Superscripts on $\mathbf{f}$ tan(`), nor and nor(`) mean that it considers only its tangential or normal component with or without derivatives. The membrane $\mathbf{B}^{\mathrm{m}}$, bending $\mathbf{B}^{\mathrm{b}}$ and shear strain-displacement matrix $\mathbf{B}^{\mathrm{s}}$ are given as equations (2.50)-(2.52). Also, the constitutive matrices for the plane stress homogeneous linear elastic isotropic materials are given in matrix form as equations (2.53) and (2.55).

Displacement solution fields considering nonlocal effects are obtained through equation (2.73), but nonlocal stress field cannot be obtained directly from equation (2.73). Therefore, staggered approach is introduced to obtain nonlocal stress field. (Askes et al. 2008) The staggered approach consists of solving the equation (2.73), computing the local strains and using the quantity as a source term for solving Helmholtz equations (2.64)-(2.66). Many attempts have been made in classical elasticity to implement finite elements with separate interpolations for stresses and displacements. However, simple and straightforward implementation of the Eringen theory that provides optimal convergence has not been accomplished as yet, and may not be feasible. (Askes and Aifantis 2011)

The differences between surface elasticity and nonlocal elasticity are as follows. Surface effects are caused by the differences of the coordination of

atoms between bulk and surface as shown in figure 2.5-(a). The influences of surface have to be taken into account as the surface to volume ratio increases in nanoscale systems. Nonlocal effects are related to the non-continuum nature of material interactions on a molecular scale and not negligible in nanoscale structures as shown in figure 2.5-(b). In surface elasticity theory, the changes of mechanical behavior are observed as the cross sectional area in 1D structure or thickness in 2D structure varies. However, nonlocal theory only represents the change of mechanical behavior as the length in 1D structure or area of the surface in 2D structure varies. The exactness of nonlocal theory comes from it considers long range force between atoms and it can be more strict consideration than the way surface elasticity considers length scale parameter by residual surface stress. Therefore, surface elasticity is more suitable choice for observing the dependence on the variations of cross sectional area in 1D structure or variation of thickness in 2D structure. On the other hand, nonlocal elasticity is appropriate for observing small scale effects of carbon nanotubes or graphene which is 1 layered structure. And besides, stress singularity is not observed in crack tip problems by considering nonlocal effects. Therefore, nonlocal elasticity is proper for crack propagation problems in nanoscale.

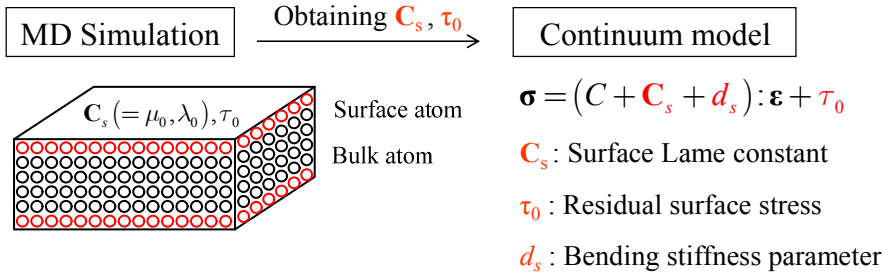

(a) Surface elasticity

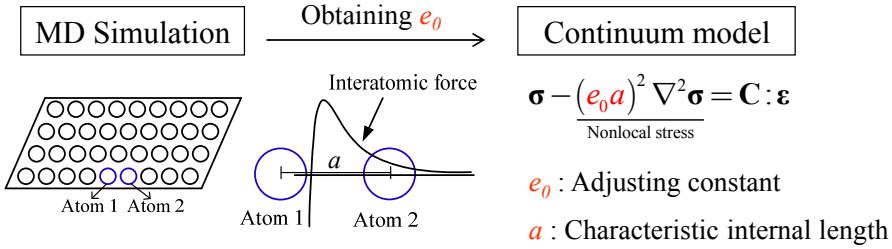

(b) Nonlocal elasticity

Figure 2.6 The difference between surface and nonlocal elasticity

Chapter 3. Isogeometric Design Sensitivity Analysis considering Size Effects

3.1 Beam structures

3.1.1 Sizing design sensitivity analysis considering surface effects

By using the chain rule of differentiation, the variational equation considering surface effects can be differentiated with respect to τ as

$$\frac{d}{d\tau}\left[a_{\mathbf{u}+\tau\delta\mathbf{u}}\left(\mathbf{z}\left(x;\mathbf{u}+\tau\delta\mathbf{u}\right),\overline{\mathbf{z}}\right)\right]\Big|_{\tau=0} = a'_{\delta\mathbf{u}}\left(\mathbf{z},\overline{\mathbf{z}}\right)+a_{\mathbf{u}}\left(\mathbf{z}',\overline{\mathbf{z}}\right) \tag{3.1}$$

and

$$\frac{d}{d\tau}\left[l_{\mathbf{u}+\tau\delta\mathbf{u}}\left(\overline{\mathbf{z}}\right)\right]\Big|_{\tau=0} = l'_{\delta\mathbf{u}}\left(\overline{\mathbf{z}}\right). \tag{3.2}$$

where **u** denotes a design vector function and the first term on the right side of equation (3.1) represents the explicit dependence of a_u on the design, whereas the second term of equation (3.1) represents the implicit dependence through the variation of the state variable. From equations (3.1) and (3.2), we can obtain

$$a_{\mathbf{u}}\left(\mathbf{z}',\overline{\mathbf{z}}\right) = l'_{\delta\mathbf{u}}\left(\overline{\mathbf{z}}\right) - a'_{\delta\mathbf{u}}\left(\mathbf{z},\overline{\mathbf{z}}\right) \tag{3.3}$$

If we let the design vector ***u*** is a diameter of circular cross section D, the design variations of bilinear form is obtained as

$$a'_{\delta D}\left(\mathbf{z},\overline{\mathbf{z}}\right) = \int_0^L \left[\left\{\left(\frac{\pi E D^3}{16}+\frac{3\pi D^2}{8}+2d_s\right)(2\mu_0+\lambda_0)\right\}\frac{\partial^2 w}{\partial x^2}\frac{\partial^2 \overline{w}}{\partial x^2}+2\tau_0\frac{\partial w}{\partial x}\frac{\partial \overline{w}}{\partial x}\right]dx \tag{3.4}$$

The design variation of load linear form vanishes.

3.1.2 Material derivatives

Consider the variation of the 1D domain from an original domain Ω to a perturbed one Ω_τ as shown in Figure 3.1. Suppose that only one parameter τ defines a transformation, and the mapping T is given by

$$\mathbf{x}_\tau \equiv T(\tau, x) \tag{3.5}$$

and

$$\Omega_\tau \equiv T(\tau, \Omega). \tag{3.6}$$

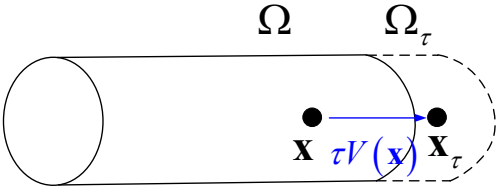

Figure 3.1 Design variation of 1D domain using linear mapping

A design velocity field that is equivalent to a mapping rate can be defined as

$$\mathbf{V}(\tau, \mathbf{x}) = \frac{d\mathbf{x}_\tau}{d\tau} = \frac{dT(\tau, x)}{d\tau}. \tag{3.7}$$

In a neighborhood of τ=0, under certain regularity hypothesis and ignoring higher-order terms, the following linear mapping relation is obtained

$$\mathbf{x}_\tau \approx T(0, x) + \tau \frac{\partial T}{\partial \tau}(0, x) = \mathbf{x}(x) + \tau \mathbf{V}(x), \tag{3.8}$$

in which the linear design velocity field at the middle surface of the shell is defined as

$$\mathbf{V}(x) \equiv \mathbf{V}(0, x) = \left. \frac{dx_\tau}{d\tau} \right|_{\tau=0}. \tag{3.9}$$

A performance measure for the beam component may be written in domain

integral form as

$$\Phi = \int_{\Omega} f(x) d\Omega. \tag{3.10}$$

The material derivative of Φ at Ω is obtained as

$$\Phi' = \int_{\Omega} \left\{ f'(x) + div\left(f(x)\mathbf{V}(x) \right) \right\} d\Omega. \tag{3.11}$$

3.1.3 Shape design sensitivity analysis considering surface effects

By using the material derivative formula given in equation (3.11), the variational equation considering surface effects given in equation (2.17) can be differentiated with respect to τ as

$$\frac{d}{d\tau}\left[a_{\Omega_\tau}(\mathbf{z}_\tau, \overline{\mathbf{z}}_\tau) \right]\Big|_{\tau=0}$$

$$= \int_{\Omega} \left(EI^* w'_{,11}\, \overline{w}_{,11} + EI^* w_{,11} \overline{w}'_{,11} - 2\tau_0 D w'_{,1}\, \overline{w}_{,1} - 2\tau_0 D w_{,1} \overline{w}'_{,1} \right) d\Omega$$

$$+ \int_{\Omega} \left(EI^* w_{,11} \overline{w}_{,11} - 2\tau_0 D w_{,1} \overline{w}_{,1} \right)_{,1} V + \left(EI^* w_{,11} \overline{w}_{,11} - 2\tau_0 D w_{,1} \overline{w}_{,1} \right) V_{,1} d\Omega \tag{3.12}$$

and

$$\frac{d}{d\tau}\left[l_{\Omega_\tau}(\overline{\mathbf{z}}_\tau) \right]\Big|_{\tau=0} = \int_{\Omega} \left(q\overline{w}' + q\overline{w}_{,1} V + q\overline{w} V_{,1} \right) d\Omega, \tag{3.13}$$

From the material derivative of response solution, we obtain

$$\dot{w} = w' + w_{,1} V. \tag{3.14}$$

Its spatial derivatives are expressed as

$$w'_{,1} = \dot{w}_{,1} - w_{,1} V_{,1} - w_{,11} V \tag{3.15}$$

and

$$w'_{,11} = \dot{w}_{,11} - w_{,11} V_{,1} - w_{,1} V_{,11} - w_{,111} V - w_{,11} V_{,1}. \tag{3.16}$$

Substituting equations (3.15) and (3.16) into equation (3.12) yields

$$\frac{d}{d\tau}\left[a_{\Omega_\tau}\left(\mathbf{z}_\tau,\overline{\mathbf{z}}_\tau\right)\right]\Big|_{\tau=0} =$$

$$\int_\Omega\left\{EI^*\left(\dot{w}_{,11}-w_{,11}V_{,1}-w_{,1}V_{,11}-w_{,111}V-w_{,11}V_{,1}\right)\overline{w}_{,11}\right\}d\Omega$$

$$+\int_\Omega\left\{EI^*w_{,11}\left(\dot{\overline{w}}_{,11}-\overline{w}_{,11}V_{,1}-\overline{w}_{,1}V_{,11}-\overline{w}_{,111}V-\overline{w}_{,11}V_{,1}\right)\right\}d\Omega$$

$$-\int_\Omega\left(2\tau_0D\left(\dot{w}_{,1}-w_{,1}V_{,1}-w_{,11}V\right)\overline{w}_{,1}\right)d\Omega$$

$$-\int_\Omega\left(2\tau_0Dw_{,1}\left(\dot{\overline{w}}_{,1}-\overline{w}_{,1}V_{,1}-\overline{w}_{,11}V\right)\right)d\Omega$$

$$+\int_\Omega\left(EI^*w_{,11}\overline{w}_{,11}-2\tau_0Dw_{,1}\overline{w}_{,1}\right)_{,1}V+\left(EI^*w_{,11}\overline{w}_{,11}-2\tau_0Dw_{,1}\overline{w}_{,1}\right)V_{,1}d\Omega \tag{3.17}$$

and rearranging equation (3.17) yields

$$\frac{d}{d\tau}\left[a_{\Omega_\tau}\left(\mathbf{z}_\tau,\overline{\mathbf{z}}_\tau\right)\right]\Big|_{\tau=0} =$$

$$\int_\Omega\left\{EI^*\left(\dot{w}_{,11}-w_{,11}V_{,1}-w_{,1}V_{,11}-w_{,11}V_{,1}\right)\overline{w}_{,11}\right\}d\Omega$$

$$+\int_\Omega\left\{EI^*w_{,11}\left(\dot{\overline{w}}_{,11}-\overline{w}_{,11}V_{,1}-\overline{w}_{,1}V_{,11}-\overline{w}_{,11}V_{,1}\right)\right\}d\Omega$$

$$-\int_\Omega\left(2\tau_0D\left(\dot{w}_{,1}-w_{,1}V_{,1}\right)\overline{w}_{,1}+2\tau_0Dw_{,1}\left(\dot{\overline{w}}_{,1}-\overline{w}_{,1}V_{,1}\right)\right)d\Omega$$

$$+\int_\Omega\left\{\left(EI^*w_{,11}\overline{w}_{,11}-2\tau_0Dw_{,1}\overline{w}_{,1}\right)V_{,1}\right\}d\Omega \tag{3.18}$$

Then, the material derivative of the strain energy bilinear form is denoted by

$$\left[a\left(\mathbf{z},\overline{\mathbf{z}}\right)\right]' = a\left(\dot{\mathbf{z}},\overline{\mathbf{z}}\right)+a\left(\mathbf{z},\dot{\overline{\mathbf{z}}}\right)+a'_V\left(\mathbf{z},\overline{\mathbf{z}}\right) \tag{3.19}$$

where

$$a\left(\dot{\mathbf{z}},\overline{\mathbf{z}}\right)=\int_\Omega\left\{EI^*\dot{w}_{,11}\overline{w}_{,11}-2\tau_0D\dot{w}_{,1}\overline{w}_{,1}\right\}d\Omega, \tag{3.20}$$

$$a\left(\mathbf{z},\dot{\overline{\mathbf{z}}}\right)=\int_\Omega\left\{EI^*w_{,11}\dot{\overline{w}}_{,11}-2\tau_0Dw_{,1}\dot{\overline{w}}_{,1}\right\}d\Omega, \tag{3.21}$$

and

$$a'_V(\mathbf{z},\bar{\mathbf{z}}) = \int_\Omega \left\{ EI^* \left(-2w_{,11}V_{,1} - w_{,1}V_{,11}\right)\bar{w}_{,11} \right\} d\Omega$$

$$+ \int_\Omega \left\{ EI^* w_{,11} \left(-2\bar{w}_{,11}V_{,1} - \bar{w}_{,1}V_{,11}\right) \right\} d\Omega$$

$$+ \int_\Omega \left(4\tau_0 D w_{,1}\bar{w}_{,1}V_{,1}\right) d\Omega$$

$$+ \int_\Omega \left\{ \left(EI^* w_{,11}\bar{w}_{,11} - 2\tau_0 D w_{,1}\bar{w}_{,1}\right) V_{,1} \right\} d\Omega \tag{3.22}$$

Substituting equation (3.14) into (3.13) yields

$$\frac{d}{d\tau}\left[l_{\Omega_\tau}(\bar{\mathbf{z}}_\tau) \right]\Big|_{\tau=0} = \int_\Omega \left(q\dot{\bar{w}}_1 + q\bar{w}V_{,1} \right) d\Omega, \tag{3.23}$$

Then, the material derivative of the load linear form is obtained as

$$\frac{d}{d\tau}\left[l_{\Omega_\tau}(\bar{\mathbf{z}}_\tau) \right]\Big|_{\tau=0} = l\left(\dot{\bar{\mathbf{z}}}\right) + l'_V(\bar{\mathbf{z}}) \tag{3.24}$$

where

$$l\left(\dot{\bar{\mathbf{z}}}\right) = \int_\Omega \left(q\dot{\bar{w}}_1 \right) d\Omega \tag{3.25}$$

and

$$l'_V(\bar{\mathbf{z}}) = \int_\Omega \left(q\bar{w}V_{,1} \right) d\Omega \tag{3.26}$$

The material derivative of variational equation for structural elasticity problem is given as

$$\frac{d}{d\tau}\left[a_\Omega(\mathbf{z}_\tau, \bar{\mathbf{z}}_\tau) \right]\Big|_{\tau=0} \equiv a(\dot{\mathbf{z}}, \bar{\mathbf{z}}) + a\left(\mathbf{z}, \dot{\bar{\mathbf{z}}}\right) + a'_V(\mathbf{z}, \bar{\mathbf{z}})$$

$$= l\left(\dot{\bar{\mathbf{z}}}\right) + l'_V(\bar{\mathbf{z}}) \equiv \frac{d}{d\tau}\left[l_\Omega(\bar{\mathbf{z}}_\tau) \right]\Big|_{\tau=0}. \tag{3.27}$$

Since all $\dot{\bar{\mathbf{z}}} \in \bar{Z}$, and following equation is valid.

$$a\left(\mathbf{z}, \dot{\bar{\mathbf{z}}}\right) = l\left(\dot{\bar{\mathbf{z}}}\right). \tag{3.28}$$

The design sensitivity formulation using a direct differentiation method is finally derived as

$$a(\dot{\mathbf{z}},\overline{\mathbf{z}}) = l'_V(\overline{\mathbf{z}}) - a'_V(\mathbf{z},\overline{\mathbf{z}}) \tag{3.29}$$

3.2 Shell structures

3.2.1 Material derivatives in curvilinear coordinates

Since the design domain is the middle surface of a shell, the variation for the thickness direction of the shell is not considered in this paper. Consider the variation of the middle surface of a shell from an original domain $\hat{\Omega} \subset \mathbf{E}^3$ to a perturbed one $\hat{\Omega}_\tau \subset \mathbf{E}^3$. Suppose that only one parameter τ defines a transformation, and the mapping T is given by

$$\hat{\mathbf{x}}_\tau \equiv T(\tau, \hat{\mathbf{x}}) \tag{3.30}$$

and

$$\hat{\Omega}_\tau \equiv T(\tau, \hat{\Omega}). \tag{3.31}$$

A design velocity field that is equivalent to a mapping rate can be defined as

$$\mathbf{V}(\tau, \hat{\mathbf{x}}) = \frac{d\hat{\mathbf{x}}_\tau}{d\tau} = \frac{dT(\tau, \hat{\mathbf{x}})}{d\tau}. \tag{3.32}$$

In a neighborhood of τ=0, under certain regularity hypothesis and ignoring higher-order terms, the following linear mapping relation is obtained as

$$\hat{\mathbf{x}}_\tau \approx T(0, \hat{\mathbf{x}}) + \tau \frac{\partial T}{\partial \tau}(0, \hat{\mathbf{x}}) = \hat{\mathbf{x}}(x_1, x_2) + \tau \mathbf{V}(\hat{\mathbf{x}}), \tag{3.33}$$

in which the linear design velocity field at the middle surface of the shell is defined as

$$\mathbf{V}(\hat{\mathbf{x}}) \equiv \mathbf{V}(0, \hat{\mathbf{x}}) = \left. \frac{d\hat{\mathbf{x}}_\tau}{d\tau} \right|_{\tau=0}. \tag{3.34}$$

The material point $\mathbf{x}_\tau \in \mathbf{R}^2$ is mapped into $\hat{\mathbf{x}}_\tau \in \mathbf{E}^3$, and perturbed basis $\mathbf{a}_{1\tau}$, $\mathbf{a}_{2\tau}$ and $\mathbf{a}^3{}_\tau$ are defined for the perturbed material point $\hat{\mathbf{x}}_\tau$ as shown in

figure 3.2.

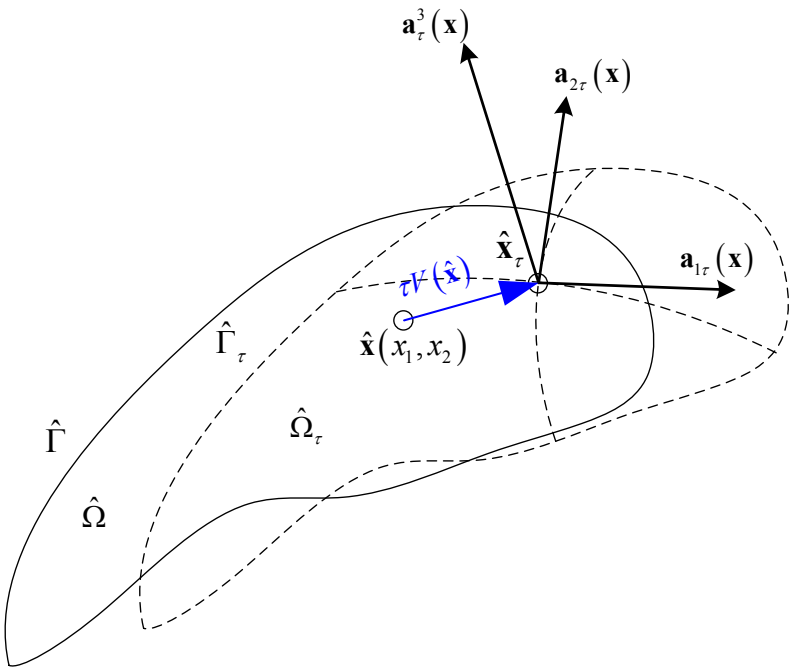

Figure 3.2 Design variation of the middle surface of the shell

A performance measure for the shell component may be written in domain integral form as

$$\Phi = \int_{\Omega} f(\mathbf{x}) \sqrt{a(\mathbf{x})} d\Omega. \tag{3.35}$$

The material derivative of Φ at Ω is obtained as

$$\Phi' = \int_{\Omega} \left\{ \dot{f}(\mathbf{x}) \sqrt{a(\mathbf{x})} + f(\mathbf{x}) \left(\sqrt{a(\mathbf{x})} \right)' \right\} d\Omega. \tag{3.36}$$

3.2.2 Shape design sensitivity analysis considering surface effects

By using the material derivative formula given in equation (3.36), the

variational equation considering surface effects can be differentiated with respect to τ as

$$\frac{d}{d\tau}\left[a_{\Omega_\tau}\left(\mathbf{z}_\tau,\overline{\mathbf{z}}_\tau\right)\right]\Big|_{\tau=0}=\int_\Omega \dot{F}\left(\mathbf{z},\overline{\mathbf{z}}\right)\sqrt{a}\,d\Omega+\int_\Omega F\left(\mathbf{z},\overline{\mathbf{z}}\right)\left(\sqrt{a}\right)^{\cdot}\,d\Omega \tag{3.37}$$

and

$$\begin{aligned}\frac{d}{d\tau}\left[l_{\Omega_\tau}\left(\overline{\mathbf{z}}_\tau\right)\right]\Big|_{\tau=0}=&\int_\Omega\left[\dot{f}^\alpha\overline{z}_\alpha\sqrt{a}+f^\alpha\dot{\overline{z}}_\alpha\sqrt{a}+f^\alpha\overline{z}_\alpha\left(\sqrt{a}\right)^{\cdot}\right]hd\Omega,\\&+\int_\Omega\left[\dot{f}^n\overline{w}\sqrt{a}+f^n\dot{\overline{w}}\sqrt{a}+f^n\overline{w}\left(\sqrt{a}\right)^{\cdot}\right]hd\Omega\\&-\int_\Omega\left[\left\{2\tau_0\dot{a}^{\alpha\beta}\varepsilon_{\alpha\beta}\left(\overline{\mathbf{z}}\right)+2\tau_0a^{\alpha\beta}\dot{\varepsilon}_{\alpha\beta}\left(\overline{\mathbf{z}}\right)\right\}\sqrt{a}\right]hd\Omega,\\&-\int_\Omega\left[2\tau_0a^{\alpha\beta}\varepsilon_{\alpha\beta}\left(\overline{\mathbf{z}}\right)\left(\sqrt{a}\right)^{\cdot}\right]hd\Omega,\end{aligned} \tag{3.38}$$

where

$$\begin{aligned}F\left(\mathbf{z},\overline{\mathbf{z}}\right)=&\left(C^{\alpha\beta\mu\lambda}h+2C_{\text{surf}}^{\alpha\beta\mu\lambda}\right)\varepsilon_{\alpha\beta}\left(\mathbf{z}\right)\varepsilon_{\mu\lambda}\left(\overline{\mathbf{z}}\right)\\&+\left(\frac{h^3}{12}C^{\alpha\beta\mu\lambda}+\frac{h^2}{2}C_{\text{surf}}^{\alpha\beta\mu\lambda}+2d_s\frac{1-\nu^2}{E}C^{\alpha\beta\mu\lambda}\right)\omega_{\alpha\beta}\left(\mathbf{z}\right)\omega_{\mu\lambda}\left(\overline{\mathbf{z}}\right)\\&+\left(C^{\alpha3\beta3}h+2C_{\text{surf}}^{\alpha3\beta3}\right)\gamma_\alpha\left(\mathbf{z}\right)\gamma_\beta\left(\overline{\mathbf{z}}\right)\end{aligned} \tag{3.39}$$

and

$$\begin{aligned}\dot{F}\left(\mathbf{z},\overline{\mathbf{z}}\right)=&\left(\dot{C}^{\alpha\beta\mu\lambda}h+2\dot{C}_{\text{surf}}^{\alpha\beta\mu\lambda}\right)\varepsilon_{\alpha\beta}\left(\mathbf{z}\right)\varepsilon_{\mu\lambda}\left(\overline{\mathbf{z}}\right)\\&+\left(\frac{h^3}{12}\dot{C}^{\alpha\beta\mu\lambda}+\frac{h^2}{2}\dot{C}_{\text{surf}}^{\alpha\beta\mu\lambda}+2d_s\frac{1-\nu^2}{E}\dot{C}^{\alpha\beta\mu\lambda}\right)\omega_{\alpha\beta}\left(\mathbf{z}\right)\omega_{\mu\lambda}\left(\overline{\mathbf{z}}\right)\\&+\left(\dot{C}^{\alpha3\beta3}h+2\dot{C}_{\text{surf}}^{\alpha3\beta3}\right)\gamma_\alpha\left(\mathbf{z}\right)\gamma_\beta\left(\overline{\mathbf{z}}\right)+\left(C^{\alpha\beta\mu\lambda}h+2C_{\text{surf}}^{\alpha\beta\mu\lambda}\right)\dot{\varepsilon}_{\alpha\beta}\left(\mathbf{z}\right)\varepsilon_{\mu\lambda}\left(\overline{\mathbf{z}}\right)\\&+\left(\frac{h^3}{12}C^{\alpha\beta\mu\lambda}+\frac{h^2}{2}C_{\text{surf}}^{\alpha\beta\mu\lambda}+2d_s\frac{1-\nu^2}{E}C^{\alpha\beta\mu\lambda}\right)\dot{\omega}_{\alpha\beta}\left(\mathbf{z}\right)\omega_{\mu\lambda}\left(\overline{\mathbf{z}}\right)\\&+\left(C^{\alpha3\beta3}h+2C_{\text{surf}}^{\alpha3\beta3}\right)\dot{\gamma}_\alpha\left(\mathbf{z}\right)\gamma_\beta\left(\overline{\mathbf{z}}\right)+\left(C^{\alpha\beta\mu\lambda}h+2C_{\text{surf}}^{\alpha\beta\mu\lambda}\right)\varepsilon_{\alpha\beta}\left(\mathbf{z}\right)\dot{\varepsilon}_{\mu\lambda}\left(\overline{\mathbf{z}}\right)\\&+\left(\frac{h^3}{12}C^{\alpha\beta\mu\lambda}+\frac{h^2}{2}C_{\text{surf}}^{\alpha\beta\mu\lambda}+2d_s\frac{1-\nu^2}{E}C^{\alpha\beta\mu\lambda}\right)\omega_{\alpha\beta}\left(\mathbf{z}\right)\dot{\omega}_{\mu\lambda}\left(\overline{\mathbf{z}}\right)\end{aligned}$$

$$+\left(C^{\alpha 3\beta 3}h+2C_{\text{surf}}^{\alpha 3\beta 3}\right)\gamma_{\alpha}\left(\mathbf{z}\right)\dot{\gamma}_{\beta}\left(\overline{\mathbf{z}}\right) \tag{3.40}$$

The material derivatives of the membrane strain tensor, bending strain tensor and shear strain tensor are obtained as

$$\dot{\varepsilon}_{\alpha\beta}\left(\mathbf{z}\right)=sym\left[u_{\alpha,\beta}-\Gamma_{\alpha\beta}^{\mu}u_{\mu}-b_{\alpha\beta}w\right]$$

$$=sym\left[\dot{u}_{\alpha,\beta}-\dot{\Gamma}_{\alpha\beta}^{\mu}u_{\mu}-\Gamma_{\alpha\beta}^{\mu}\dot{u}_{\mu}-\dot{b}_{\alpha\beta}w-b_{\alpha\beta}\dot{w}\right]=\varepsilon_{\alpha\beta}\left(\dot{\mathbf{z}}\right)+\varepsilon_{\alpha\beta}^{V}\left(\mathbf{z}\right), \tag{3.41}$$

$$\dot{\omega}_{\alpha\beta}\left(\mathbf{z}\right)=sym\left[\psi_{\alpha,\beta}-\Gamma_{\alpha\beta}^{\mu}\psi_{\mu}\right]^{\cdot}$$

$$=sym\left[\dot{\psi}_{\alpha,\beta}-\dot{\Gamma}_{\alpha\beta}^{\mu}\psi_{\mu}-\Gamma_{\alpha\beta}^{\mu}\dot{\psi}_{\mu}\right]=\omega_{\alpha\beta}\left(\dot{\mathbf{z}}\right)+\omega_{\alpha\beta}^{V}\left(\mathbf{z}\right), \tag{3.42}$$

and

$$\dot{\gamma}_{\alpha}\left(\mathbf{z}\right)=sym\left[w_{,\alpha}+\psi_{\alpha}+b_{\alpha}^{\lambda}u_{\lambda}\right]^{\cdot}$$

$$=sym\left[\dot{w}_{,\alpha}+\dot{\psi}_{\alpha}+\dot{b}_{\alpha}^{\lambda}u_{\lambda}+b_{\alpha}^{\lambda}\dot{u}_{\lambda}\right]=\gamma_{\alpha}\left(\dot{\mathbf{z}}\right)+\gamma_{\alpha}^{V}\left(\mathbf{z}\right), \tag{3.43}$$

in which $\varepsilon(\dot{\mathbf{z}}),\omega(\dot{\mathbf{z}})$ and $\gamma(\dot{\mathbf{z}})$ implicitly depend on the design through $\dot{\mathbf{z}}$. $\varepsilon^{V}(\mathbf{z})$, $\omega^{V}(\mathbf{z})$ and $\gamma^{V}(\mathbf{z})$ represent the explicitly dependent part that can be computed from both the state variable **z** and the design velocity **V**. Note that the operations of partial derivative with respect to the NURBS parametric coordinates and the material derivatives are commutative. The material derivative of variational equation for structural elasticity problem is given as

$$\frac{d}{d\tau}\left[a_{\Omega}\left(\mathbf{z}_{\tau},\overline{\mathbf{z}}_{\tau}\right)\right]\Big|_{\tau=0}\equiv a\left(\dot{\mathbf{z}},\overline{\mathbf{z}}\right)+a\left(\mathbf{z},\dot{\overline{\mathbf{z}}}\right)+a'_{V}\left(\mathbf{z},\overline{\mathbf{z}}\right)$$

$$=l\left(\dot{\overline{\mathbf{z}}}\right)+l'_{V}\left(\overline{\mathbf{z}}\right)\equiv\frac{d}{d\tau}\left[l_{\Omega}\left(\overline{\mathbf{z}}_{\tau}\right)\right]\Big|_{\tau=0}. \tag{3.44}$$

In $\mathbf{E}^2$ space the following relation holds such as $\hat{\overline{\mathbf{z}}}\in\overline{Z}$, $\dot{\hat{\overline{\mathbf{z}}}}\in\overline{Z}$ and $\dot{\hat{\overline{\mathbf{z}}}}=\dot{\overline{z}}_i\mathbf{g}^i+\overline{z}_i\dot{\mathbf{g}}^i$. Since $\hat{\overline{\mathbf{z}}}=\overline{z}_i\mathbf{g}^i=0$ on Γ^D and the basis vectors $\mathbf{g}^i$ are

linearly independent, $\overline{z}_i = 0$ on Γ^D. Therefore, $\dot{\overline{\mathbf{z}}} = (\dot{\overline{z}}_i) \in \overline{Z}$, and following equation is valid.

$$a\left(\mathbf{z}, \dot{\overline{\mathbf{z}}}\right) = l\left(\dot{\overline{\mathbf{z}}}\right). \tag{3.45}$$

The design sensitivity formulation using a direct differentiation method is finally derived as

$$\begin{aligned} a\left(\dot{\mathbf{z}}, \overline{\mathbf{z}}\right) &= l'_V\left(\overline{\mathbf{z}}\right) - a'_V\left(\mathbf{z}, \overline{\mathbf{z}}\right) \\ &= l'_V\left(\overline{\mathbf{z}}\right) - \left\{a'_{mV}\left(\mathbf{z}, \overline{\mathbf{z}}\right) + a'_{bV}\left(\mathbf{z}, \overline{\mathbf{z}}\right) + a'_{sV}\left(\mathbf{z}, \overline{\mathbf{z}}\right)\right\} \end{aligned} \tag{3.46}$$

Considering only membrane strain tensor and substituting equation (3.41) into equation (3.37) yields equation (3.47). Substituting equations (3.42) and (3.43) into equation (3.37) yields bending strain tensor equation (3.48) and shear strain tensor equation (3.49).

$$\begin{aligned} a'_{mV}\left(\mathbf{z}, \overline{\mathbf{z}}\right) &= \int_\Omega \left[\left(\dot{C}^{\alpha\beta\mu\lambda} h + 2\dot{C}^{\alpha\beta\mu\lambda}_{\text{surf}}\right)\varepsilon_{\alpha\beta}\left(\mathbf{z}\right)\varepsilon_{\mu\lambda}\left(\overline{\mathbf{z}}\right)\sqrt{a}\right] d\Omega, \\ &+ \int_\Omega \left[\left(C^{\alpha\beta\mu\lambda} h + 2C^{\alpha\beta\mu\lambda}_{\text{surf}}\right)\varepsilon_{\alpha\beta}\left(\mathbf{z}\right)\varepsilon_{\mu\lambda}\left(\overline{\mathbf{z}}\right)\left(\sqrt{a}\right)^{\cdot}\right] d\Omega, \\ &+ \int_\Omega \left[\left(C^{\alpha\beta\mu\lambda} h + 2C^{\alpha\beta\mu\lambda}_{\text{surf}}\right)\left\{\left(-\dot{\Gamma}^n_{\alpha\beta} u_n - \dot{b}_{\alpha\beta} w\right)\varepsilon_{\mu\lambda}\left(\overline{\mathbf{z}}\right)\right\}\sqrt{a}\right] d\Omega, \\ &+ \int_\Omega \left[\left(C^{\alpha\beta\mu\lambda} h + 2C^{\alpha\beta\mu\lambda}_{\text{surf}}\right)\left\{\varepsilon_{\alpha\beta}\left(\mathbf{z}\right)\left(-\dot{\Gamma}^n_{\mu\lambda}\overline{u}_n - \dot{b}_{\mu\lambda}\overline{w}\right)\right\}\sqrt{a}\right] d\Omega, \end{aligned} \tag{3.47}$$

$$\begin{aligned} a'_{bV}\left(\mathbf{z}, \overline{\mathbf{z}}\right) &= \int_\Omega \left[\left(\frac{h^3}{12}\dot{C}^{\alpha\beta\mu\lambda} + \frac{h^2}{2}\dot{C}^{\alpha\beta\mu\lambda}_{\text{surf}} + 2d_s\frac{1-\nu^2}{E}\dot{C}^{\alpha\beta\mu\lambda}\right)\omega_{\alpha\beta}\left(\mathbf{z}\right)\omega_{\mu\lambda}\left(\overline{\mathbf{z}}\right)\sqrt{a}\right] d\Omega, \\ &+ \int_\Omega \left[\left(\frac{h^3}{12}C^{\alpha\beta\mu\lambda} + \frac{h^2}{2}C^{\alpha\beta\mu\lambda}_{\text{surf}} + 2d_s\frac{1-\nu^2}{E}C^{\alpha\beta\mu\lambda}\right)\omega_{\alpha\beta}\left(\mathbf{z}\right)\omega_{\mu\lambda}\left(\overline{\mathbf{z}}\right)\left(\sqrt{a}\right)^{\cdot}\right] d\Omega, \\ &+ \int_\Omega \left[\left(\frac{h^3}{12}C^{\alpha\beta\mu\lambda} + \frac{h^2}{2}C^{\alpha\beta\mu\lambda}_{\text{surf}} + 2d_s\frac{1-\nu^2}{E}C^{\alpha\beta\mu\lambda}\right)\left\{-\dot{\Gamma}^n_{\alpha\beta}\psi_n\omega_{\mu\lambda}\left(\overline{\mathbf{z}}\right)\right\}\sqrt{a}\right] d\Omega, \\ &+ \int_\Omega \left[\left(\frac{h^3}{12}C^{\alpha\beta\mu\lambda} + \frac{h^2}{2}C^{\alpha\beta\mu\lambda}_{\text{surf}} + 2d_s\frac{1-\nu^2}{E}C^{\alpha\beta\mu\lambda}\right)\left\{-\omega_{\alpha\beta}\left(\mathbf{z}\right)\dot{\Gamma}^n_{\mu\lambda}\overline{\psi}_n\right\}\sqrt{a}\right] d\Omega, \end{aligned} \tag{3.48}$$

and

$$a'_{sV}(\mathbf{z},\overline{\mathbf{z}}) = \int_\Omega \left\{ \left(\dot{C}^{\alpha 3\beta 3} h + 2\dot{C}^{\alpha 3\beta 3}_{\text{surf}} \right) \gamma_\alpha(\mathbf{z}) \gamma_\beta(\overline{\mathbf{z}}) \sqrt{a} \right\} d\Omega.$$

$$+ \int_\Omega \left\{ \left(C^{\alpha 3\beta 3} h + 2C^{\alpha 3\beta 3}_{\text{surf}} \right) \gamma_\alpha(\mathbf{z}) \gamma_\beta(\overline{\mathbf{z}}) \left(\sqrt{a} \right)^{\cdot} \right\} d\Omega.$$

$$+ \int_\Omega \left[\left(C^{\alpha 3\beta 3} h + 2C^{\alpha 3\beta 3}_{\text{surf}} \right) \left\{ \dot{b}^n_\alpha u_n \gamma_\beta(\overline{\mathbf{z}}) + \gamma_\alpha(\mathbf{z}) \dot{b}^n_\beta \overline{u}_n \right\} \sqrt{a} \right] d\Omega. \tag{3.49}$$

Here, *m*, *b* and *s* mean explicitly dependent part of membrane, bending, and shear, respectively. From equation (3.38), explicitly dependent part of load linear form is obtained as

$$l'_V(\overline{\mathbf{z}}) = \int_\Omega \left[\dot{f}^\alpha \overline{z}_\alpha \sqrt{a} + f^\alpha \overline{z}_\alpha \left(\sqrt{a} \right)^{\cdot} + \dot{f}^n \overline{w} \sqrt{a} + f^n \overline{w} \left(\sqrt{a} \right)^{\cdot} \right] d\Omega.$$

$$- \int_\Omega \left[\left\{ 2\tau_0 \dot{a}^{\alpha\beta} \varepsilon_{\alpha\beta}(\overline{\mathbf{z}}) + 2\tau_0 a^{\alpha\beta} \left(-\dot{\Gamma}^n_{\alpha\beta} \overline{u}_n - \dot{b}_{\alpha\beta} \overline{w} \right) \right\} \sqrt{a} \right] d\Omega,$$

$$- \int_\Omega \left[2\tau_0 a^{\alpha\beta} \varepsilon_{\alpha\beta}(\overline{\mathbf{z}}) \left(\sqrt{a} \right)^{\cdot} \right] d\Omega, \tag{3.50}$$

3.2.3 Shape design sensitivity analysis considering nonlocal effects

By using the material derivative formula given in equation (3.36), the variational equation considering nonlocal effects is differentiated with respect to τ as

$$\frac{d}{d\tau} \left[a_{\Omega_\tau} \left(\mathbf{z}_\tau, \overline{\mathbf{z}}_\tau \right) \right] \Big|_{\tau=0} = \int_\Omega \dot{F}(\mathbf{z},\overline{\mathbf{z}}) \sqrt{a} d\Omega + \int_\Omega F(\mathbf{z},\overline{\mathbf{z}}) \left(\sqrt{a} \right)^{\cdot} d\Omega \tag{3.51}$$

and

$$\frac{d}{d\tau} \left[l_{\Omega_\tau} \left(\overline{\mathbf{z}}_\tau \right) \right] \Big|_{\tau=0} = \int_\Omega \left[\dot{f}^\alpha \overline{z}_\alpha \sqrt{a} + f^\alpha \dot{\overline{z}}_\alpha \sqrt{a} + f^\alpha \overline{z}_\alpha \left(\sqrt{a} \right)^{\cdot} \right] d\Omega$$

$$+ \int_\Omega \left[\dot{f}^n \overline{w} \sqrt{a} + f^n \dot{\overline{w}} \sqrt{a} + f^n \overline{w} \left(\sqrt{a} \right)^{\cdot} \right] d\Omega$$

$$+ \mu \int_\Omega \left[\left\{ \dot{f}^\alpha_{,\beta} \varepsilon_{\alpha\beta}(\overline{\mathbf{z}}) + \dot{f}^n \omega_{\alpha\alpha}(\overline{\mathbf{z}}) + \dot{f}^n_{,\alpha} \gamma_\alpha(\overline{\mathbf{z}}) \right\} \sqrt{a} \right] d\Omega$$

$$+\mu\int_{\Omega}\left[\left\{f^{\alpha}_{,\beta}\dot{\varepsilon}_{\alpha\beta}(\bar{\mathbf{z}})+f^{n}\dot{\omega}_{\alpha\alpha}(\bar{\mathbf{z}})+f^{n}_{,\alpha}\dot{\gamma}_{\alpha}(\bar{\mathbf{z}})\right\}\sqrt{a}\right]d\Omega \tag{3.52}$$

where

$$F(\mathbf{z},\bar{\mathbf{z}})=C^{\alpha\beta\mu\lambda}h\varepsilon_{\alpha\beta}(\mathbf{z})\varepsilon_{\mu\lambda}(\bar{\mathbf{z}})+\frac{h^3}{12}C^{\alpha\beta\mu\lambda}\omega_{\alpha\beta}(\mathbf{z})\omega_{\mu\lambda}(\bar{\mathbf{z}})$$
$$+C^{\alpha 3\beta 3}h\gamma_{\alpha}(\mathbf{z})\gamma_{\beta}(\bar{\mathbf{z}}) \tag{3.53}$$

and

$$\dot{F}(\mathbf{z},\bar{\mathbf{z}})=\dot{C}^{\alpha\beta\mu\lambda}h\varepsilon_{\alpha\beta}(\mathbf{z})\varepsilon_{\mu\lambda}(\bar{\mathbf{z}})+\frac{h^3}{12}\dot{C}^{\alpha\beta\mu\lambda}\omega_{\alpha\beta}(\mathbf{z})\omega_{\mu\lambda}(\bar{\mathbf{z}})$$
$$+\dot{C}^{\alpha 3\beta 3}h\gamma_{\alpha}(\mathbf{z})\gamma_{\beta}(\bar{\mathbf{z}})+C^{\alpha\beta\mu\lambda}h\dot{\varepsilon}_{\alpha\beta}(\mathbf{z})\varepsilon_{\mu\lambda}(\bar{\mathbf{z}})$$

$$+\frac{h^3}{12}C^{\alpha\beta\mu\lambda}\dot{\omega}_{\alpha\beta}(\mathbf{z})\omega_{\mu\lambda}(\bar{\mathbf{z}})+C^{\alpha 3\beta 3}h\dot{\gamma}_{\alpha}(\mathbf{z})\gamma_{\beta}(\bar{\mathbf{z}})$$
$$+C^{\alpha\beta\mu\lambda}h\varepsilon_{\alpha\beta}(\mathbf{z})\dot{\varepsilon}_{\mu\lambda}(\bar{\mathbf{z}})+\frac{h^3}{12}C^{\alpha\beta\mu\lambda}\omega_{\alpha\beta}(\mathbf{z})\dot{\omega}_{\mu\lambda}(\bar{\mathbf{z}})$$
$$+C^{\alpha 3\beta 3}h\gamma_{\alpha}(\mathbf{z})\dot{\gamma}_{\beta}(\bar{\mathbf{z}}) \tag{3.54}$$

The material derivatives of the membrane strain tensor, bending strain tensor and shear strain tensor are obtained as equations (3.41)-(3.43). Considering only membrane strain tensor and substituting equation (3.41) into equation (3.51) yields equation (3.55). Substituting equations (3.42) and (3.43) into equation (3.51) yields bending strain tensor equation (3.56) and shear strain tensor equation (3.57), respectively.

$$a'_{mV}(\mathbf{z},\bar{\mathbf{z}})=\int_{\Omega}\left[\dot{C}^{\alpha\beta\mu\lambda}h\varepsilon_{\alpha\beta}(\mathbf{z})\varepsilon_{\mu\lambda}(\bar{\mathbf{z}})\sqrt{a}\right]d\Omega,$$
$$+\int_{\Omega}\left[C^{\alpha\beta\mu\lambda}h\varepsilon_{\alpha\beta}(\mathbf{z})\varepsilon_{\mu\lambda}(\bar{\mathbf{z}})\left(\sqrt{a}\right)^{\cdot}\right]d\Omega,$$
$$+\int_{\Omega}\left[C^{\alpha\beta\mu\lambda}h\left\{\left(-\dot{\Gamma}^{n}_{\alpha\beta}u_n-\dot{b}_{\alpha\beta}w\right)\varepsilon_{\mu\lambda}(\bar{\mathbf{z}})\right\}\sqrt{a}\right]d\Omega$$
$$+\int_{\Omega}\left[C^{\alpha\beta\mu\lambda}h\left\{\varepsilon_{\alpha\beta}(\mathbf{z})\left(-\dot{\Gamma}^{n}_{\mu\lambda}\bar{u}_n-\dot{b}_{\mu\lambda}\bar{w}\right)\right\}\sqrt{a}\right]d\Omega, \tag{3.55}$$

$$a'_{bV}(\mathbf{z},\bar{\mathbf{z}}) = \int_\Omega \left[\frac{h^3}{12} \dot{C}^{\alpha\beta\mu\lambda} \omega_{\alpha\beta}(\mathbf{z}) \omega_{\mu\lambda}(\bar{\mathbf{z}}) \sqrt{a} \right] d\Omega,$$

$$+ \int_\Omega \left[\frac{h^3}{12} C^{\alpha\beta\mu\lambda} \omega_{\alpha\beta}(\mathbf{z}) \omega_{\mu\lambda}(\bar{\mathbf{z}}) \left(\sqrt{a}\right)^{\cdot} \right] d\Omega,$$

$$+ \int_\Omega \left[\frac{h^3}{12} C^{\alpha\beta\mu\lambda} \left\{ -\dot{\Gamma}^n_{\alpha\beta} \psi_n \omega_{\mu\lambda}(\bar{\mathbf{z}}) - \omega_{\alpha\beta}(\mathbf{z}) \dot{\Gamma}^n_{\mu\lambda} \bar{\psi}_n \right\} \sqrt{a} \right] d\Omega, \qquad (3.56)$$

and

$$a'_{sV}(\mathbf{z},\bar{\mathbf{z}}) = \int_\Omega \left\{ \dot{C}^{\alpha 3 \beta 3} h \gamma_\alpha(\mathbf{z}) \gamma_\beta(\bar{\mathbf{z}}) \sqrt{a} \right\} d\Omega.$$

$$+ \int_\Omega \left\{ C^{\alpha 3 \beta 3} h \gamma_\alpha(\mathbf{z}) \gamma_\beta(\bar{\mathbf{z}}) \left(\sqrt{a}\right)^{\cdot} \right\} d\Omega.$$

$$+ \int_\Omega \left[C^{\alpha 3 \beta 3} h \left\{ \dot{b}^n_\alpha u_n \gamma_\beta(\bar{\mathbf{z}}) + \gamma_\alpha(\mathbf{z}) \dot{b}^n_\beta \bar{u}_n \right\} \sqrt{a} \right] d\Omega. \qquad (3.57)$$

Here, *m*,*b* and *s* mean explicitly dependent part of membrane, bending, and shear, respectively. From equation (3.52), explicitly dependent part of load linear form is obtained as

$$l'_V(\bar{\mathbf{z}}) = \int_\Omega \left[\dot{f}^\alpha \bar{z}_\alpha \sqrt{a} + f^\alpha \bar{z}_\alpha \left(\sqrt{a}\right)^{\cdot} + \dot{f}^n \bar{w} \sqrt{a} + f^n \bar{w} \left(\sqrt{a}\right)^{\cdot} \right] d\Omega.$$

$$+ \int_\Omega \left[\left\{ \mu \left(f^\alpha_{,\beta} \varepsilon_{\alpha\beta}(\bar{\mathbf{z}}) + f^n \omega_{\alpha\alpha}(\bar{\mathbf{z}}) + f^n_{,\alpha} \gamma_\alpha(\bar{\mathbf{z}}) \right) \right\} \left(\sqrt{a}\right)^{\cdot} \right] d\Omega$$

$$+ \int_\Omega \left[\mu \left(\dot{f}^\alpha_{,\beta} \varepsilon_{\alpha\beta}(\bar{\mathbf{z}}) + \dot{f}^n \omega_{\alpha\alpha}(\bar{\mathbf{z}}) + \dot{f}^n_{,\alpha} \gamma_\alpha(\bar{\mathbf{z}}) \right) \left(\sqrt{a}\right) \right] d\Omega$$

$$+ \int_\Omega \left[\mu \left(f^\alpha_{,\beta} \left(-\dot{\Gamma}^\mu_{\alpha\beta} \bar{u}_\mu - \dot{b}_{\alpha\beta} \bar{w} \right) + f^n \left(-\dot{\Gamma}^\mu_{\alpha\alpha} \bar{\psi}_\mu \right) \right) \left(\sqrt{a}\right) \right] d\Omega$$

$$+ \int_\Omega \left[\mu f^n_{,\alpha} \left(\dot{b}^\lambda_\alpha \bar{u}_\lambda \right) \left(\sqrt{a}\right) \right] d\Omega \qquad (3.58)$$

Chapter 4. Numerical Examples

4.1 Beam structures in nanoscale

4.1.1 Surface elasticity of silver nanowires under a concentrated force

To validate the developed method experimentally, three-point bending test of silver nanowires using AFM are performed. Continuum formulation considering surface effects in nanoscale is introduced for the theoretical analysis of silver nanowires under a concentrated force. Since nonlocal theory does not capture the variation of cross sectional area and size effects cannot be predicted for bending of a nanobeam under a concentrated force, which is called paradox, nonlocal theory is not considered for the theoretical analysis of silver nanowires. Several researchers neglect the effect of the deflection due to shear and considered the beam as a straight one ignoring initial deflection. (Jing et al, 2006) In this research, shear effects and initial deflection of a beam will also be ignored for simplicity. Governing equation of a straight beam considering surface effects in nanoscale is rewritten as

$$(EI)^{*}\frac{d^{4}w}{dx^{4}}+2\tau_{0}D\frac{d^{2}w}{dx^{2}}-q(x)=0 \tag{4.1}$$

where *(EI)** is effective rigidity and is obtained by

$$(EI)^{*}=EI+\frac{\pi}{8}E_{s}D^{3}+2d_{s}D \tag{4.2}$$

and E_s is surface modulus and D is diameter of circular nanowire. A constant concentrated load F is applied at midpoint of the beam. For a fixed-fixed nanowire boundary condition, following force equilibrium at x=0 is considered as

$$-\left(EI_2+\frac{\pi}{8}E_sD^3\right)\left.\frac{d^3w}{dx^3}\right|_{x=0}=F/2 \tag{4.3}$$

Exact displacement field without considering τ_0 is expressed as

$$w=\frac{F(3L-4x)x^2}{48(EI)^*},\quad x\in[0,L/2] \tag{4.4}$$

Exact displacement field with considering τ_0 is expressed as

$$w=\frac{F}{4\tau_0 D}\left[x-\frac{L}{\sqrt{\eta}}\tanh\left(\sqrt{\eta}/4\right)-\frac{L}{\sqrt{\eta}}\frac{\sinh\left(\sqrt{\eta}x/L-\sqrt{\eta}/4\right)}{\cosh\left(\sqrt{\eta}/4\right)}\right] \tag{4.5}$$

Setting x to $L/2$ yields exact maximum deflection at midpoint as

$$\delta_{\max}=\frac{F}{4\tau_0 D}\left[\frac{L}{2}-\frac{2L}{\sqrt{\eta}}\tanh\left(\sqrt{\eta}/4\right)\right] \tag{4.6}$$

where η is obtained as

$$\eta=2\tau^0 DL^2/(EI)^*. \tag{4.7}$$

Effective Young's modulus is obtained from maximum deflection as

$$E_{eff}=\frac{L^3F}{3\pi D^4\delta_{\max}} \tag{4.8}$$

Detailed derivation of exact displacement may refer to He and Lilley (2008).

As a further development, design sensitivities of maximum deflection with respect to diameter and length are given, respectively. Derivative of maximum deflection with respect to D is given as

$$\frac{\partial\delta_{\max}}{\partial D}=\frac{-F}{4\tau_0 D^2}\left[\frac{L}{2}-\frac{2L}{\sqrt{\eta}}\tanh\left(\sqrt{\eta}/4\right)\right]$$

$$+\frac{F}{4\tau_0 D}\left[-\frac{2L}{\sqrt{\eta}}\operatorname{sech}^2\left(\sqrt{\eta}/4\right)\frac{1}{8\sqrt{\eta}}\frac{\partial\eta}{\partial D}\right] \tag{4.9}$$

where

$$\frac{\partial \eta}{\partial D} = \frac{-128\tau^0 L^2 \left(3ED^2 + 16E_s D\right)}{\pi\left(ED^3 + 8E_s D^2\right)^2} \tag{4.10}$$

Derivative of maximum deflection with respect to L is given as

$$\frac{\partial \delta_{\max}}{\partial L} = \frac{F}{4\tau_0 D}\left[\frac{1}{2} - \frac{2}{\sqrt{\eta}}\tanh\left(\sqrt{\eta}/4\right)\frac{\partial \eta}{\partial L}\right]$$

$$-\frac{F}{4\tau_0 D}\left[\frac{2L}{\sqrt{\eta}}\left(\operatorname{sech}^2\left(\sqrt{\eta}/4\right)\frac{1}{8\sqrt{\eta}}\frac{\partial \eta}{\partial L}\right)\right] \tag{4.11}$$

where

$$\frac{\partial \eta}{\partial L} = \frac{256\tau^0 L}{E\pi D^3 + 8\pi E_s D^2} \tag{4.12}$$

Figure 4.1 shows the effect of the surface stress on the effective Young's modulus. For the (001) silver, surface elasticity values from atomistic calculations of τ_0=0.89 and E_s=1.22 are used. (Miller and Shenoy 2000) The silver nanowire length used in the calculation is 1 μm and the diameter of silver nanowire is 35 nm. The size dependence of the effective Young's modulus is observed by considering surface effects.

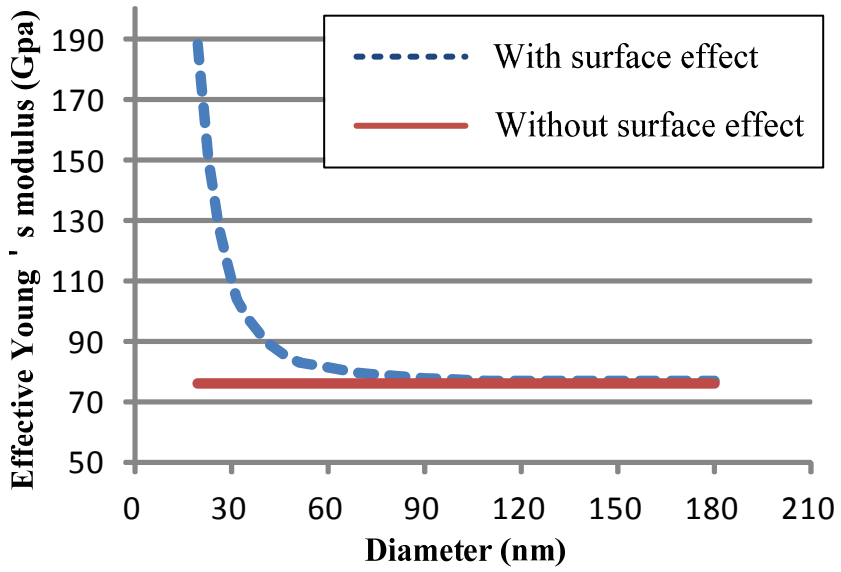

Figure 4.1 Effect of the surface stress on the effective Young's modulus

Table 4.1

Comparison of maximum displacement of silver nanowire under concentrated load considering surface effects

	(a) Exact displacement	(b) Numerical displacement	Ratio (b)/(a)
Quadratic FEA	0.7318	0.7089	96.87 (%)
Quadratic IGA		0.7262	99.23 (%)

The numerical maximum displacement using quadratic FEA and IGA are compared with exact maximum displacement as shown in table 4.1. Total number of DOFs used for each numerical analysis is 18. The IGA gives more accurate results than the conventional FEA, even same DOFs is used.

Table 4.2

Comparison of sizing design sensitivity of maximum displacement with respect to the diameter of silver nanowire under concentrated load considering surface effects

	(a) Exact sensitivity	(b) Analytical sensitivity	Ratio (b)/(a)
Quadratic FEA	-3.4834E+07	-3.3579E+07	96.40 (%)
Quadratic IGA		-3.4444E+07	98.88 (%)

Table 4.3

Comparison of shape design sensitivity of maximum displacement with respect to the length of silver nanowire under concentrated load considering surface effects

	(a) Exact sensitivity	(b) Analytical sensitivity	Ratio (b)/(a)
Quadratic FEA	9.3361E+05	8.9726E+05	96.11 (%)
Quadratic IGA		9.2174E+05	98.73 (%)

Analytical sizing and shape sensitivity using quadratic FEA and IGA are compared with exact sensitivity as shown in table 4.2 and 4.3, respectively. Comparing with the exact sensitivity, analytical sensitivity of IGA shows better agreement than FEA case.

4.1.2 Three point bending test of silver nanowires using AFM

The elastic modulus of silver nanowires is measured by performing three-point bending tests on nanowires suspended over substrate with etched holes. Figure 4.2 shows the image of used AFM (Brucker, Dimension Icon-PT SM) instrument. A small force is applied to the middle point along its suspended length using AFM cantilever tip. The cantilever (Veeco, RTESPA-300) here with calibrated resonance frequency 300 kHz and normal spring constants of 40 N/m was used. Silver nanowires were purchased from Plasmachem. Three kinds of silver nanowires dispersion in Ethanol were purchased, respectively. Average diameters of each silver nanowire are 40 nm, 100 nm and 200 nm, and its length is up to 50 μm.

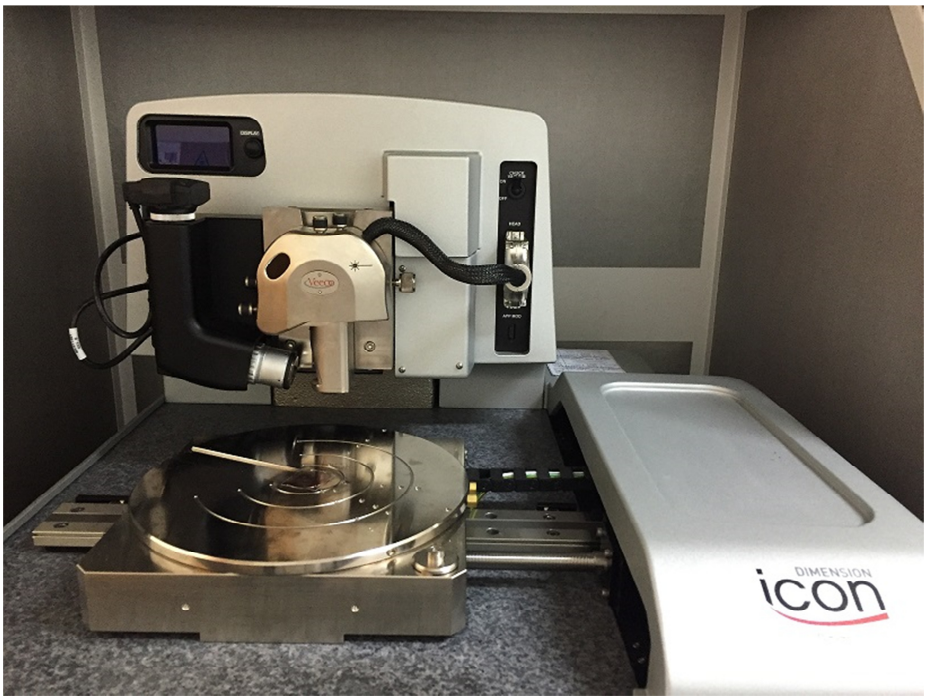

Figure 4.2 AFM instrument (Brucker, Dimension Icon-PT SM)

Figure 4.3 AFM cantilever (Veeco, RTESPA-300)

Figure 4.4 Silver nanowires (Plasmachem)

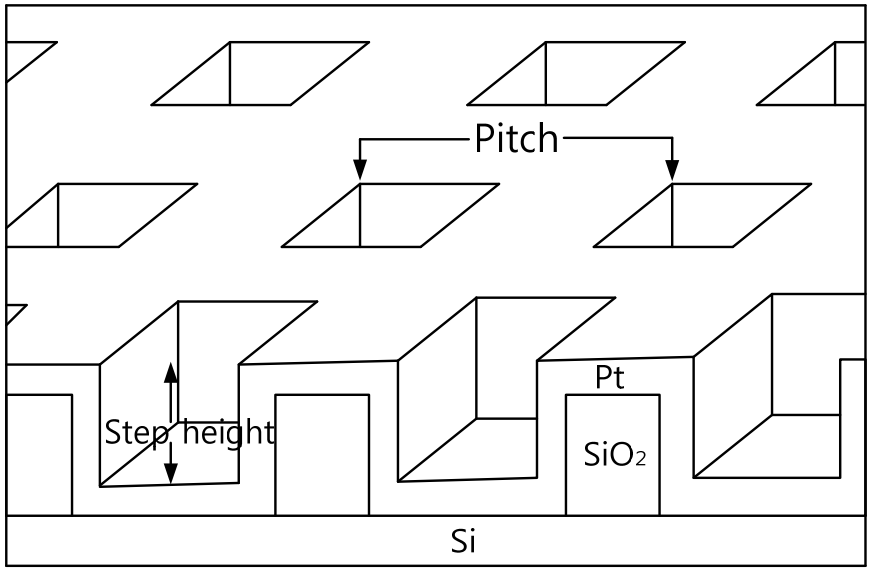

Figure 4.5 AFM calibration grating for the three point bending test

Flat substrate with a hole is required for the three-point bending test of silver nanowire. AFM calibration grating is well-defined structures designed as an auxiliary aid for the monitoring of sophisticated imaging tools, so it provides reliable testing substrate for three-point bending test of silver nanowire. Used AFM calibration grating (Bruker, APCS-0099) in this study is a multi-area calibration artifact and pitch size is selectable from 2 μm to 15 μm. Therefore, we can choose suspended nanowire with appropriate length depending on the diameter to prevent initial deflection of nanowire. Several drops of the silver nanowires ethanol solution were dispersed onto the substrate. For eliminating problems associated with initial deflection of silver nanowire, the selection of reasonable ratio between the nanowire length and its diameter is required. $L/D>15$ is avoided to prevent initial deflection of silver nanowire. Since overlapped suspension of the silver nanowires is not desirable in three-point bending test, silver nanowire solution with low concentration is required for observing individual silver nanowire. After the experiment, substrate is

rinsed several times with ethyl alcohol, acetone and DI water for another experiment.

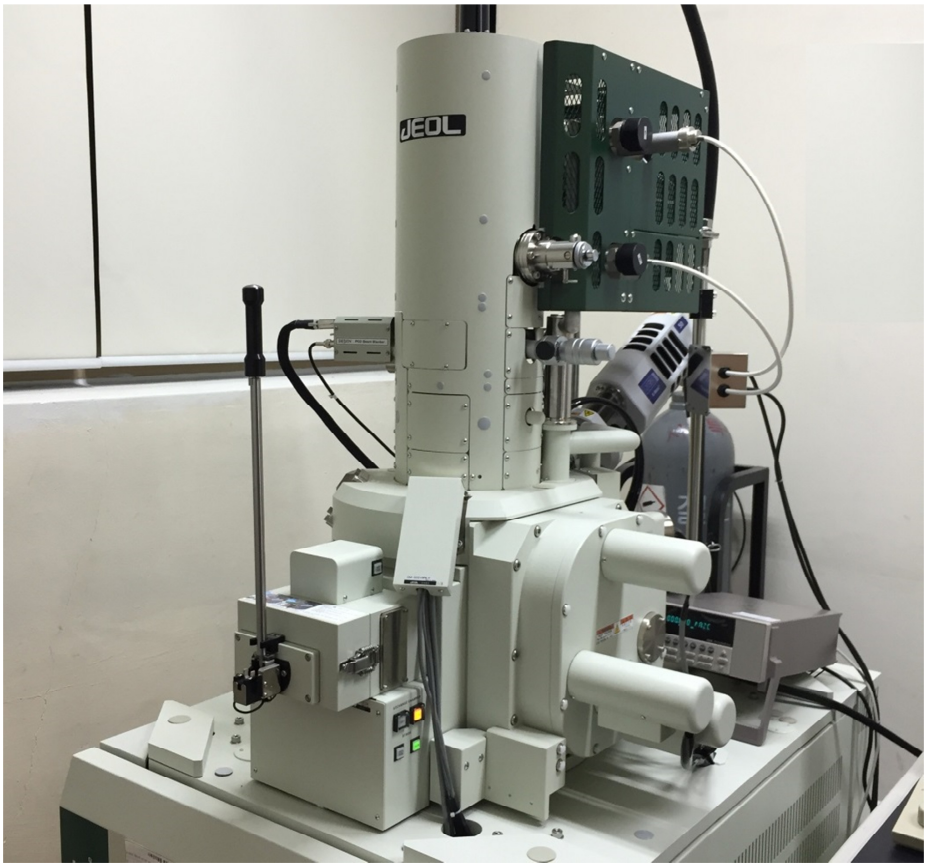

Figure 4.6 SEM instrument (Jeol, JSM-7100F)

Figure 4.6 shows the image of used scanning electron microscope (SEM) (Jeol, JSM-7100F). Before measurement with AFM, SEM images were obtained in advance. This is because scan speed of SEM is much faster than AFM and matching the same position between two instruments is possible by setting a coordinates using periodicity of AFM calibration gratings. We can observe that some of silver nanowires were well-suspended over the holes using SEM. The AFM images of the sample were scanned first at low magnification as shown in figure 4.7 to obtain overall view and an

individual nanowire of interest suspended over one hole is selected. Once a suspended nanowire was selected, an AFM image at higher magnification was carefully taken. Figure 4.8 and 4.9 show the images of the sample at higher magnification by SEM and AFM, respectively. We can observe same region is matched exactly by setting a coordinates using periodicity of AFM calibration gratings. Since alignment is not perfectly orthogonal, suspended length L is measured for each nanowire.

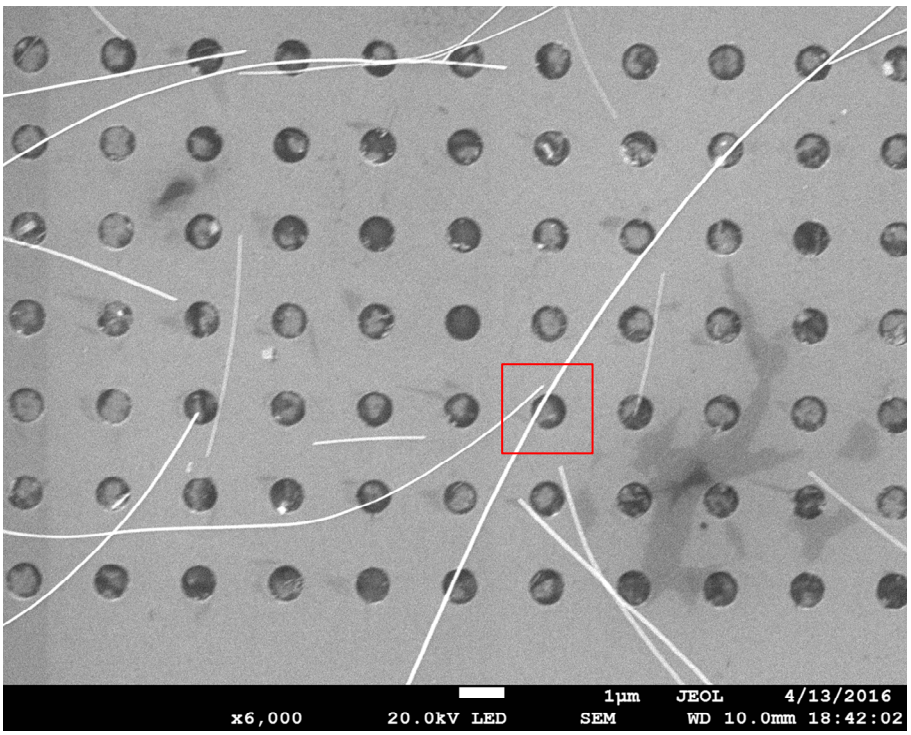

Figure 4.7 SEM image of a suspended silver nanowire at lower magnification

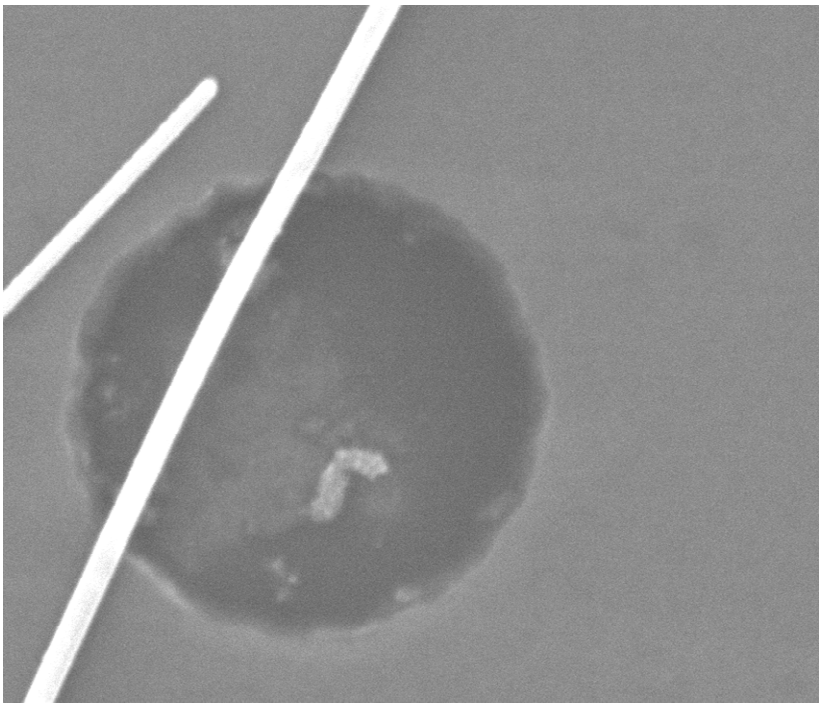

Figure 4.8 The SEM images of the sample at higher magnification

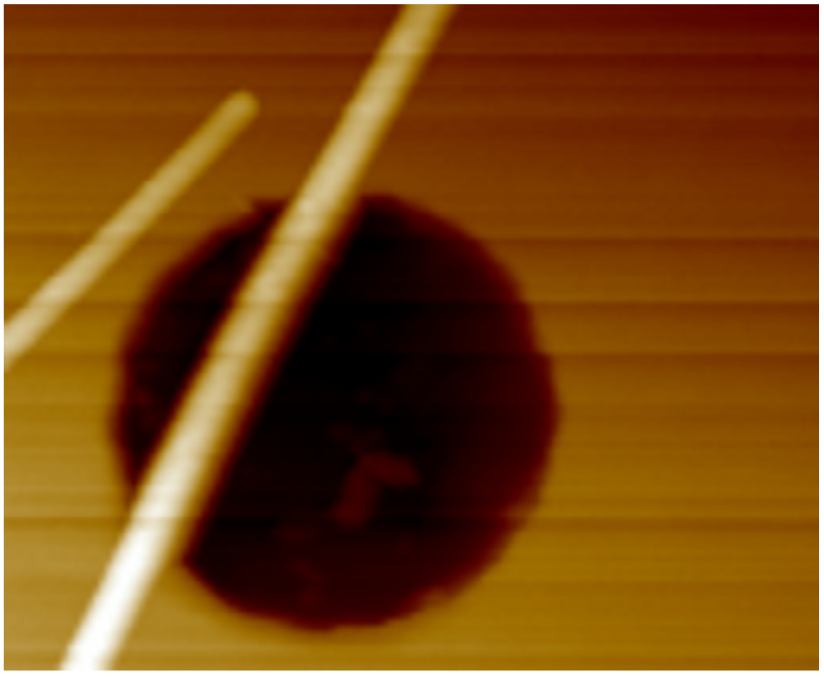

Figure 4.9 The AFM images of the sample at higher magnification

The diameter D of the nanowire was measured by cross sectional view in the AFM image. Figure 4.10 shows enlarged silver nanowire image and its cross sectional view. Since height information is more reliable than surface image due to the limitation of plane resolution, measured maximum height is set to diameter of circular nanowire. The AFM tip was then moved to the midpoint of the nanowire of interest. Special procedures are not required for fastening the nanowires to the substrate. Adhesion of the silver nanowire to the substrate was sufficiently strong to prevent any lift-off, providing a clamped beam assumption.

Assuming that a force is applied at the midpoint of the beam and induces a deflection, we measure force-displacement curves from the midpoint of the suspended nanowire. The photodetector deflection sensitivity allows conversion from the raw photodiode signal to deflection of the cantilever. Deflection sensitivity is dependent on the cantilever type and laser alignment. The sensitivity must be calibrated on a hard substrate before accurate deflection data is obtained. As we know the parameters such as deflection sensitivity and spring constant, the deflection voltage-time curves can be converted to real force-distance curves. The cantilever tip was brought to contact with the sample by a piezoelectric actuator, resulting in both cantilever deflection and the bending of the suspended nanowire simultaneously. Therefore, the slope of force-deflection curves gives the spring constant of combined structure of cantilever and nanowire k_{wc} which is related to the spring constant of the nanowire k_w and that of cantilever k_c by

$$k_w = \frac{k_c k_{wc}}{k_c - k_{wc}} \tag{4.13}$$

k_c is given value depending on the cantilever type. Figure 4.11 shows the example of determining spring constant of nanowire k_w from spring

constant of combined structure k_{wc} and that of cantilever k_c as given in equation (4.13).

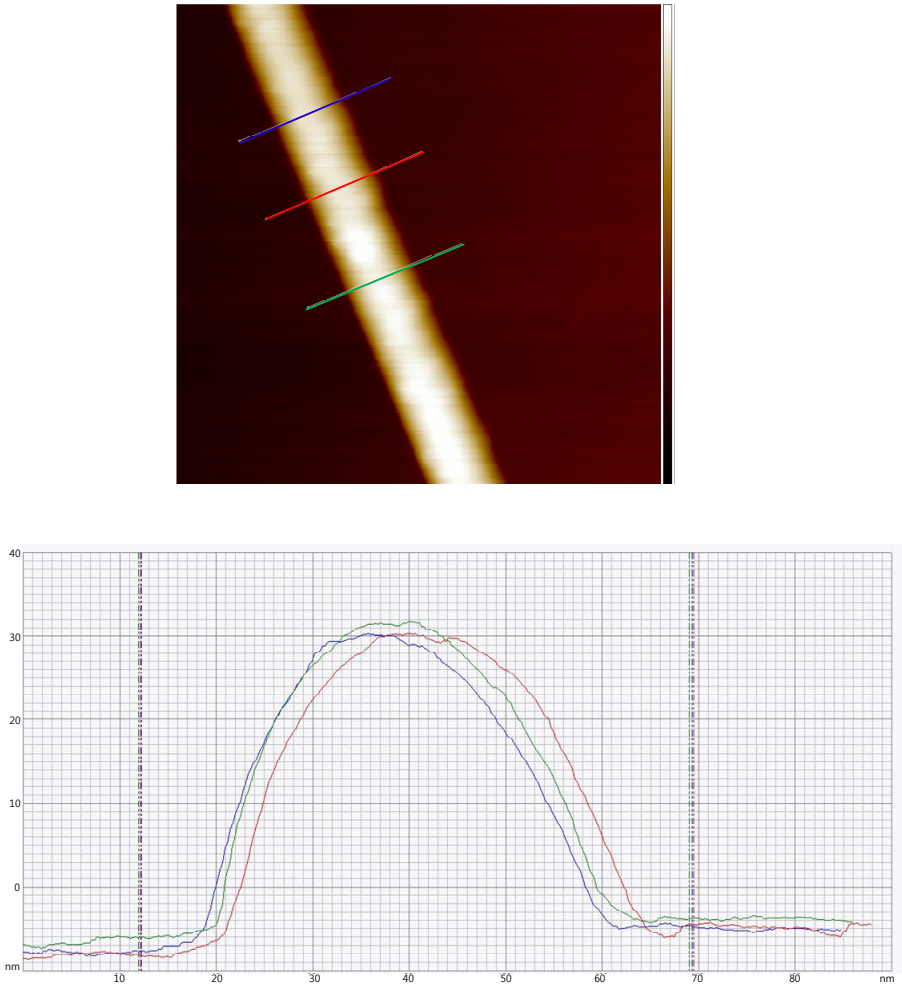

Figure 4.10 The AFM images and its cross sectional view

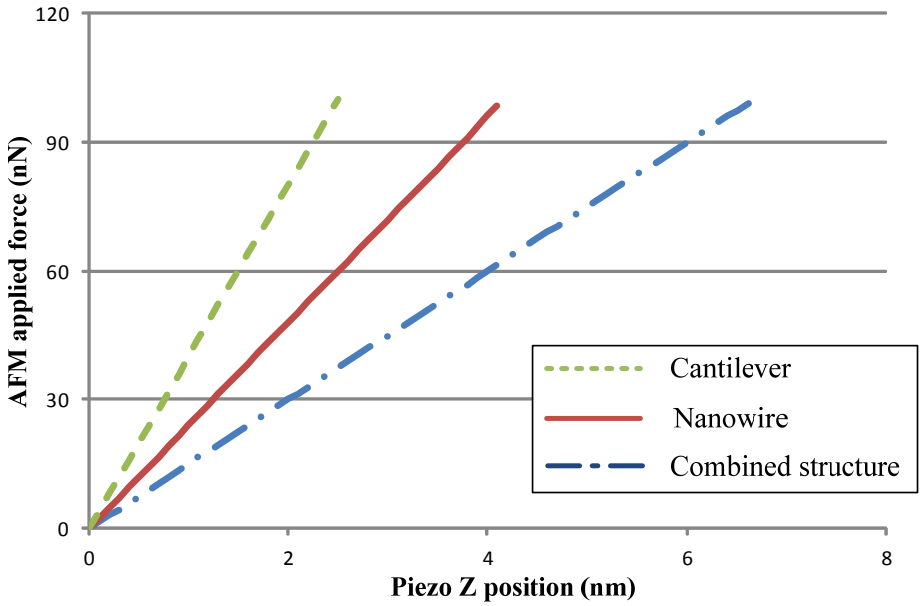

Figure 4.11 Determination of spring constant of nanowire from three-point bending test

4.1.3 Experimental validation for surface elasticity of silver nanowires

Surface elasticity with high order surface effect

Generally, according to the beam theory for a three-point bending test, the effective Young's modulus considering size effects is given by equation (4.8). L, D and I are obtained from the geometry information and stiffness k_s=F/δ_{max} is determined by three point bending test. Figure 4.12 shows the effective Young's modulus obtained from three point bending test as the function of the diameters of silver nanowires. Obtained experimental data is compared with experimental data by Jing et al. (2006) and it shows fairly good agreement.

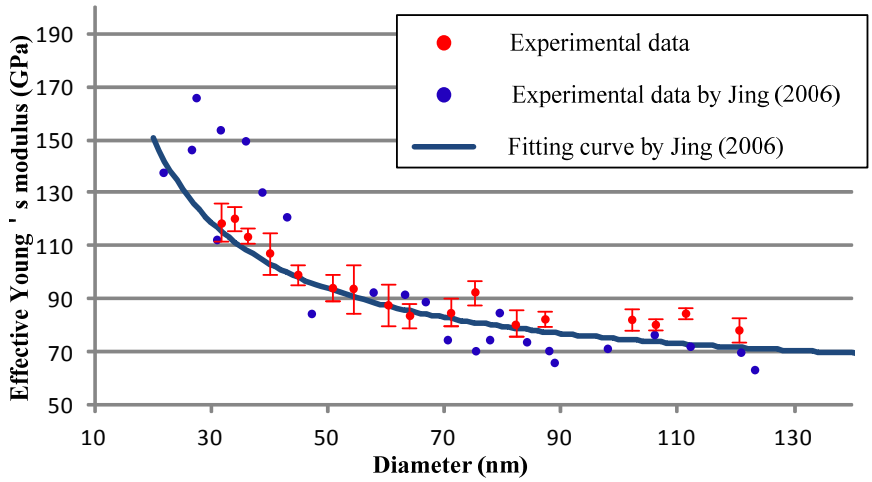

Figure 4.12 Variation of the effective Young's modulus with the diameters of silver nanowires

Jing et al. (2006) obtained a relationship between the effective Young's modulus and the diameters of nanowires through three point bending test. Using the relation that total elastic energy is the sum of bulk and surface elastic energy, they derived following approximated relation between original Young's modulus E and effective Young's modulus E_{eff} as

$$E_{eff} = E + \frac{8}{D}E_s + \frac{8L^2}{5D^3}\tau_0. \tag{4.14}$$

Under the assumption that L is approximately $14D$, fitting curve given in equation (4.14) gives optimized surface parameters, E=56 GPa, E_s=8.7 N/m and τ_0=5.8 N/m. Cuenot et al. (2004) also presented optimized surface parameters E=67.5 GPa and τ_0=3.09 N/m from their own experimental results. These values are different from E=76 GPa, E_s=1.22 N/m and τ_0=0.89 N/m which are obtained from MD simulation results. Jing et al. (2006) analyzed the reasons for the differences of surface parameters obtained by MD simulation and experimental results are due to surface roughness and

surface oxidation layer. Since rough surface may consume more energy than a smooth surface during the deformation, surface parameters obtained from experimental data are larger than those obtained from MD Simulation, which deals with silver nanowires having smooth surface.

He et al. (2008) present the approach using the generalized Young-Laplace equation to study the influence of surface effect on the three point bending test of silver nanowires. Concentrated force 1.0 nN is applied at the mid-point and maximum displacement w_{max} at the mid-point is obtained. The effective Young's modulus is obtained as $FL^3/[192(EI)^* w_{max}]$. For the theoretical calculation, surface parameters are given as E=76 GPa, E_s=1.22 N/m and τ_0=0.89 N/m which are obtained from MD simulation results. Under the assumption that L is 1.0 μm, theoretical solutions are compared with experimental results obtained by Jing et al. (2006) and it shows fairly good agreement between them. However, suspended length in the experiment by Jing et al. (2006) is approximately 14D, not 1.0 μm for all diameters. To account for the differences between experimental results and theory, some researchers discuss that surface moment with finite thickness affects the surface energy. The surface elasticity theory developed by Gurtin and Murdoch (1975) is based on the idea that two-dimensional membrane with zero-thickness is bonded to the bulk, so it has no flexural resistance. However, there is an intrinsic flexural resistance of the surface since the surface region has a few atomic layers thickness. Chiu and Chen (2011) suggest high-order surface stress which considers not only the effect of in-plane membrane surface stresses, but also the surface moments induced from the non-uniform surface stress across the layer thickness. It allows that the stress could be linearly varying across the layer thickness, which results in

surface stress as well as surface moment. The generalized Young-Laplace equation with high-order surface stress is obtained as

$$\left[EI+\frac{\pi D^3}{8}E_s+2d_sD\right]\frac{\partial^4 w}{\partial x^4}-2\tau_0 D\frac{\partial^2 w}{\partial x^2}+q(x)=0. \tag{4.15}$$

The surface bending stiffness parameter d_s is estimated approximately from the reported value of E_s via the relation $d_s \approx O(h^2)E_s$ where h is surface layer thickness. In their study, d_s is estimated as about 1.0~5.0 (10^{-14}N·m) for silver nanowires. They show that developed method predicts more accurate results with the experimental data reported by Jing et al. (2006) compared with original method without high-order surface stress.

Validation of surface elasticity theory by experimental data

For the validation of surface elasticity theory using obtained experimental data, dependence on diameter as well suspended length is observed. The DSA formulation considering surface effects is also validated through experimental data. Firstly, surface parameters E_s and τ_0 in generalized Young-Laplace equation are modified for best fitting experimental data and their values are compared with those suggested by Cuenot et al. (2004) and Jing et al. (2006). Since τ_0 is dominant in calculation of surface energy, Cuenot et al. (2004) ignored E_s term. Average error of effective Young's modulus between theory and experimental data is defined as

$$e=\frac{1}{N_{\text{exp}}}\sum_{i=1}^{N_{\text{exp}}}\frac{E_{\text{exp},i}-E_{\text{theory},i}}{E_{\text{theory},i}} \tag{4.16}$$

where N_{exp} is total number of experimental data, $E_{\text{exp},i}$ and $E_{\text{theory},i}$ are i-th effective Young's modulus obtained by experiments and that obtained by theory, respectively. Average error of effective Young's modulus is minimized when E_s is 6.59 and τ_0 is 3.51. Surface parameters obtained from

experimental data in present study are comparable with those obtained by other researchers as shown in table 4.4.

Table 4.4

Comparison of surface parameters obtained from other papers

	MD Simulation	Cuenot (2004)	Jing (2006)	Present study
E (GPa)	76.0	67.5	56.0	76.0
E_s (N/m)	1.22	-	8.7	6.59
τ_0 (N/m)	0.89	3.09	5.8	4.81

Secondly, the dependence on surface bending stiffness parameter d_s of effective Young's modulus is observed. Chiu and Chen (2011) estimated d_s as 1.0~5.0 (10^{-14}N·m) for silver nanowires. Figure 4.13 shows the graph of average error of effective Young's modulus between theory and experimental data as function of surface bending stiffness parameter d_s. Average error of effective Young's modulus is minimized when surface bending stiffness parameter is 3.2 (10^{-14}N·m).

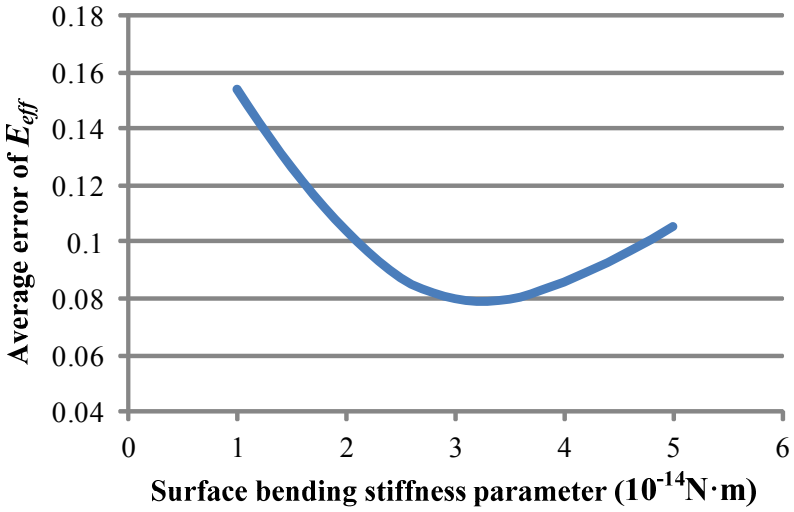

Figure 4.13 The graph of the average error of effective Young's modulus as function of surface bending stiffness parameter

Figure 4.14 shows the graph of effective Young's modulus as function of suspended length and diameter of silver nanowires. Red graph shows effective Young's modulus without surface effects. Size dependence of effective Young's modulus is not observed. In yellow graph, Size dependence on effective Young's modulus is observed under the assumption that surface parameters are E=76 GPa, E_s=1.22 N/m and τ_0=0.89 N/m which are obtained from MD simulation results. Especially, size dependence is not clear for low suspended length on the given surface parameter. Green graph shows best fitting surface of experimental data under the modified surface parameters, E=76 GPa, E_s=6.59 N/m and τ_0=3.71 N/m. In blue graph, best fitting surface minimizing average error of effective Young's modulus is obtained by considering surface bending stiffness parameter d_s=3.2 (10^{-14}N·m). Average error of effective Young's modulus in the modified surface parameter case (which is green) and high order surface effects case (which is blue) are obtained as 9.82(%) and 7.89(%), respectively. Figure 4.15 shows

the graph of the effective Young's modulus as function of diameter of silver nanowires with suspended length. We can observe that best fitting surface is obtained by considering high order surface effects. With the modified surface parameters, effective Young's modulus is too high or too small for some range.

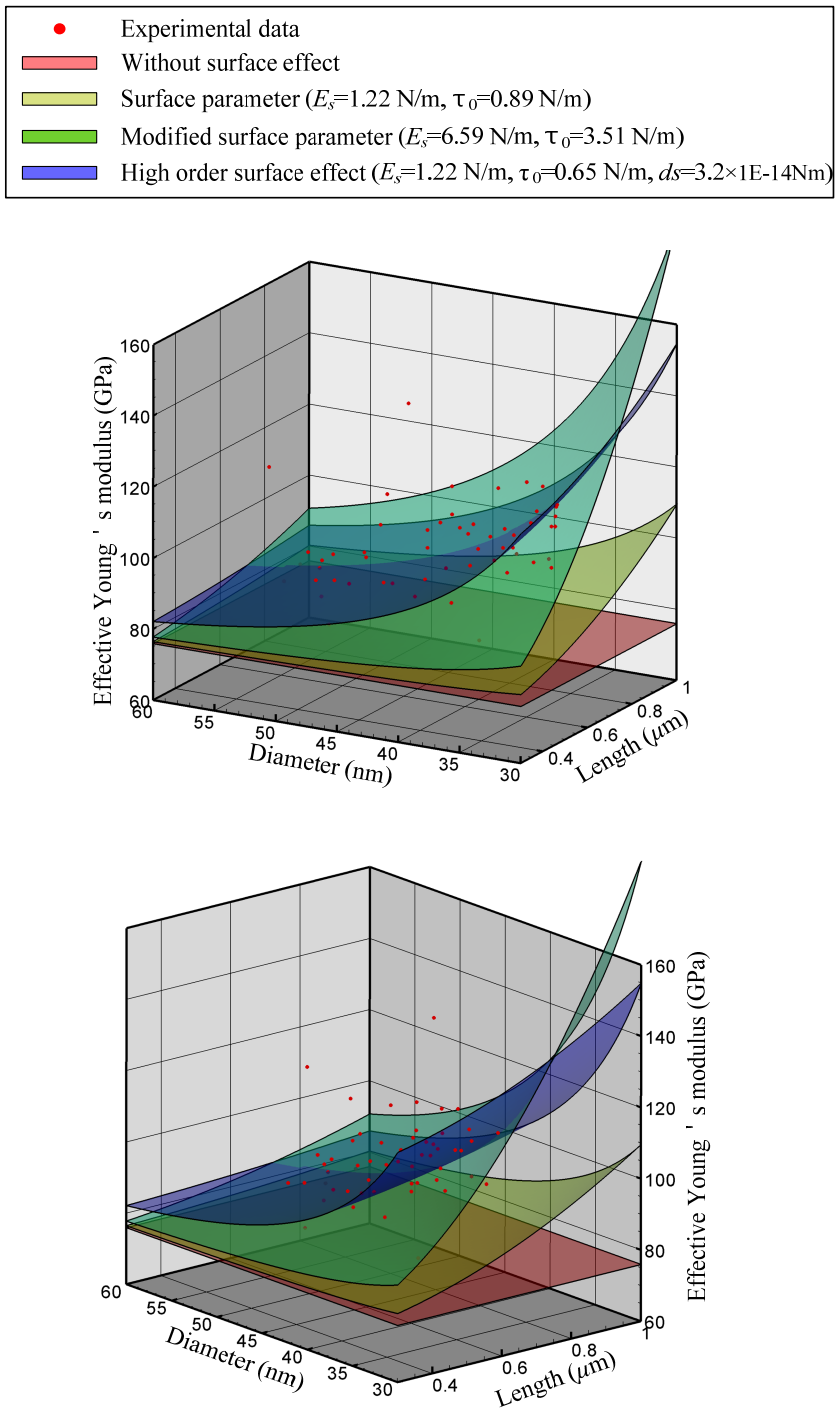

Figure 4.14 The graph of the effective Young's modulus as function of suspended length and diameter of silver nanowires

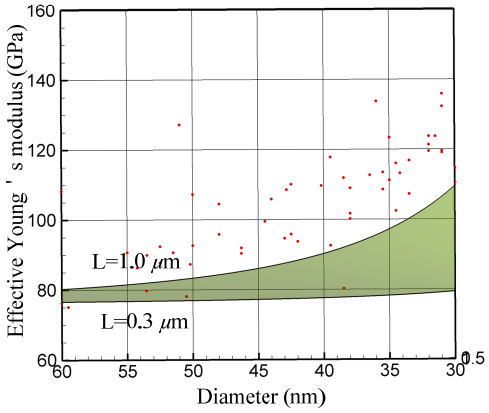

(a) Surface parameter (E_s=1.22 N/m, τ_0=0.89 N/m)

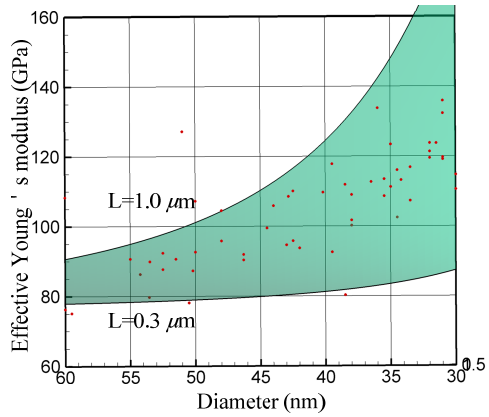

(b) Modified surface parameter (E_s=6.59 N/m, τ_0=3.51 N/m)

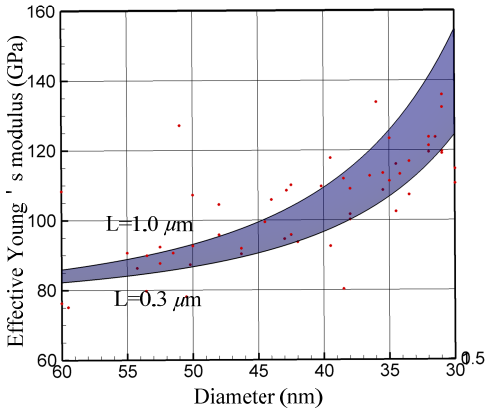

(c) High order surface effect (E_s=1.22 N/m, τ_0=0.89 N/m, ds=3.2×1E-14Nm)

Figure 4.15 The graph of the effective Young's modulus as function of diameter of silver nanowires with suspended length

Validation of DSA considering surface effect

For the validation of DSA based on continuum-based theory considering surface effects, the design sensitivity values obtained from fitting curve of experimental data are compared with those obtained by DSA. Surface parameters for best fitting curve of experimental data E=76 GPa, E_s =1.22 N/m, τ_0=0.89 N/m and ds=3.2 (1E-14Nm) are used. Figure 4.16 and 4.17 show the design sensitivity of maximum displacement with respect to diameter and suspended length of silver nanowires, respectively. Fitting curve of experimental data is obtained using second order polynomial function and design sensitivity is calculated from fitting curve. Design sensitivity obtained by fittig curve of experimental data are compared with that of theoretical calculation in table 4.5. Acceptable agreement is obtained between the design sensitivity of maximum displacement obtained by experiments and the results obtained by DSA considering surface effects. Therefore, we can conclude that developed DSA formulation considering surface effects in nanoscale is validated experimentally through three point bending test of silver nanowires.

Table 4.5 Comparison of DSA between experiments and theory

	(a) Fitting curve by experiments	(b) Without surface effect	(c) With surface effect	Ratio (b)/(a) (%)	Ratio (c)/(a) (%)
$\left.\frac{\partial w}{\partial D}\right\|_{D=37\,nm}$	-9.100E-03	-1.742E-02	-9.493E-03	191.43	104.32
$\left.\frac{\partial w}{\partial L}\right\|_{D=0.5\,\mu m}$	2.771E-04	4.108E-04	3.044E-04	148.25	109.85

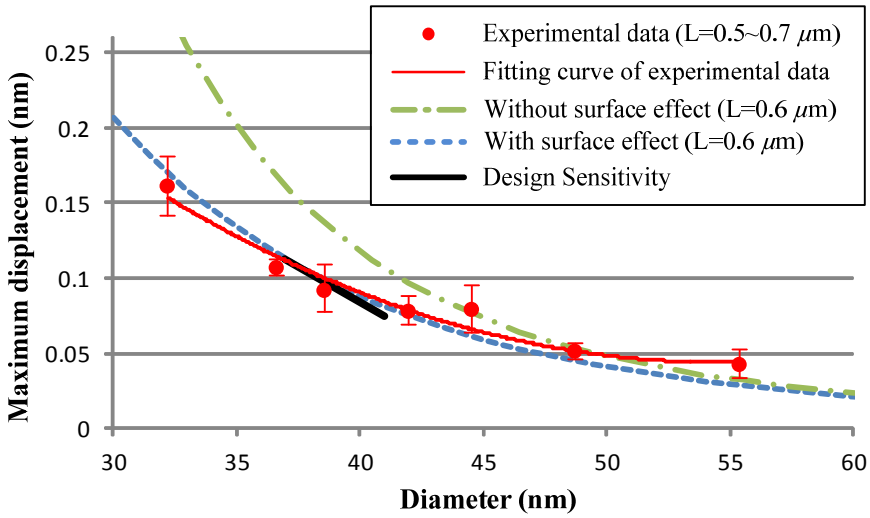

Figure 4.16 Validation of design sensitivity of maximum displacement with respect to diameter of silver nanowires

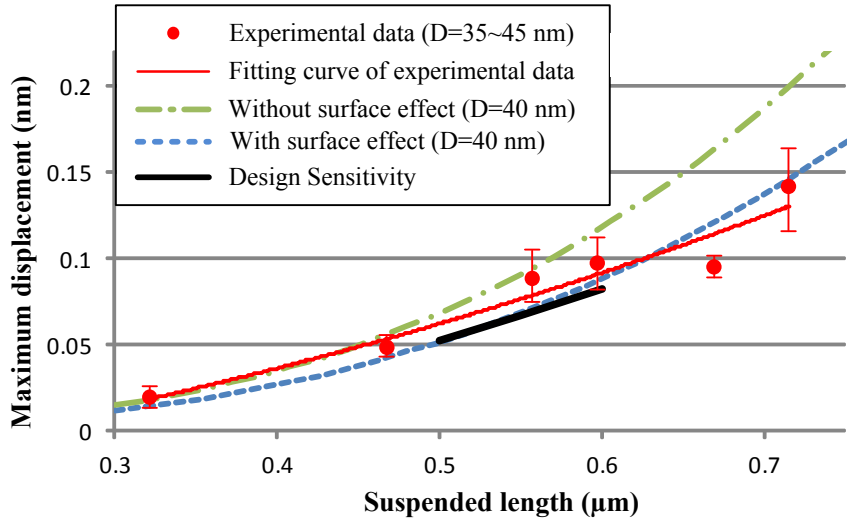

Figure 4.17 Validation of design sensitivity of maximum displacement with respect to suspended length of silver nanowires

4.2 Shell structures in nanoscale

4.2.1 Shape design optimization of parabolic arch: optimal height

Shape design optimization problem of parabolic arch in nanoscale under distributed load is considered. Shape design optimization is to find the optimal shape design which minimizes a certain objective functional while satisfying given constraints. In shape design optimization, the shape of physical domain must be treated as the design variable. In this example, design variable is the height of parabolic arch, and the objective of shape optimization is to minimize the total strain energy. The optimal shape for an arch under distributed load is known as parabola where bending moments vanish and the loads are carried by membrane forces only. There is infinite number of quadratic parabolas to be spanned between two points, and we want to find the optimal height of the parabola on the given width. Kiendl et al. (2014) discussed the exact optimal height of parabola, and we derived additional terms to reflect the surface effects in nanoscale. The total strain energy for the parabolic arch with surface effects is derived as

$$U(h)=\frac{1}{2(EA+4\mu_0+2\lambda_0)}\left\{q^2D^3\tilde{U}_1(h)+4\tau_0 qD^2\tilde{U}_2(h)+4\tau_0^2D\tilde{U}_3(h)\right\}, \tag{4.17}$$

where

$$\tilde{U}_1(h)=\frac{\sqrt{1+4h^2}\left(16h^3+10h\right)+3\sinh^{-1}(2h)}{32h^3}, \tag{4.18}$$

$$\tilde{U}_2(h)=\frac{4}{3}h+\frac{1}{h}, \tag{4.19}$$

and

$$\tilde{U}_3(h)=\sqrt{1+4h^2}+\frac{\sinh^{-1}(2h)}{2h}, \tag{4.20}$$

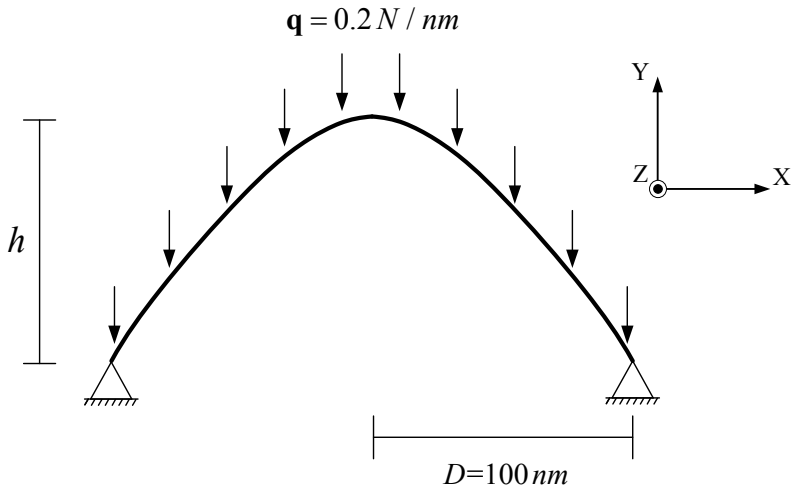

Figure 4.18 Model description of parabolic arch under distributed load

where μ_0, λ_0 and τ_0 are considered to apply the surface effects, q is the distributed load, h is the height of the parabolic arch and D is the half width of the arch. Since bending moments vanish in parabola, surface bending stiffness parameter d_s is not considered in this example. As D increases, the relative effect of τ_0 decreases. This is in accordance with the physical meanings that τ_0 have a larger influence on the small sized structure. Detailed derivation of equation (4.17) and its derivatives can be found in Appendix A. For the verification of numerical analysis results, numerical strain energy and its shape design sensitivity are compared with the exact solutions. The problem parameters are: D and h are 100 nm, q is 0.2 N/nm and thickness is 1 nm. The material is assumed as Si(100) under EAM potential (Miller and Shenoy 2000). Young's modulus E=107 GPa and surface Lame constants μ_0 is -2.7779, λ_0 is -4.4939 and residual surface stress τ_0 is 0.6056. To guarantee constant state throughout the z-direction, Poisson's ratio v is set to zero and unit width is assumed. Total number of DOFs is 245. The numerical strain energy using quadratic FEA and IGA are

compared with exact strain energy as shown in table 4.6 The IGA gives more accurate results than the conventional FEA, even same DOFs is used.

Table 4.6

Comparison of strain energy of parabolic arch under distributed load considering surface effects

	(a) Exact strain energy	(b) Numerical strain energy	Ratio (b)/(a)
Quadratic FEA	5.6210E-07	5.4607E-07	97.15 (%)
Quadratic IGA		5.5975E-07	99.58 (%)

The exact shape design sensitivity is obtained by differentiating equation (4.17) with respect to the design variable h, and the analytical sensitivity using quadratic FEA and IGA are compared with exact sensitivity as shown in table 4.7 Comparing with the exact sensitivity, analytical sensitivity of IGA shows better agreement than FEA case.

Table 4.7

Comparison of shape design sensitivity of strain energy with respect to the height of parabolic arch under distributed load considering surface effects

	(a) Exact shape design sensitivity	(b) Analytical shape design sensitivity	Ratio (b)/(a) (%)
Quadratic FEA	-5.5154E-08	-7.9957E-08	144.97
Quadratic IGA		-5.8937E-08	106.86

Exact optimal height is determined by the stationary point of strain energy given in equation (4.17). Since the parabola is in pure membrane state,

surface Lame constants affect only magnitude of total strain energy and do not affect the optimal height. Only residual surface stress affects the optimal design. Figure 4.19 shows the effect of the surface stress on the strain energy with parabolic height. If the height of the arch tends to zero, the strain energy become infinity. As the height of the arch tends to infinity, total volume of the domain becomes infinity. Therefore, there exists optimal height that minimizes total strain energy. Since the optimization problem is convex, it does not require any constraints to get an optimal solution.

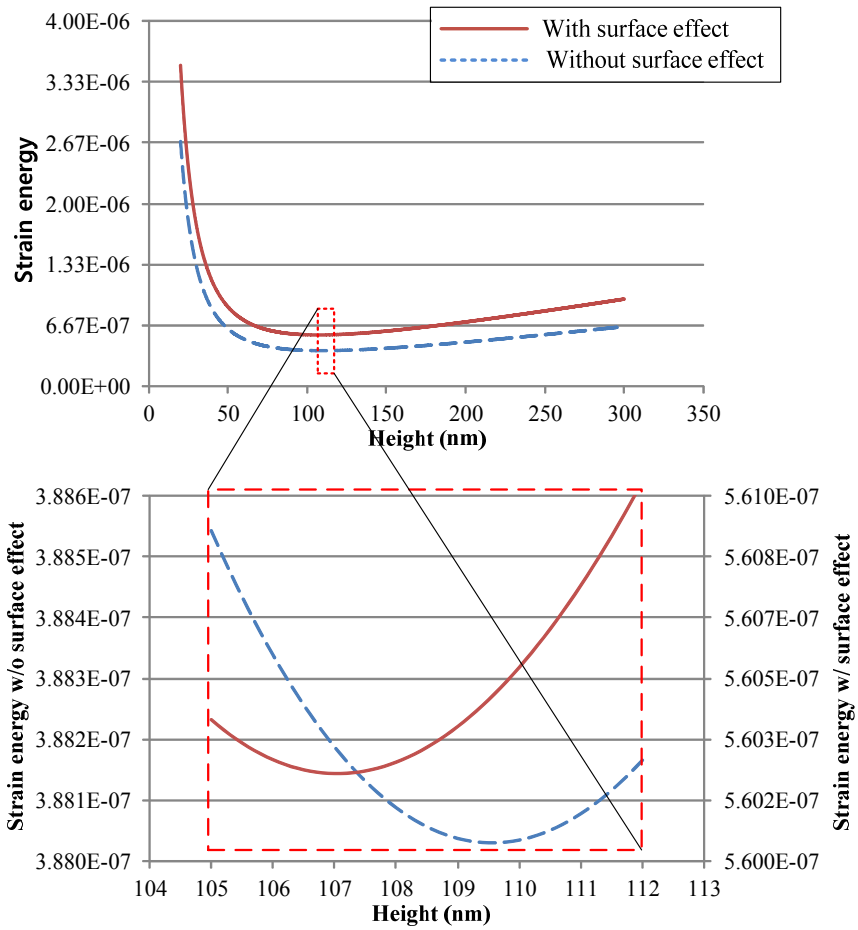

Figure 4.19 Effect of the surface stress on the strain energy with parabolic height

To solve the nonlinear mathematical optimization problem, a gradient-based optimization algorithm (MMFD; modified method of feasible direction) is used. Exact optimal height is obtained as 109.558 nm without surface effects and 107.044 nm with surface effects from exact solution. Strain energy caused by distributed load is convex for the height change, but strain energy caused by residual surface stress monotonically decreases as the height decreases. Therefore, if we consider the strain energy caused by residual surface stress additionally, lower height is more advantageous to obtain minimum strain energy. If residual surface stress is not considered, obtained stationary point has nothing to do with distributed load q. If residual surface stress is considered, stationary point is determined as function of the the q to τ_0 ratio. As the distributed load q increases, residual surface stress τ_0 affects less to the solution. In other words, the difference between the optimal height with and without surface effects increases as q to τ_0 ratio decreases. Figure 4.20-(a) shows the design model and design variable for the change of parabolic height and Figure 4.20-(b) shows analysis model. Because the shell structures require sufficient number of DOFs to ensure a reasonable structural response analysis, shape parametrization is essential to avoid wiggly design. In the present study, geometry is defined using some control points and analysis model is obtained through h-refinement of the design model keeping the geometry unchanged. Quadratic IGA is used and total number of DOFs used for analysis is 65. Figure 4.20-(c) shows initial and optimal design and the optimal height is obtained as 107.049 through 3 iteration. The number of iteration in optimization is same with that of DSA evaluation. Note that total number of function evaluation including structural analysis is larger than that of DSA evaluation.

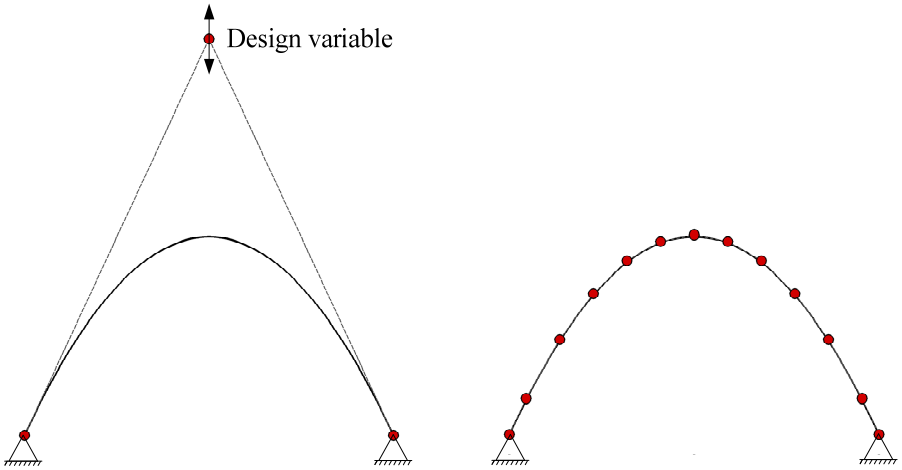

(a) Design model (b) Analysis model;

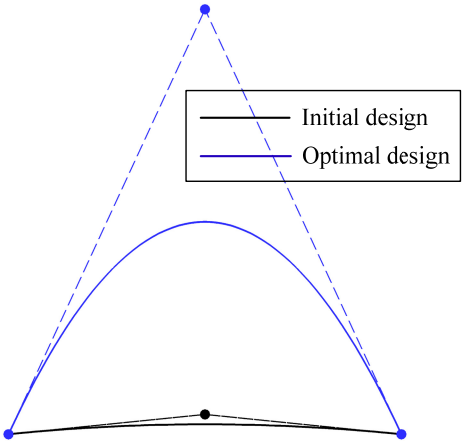

(c) Initial and optimal design

Figure 4.20 Shape design optimization of parabolic arch considering surface effects

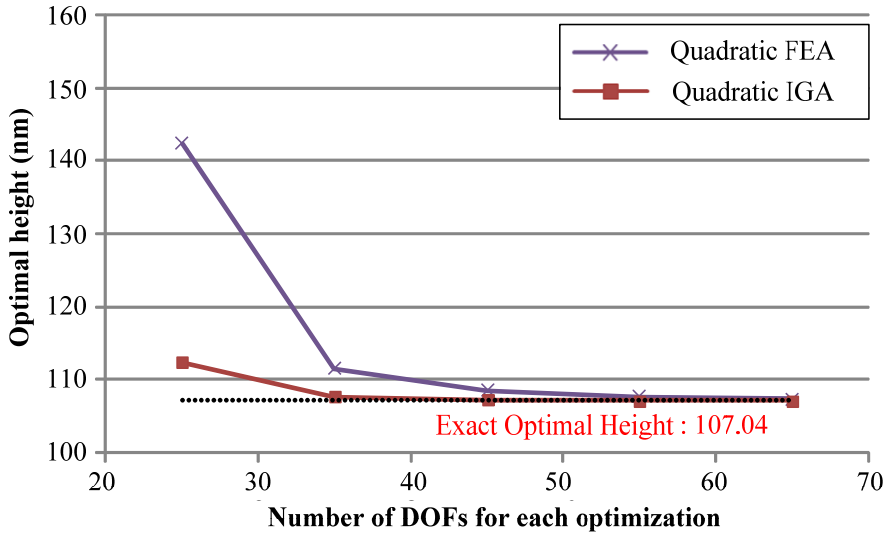

Figure 4.21 Convergence of optimal height of parabolic arch considering surface effects

Figure 4.21 shows the convergence of optimal height for FEA and IGA case as the number of DOFs for each optimization increases. It converges well to the exact optimal height with surface effects. Even basis functions with same order are used in both FEA and IGA cases, IGA shows better convergence rate than FEA case.

4.2.2 Shape design optimization of curved graphene: optimal curvature

As a second example for shell, shape design optimization problem of curved graphene under distributed load is considered. The design variable is the curvature of curved graphene which is constant over the whole domain. The objective of shape optimization is to minimize the total strain energy with constraints that allowable volume fraction is equal to the original one. Kosynkin et al. (2009) found that curved graphene with constant curvature

can be constructed by unzipping carbon nanotubes, and the size of width, length and curvature of the graphene can be obtained as we want from the specific carbon nanotubes. Curved graphene is modeled as circular arch shell shown in figure 4.22. w is the distributed load and the curvature of the circular arch is $1/R$ over the whole domain where R is the radius of the circular arch. As the radius of the circular arch changes, the center angle of the circular arch also changes for preserving the original volume.

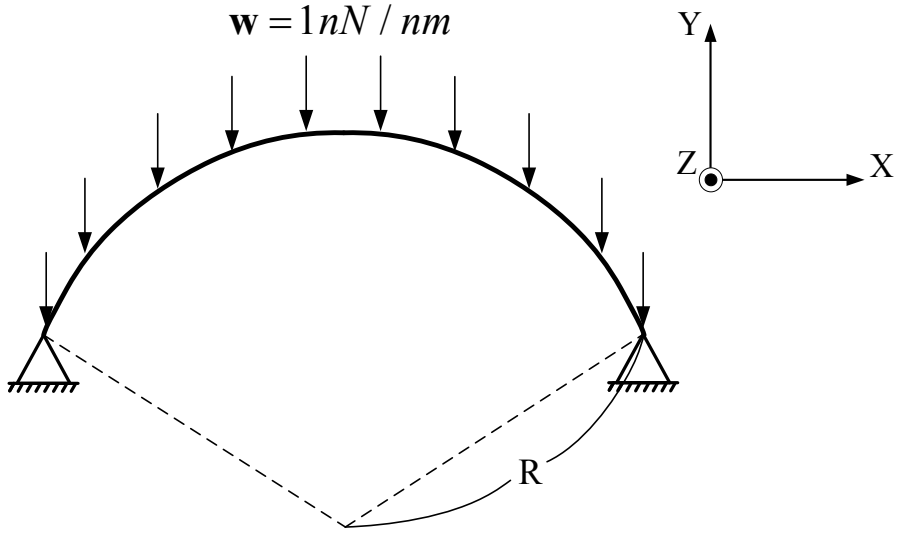

Figure 4.22 Model description of circular arch under distributed load

Surface elasticity

The exact solution of strain energy considering surface effects is derived as

$$U = U_m + U_b + U_s = \int_0^l \frac{N^2}{2\left(EA + 4\mu_0 + 2\lambda_0\right)} ds + \int_0^l \frac{M^2}{2EI + h^2\left(2\mu_0 + \lambda_0\right)} ds + \int_0^l \frac{V^2}{2\left(GA_t + \mu_0\right)} ds \quad (4.21)$$

Detailed derivation of exact solution and its derivatives are given in

appendix A. Residual surface stress τ_0 and surface Lame constants μ_0 and λ_0 are introduced to consider surface effects. Surface bending stiffness parameter d_s is not considered here. τ_0 affects the stress state directly through the axial force N, and μ_0 and λ_0 affect the constitutive relation. Optimal curvature is determined by the stationary point of strain energy given in equation (4.21). Optimal curvature minimizing strain energy is obtained under the following conditions. We determined material properties of graphene from the Farajpour's assumption (2013). Young's modulus E=1000 GPa and surface Lame constants μ_0 is 15.3846 and λ_0 is 23.0769 and residual surface stress τ_0 is 0.4. To guarantee constant state throughout the z-direction, Poisson's ratio is set to zero and unit width is assumed. The thickness is 3.35 nm and distributed load w is 3E-3 N/nm. Figure 4.23-(a) shows the variation of membrane and bending energy as function of the curvature, respectively. It is observed that optimal curvature minimizing strain energy is determined by the ratio between membrane and bending energy. Since the consideration of μ_0 and λ_0 changes constitutive relation, it changes the ratio between membrane and bending energy. Figure 4.23-(b) shows the effect of surface stress on the strain energy with curvature. If surface effects are not considered, strain energy is minimized when curvature is 1.745E-3. If μ_0 and λ_0 are considered, strain energy is minimum when curvature is 1.762E-3. If μ_0, λ_0 and τ_0 are considered, strain energy is minimum when curvature is 1.887E-3. Compared with parabolic arch example, not only τ_0 but also μ_0 and λ_0 affect the optimization results. Also, the dependence on the curvature of mechanical behaviors of curved shell in nanoscale can be observed. Even the total volume and distributed load remain constant during the curvature changes, total strain energy of the shell model changes abruptly. Therefore, representation of exact geometry is

highly significant in continuum shell modeling.

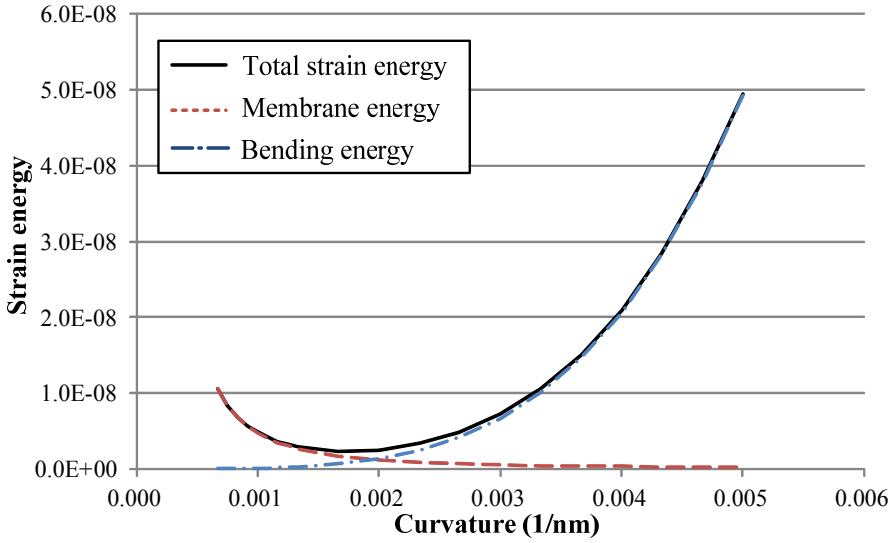

(a) Membrane and bending energy variation

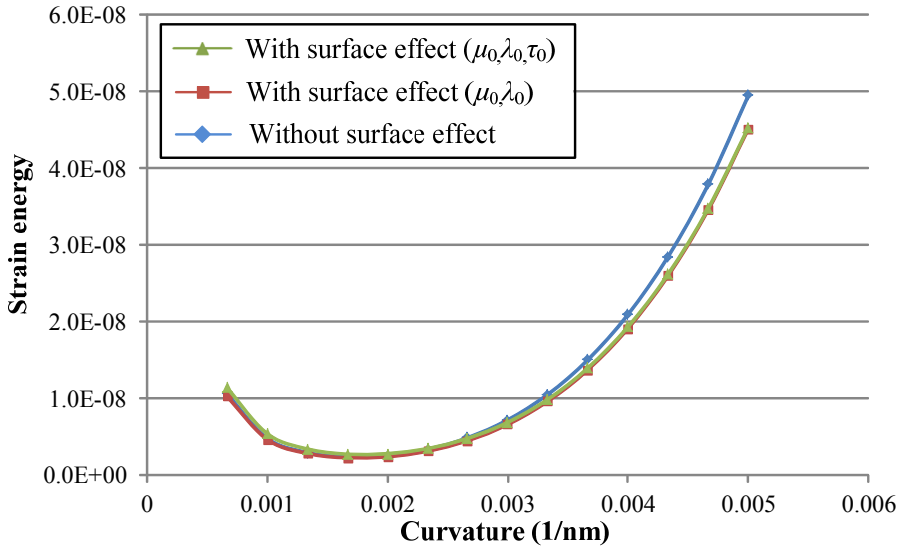

(b) Effect of the surface stress

Figure 4.23 The graph of the strain energy as function of the curvature

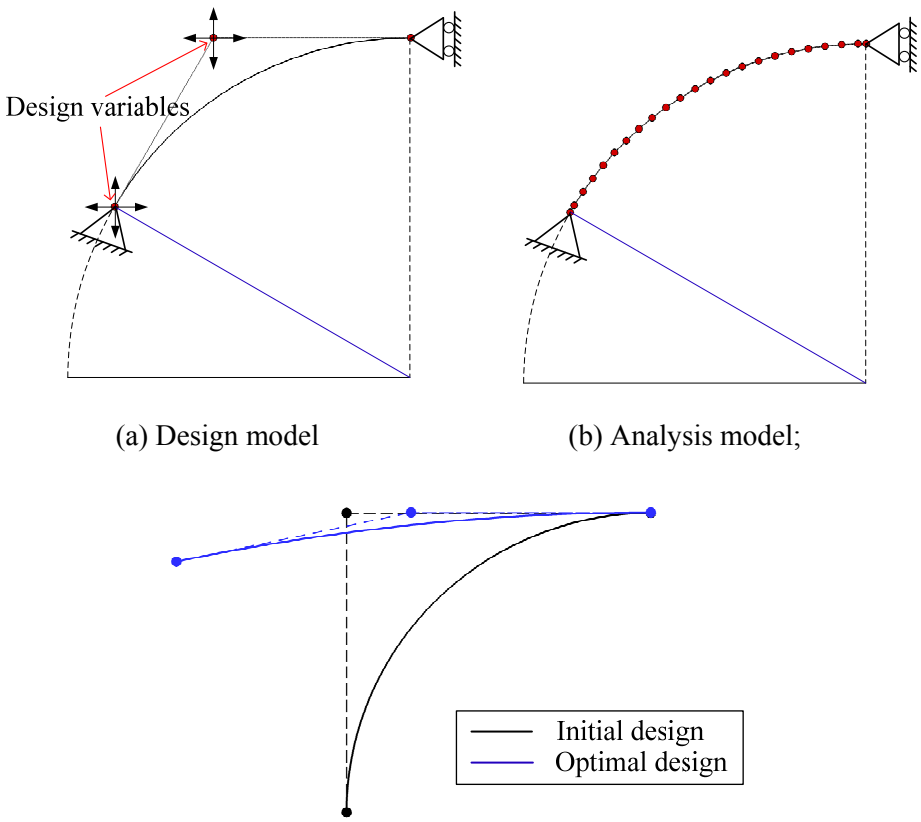

(a) Design model (b) Analysis model;

(c) Initial and optimal design

Figure 4.24 Shape design optimization of circular arch considering surface effects

Figure 4.24-(a) shows the design model and design variables for the change of curvature. Analysis model in figure 4.24-(b) is obtained through *h*-refinement of the design model keeping the geometry unchanged. Quadratic IGA is used and total number of DOFs used for analysis is 115. Thickness is 0.335 nm and distributed load w is 0.01 N/nm. Figure 4.24-(c) shows initial and optimal design. The optimal curvature is obtained as 0.087 through 3 iterations. This value is identical with exact optimal curvature considering surface effects.

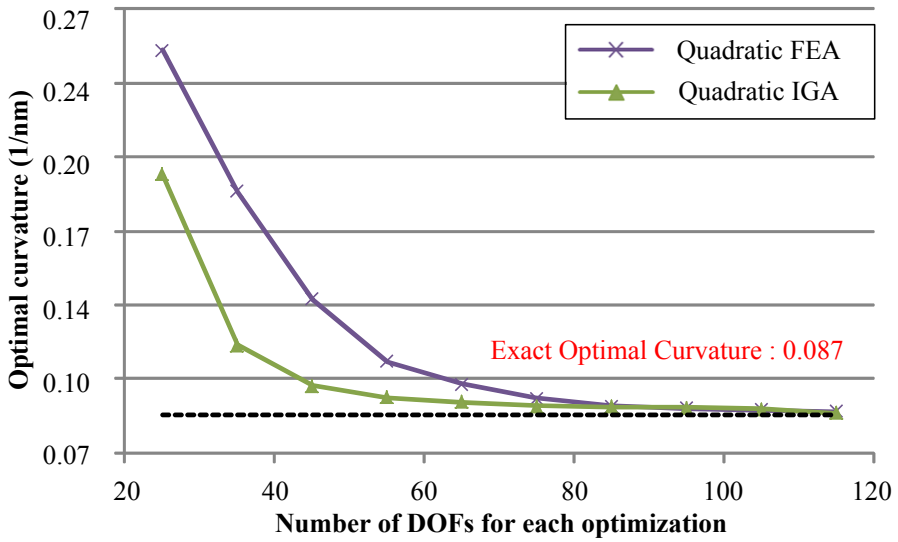

Figure 4.25 Convergence of optimal curvature of circular arch considering surface effects

Figure 4.25 shows the convergence of optimal curvature for FEA and IGA case as the number of DOFs for each optimization increases. Both cases converge well to the exact optimal curvature, and IGA case shows better convergence rate than FEA case due to the exact geometry and higher-order geometric information in DSA.

Nonlocal elasticity

The exact solution of strain energy considering nonlocal effects is derived as

$$U = U_m + U_b + U_s = \int_0^l \frac{N^2}{2EA} ds + \int_0^l \frac{M^2}{2EI} ds + \int_0^l \frac{V^2}{2GA_t} ds \qquad (4.22)$$

Detailed derivation of exact solution and its derivatives are given in appendix B. Optimal curvature is determined by the stationary point of strain energy given in equation (4.22). Optimal curvature minimizing strain energy is obtained under the following conditions. For the verification of numerical

analysis results, numerical strain energy and its shape design sensitivity are compared with the exact solutions. The problem parameters are: R is 20 nm, w is 1 nN/nm and thickness is 0.34 nm. Young's modulus E is 790.7 GPa and nonlocal parameter is 1.0 nm. To guarantee constant state throughout the z-direction, Poisson's ratio is set to zero and unit width is assumed. Total number of DOFs is 285. The exact strain energy and the numerical strain energy using quadratic FEA and IGA are compared with exact strain energy as shown in table 4.8 The IGA gives more accurate results than the conventional FEA, even same DOFs is used.

Table 4.8

Comparison of strain energy of circular arch under distributed load considering nonlocal effects

	(a) Exact strain energy	(b) Numerical strain energy	Ratio (b)/(a)
Quadratic FEA	5.818E-24	5.301E-24	91.11 (%)
Quadratic IGA		5.719E-24	98.29 (%)

The exact shape design sensitivity is obtained by differentiating equation (4.22) with respect to the curvature, and the analytical sensitivity using quadratic FEA and IGA are compared with exact shape design sensitivity as shown in table 4.9. Comparing with the exact sensitivity, analytical sensitivity of IGA shows better agreement than FEA case.

Table 4.9

Comparison of shape design sensitivity of strain energy with respect to the curvature of circular arch under distributed load considering nonlocal effects

	(a) Exact shape sensitivity	(b) Numerical shape sensitivity	Ratio (b)/(a)
Quadratic FEA	-1.162E-24	-1.021E-24	87.85 (%)
Quadratic IGA		-1.128E-24	97.01 (%)

Figure 4.26 shows the increase of nonlocal effects with the size changes. As the radius of the circle increases, the difference of the normalized strain energy between without and with nonlocal effects decreases.

Figure 4.27-(a) shows the variation of membrane and bending energy as function of the curvature, respectively. It is observed that optimal curvature minimizing strain energy is determined by the ratio between membrane and bending energy. Consideration of nonlocal parameter changes the ratio between membrane and bending energy. Figure 4.27-(b) shows the effect of nonlocal effects on the strain energy with curvature. If nonlocal effects are not considered, strain energy is minimized when curvature is 1.75E-02. If nonlocal parameter is considered, strain energy is minimized when curvature is 1.81E-02. Also, the dependence on the curvature of mechanical behaviors of curved shell in nanoscale can be observed. Even the total volume and distributed load remain constant during the curvature changes, total strain energy of the shell model changes abruptly. Therefore, representation of exact geometry is highly significant in continuum shell modeling.

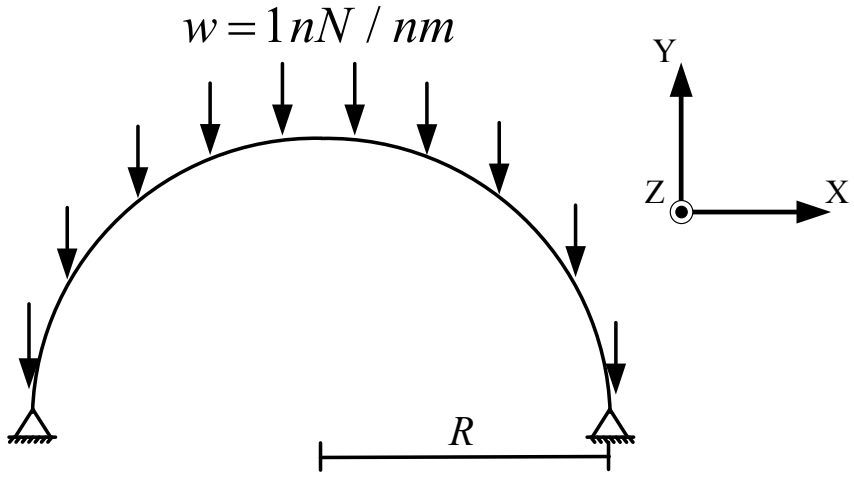

(a) Model description

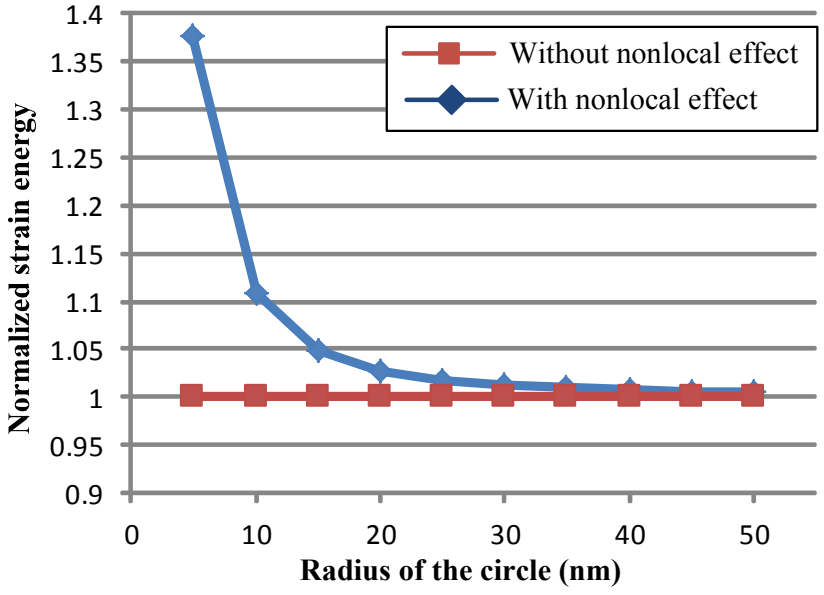

(a) Normalized strain energy as the function of radius of the circle

Figure 4.26 Nonlocal effects with the size changes

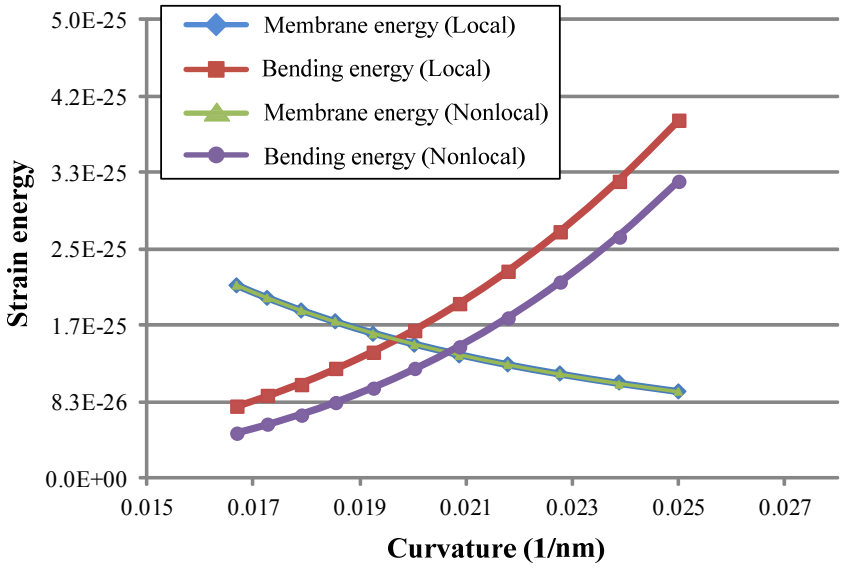

(a) Membrane and bending energy

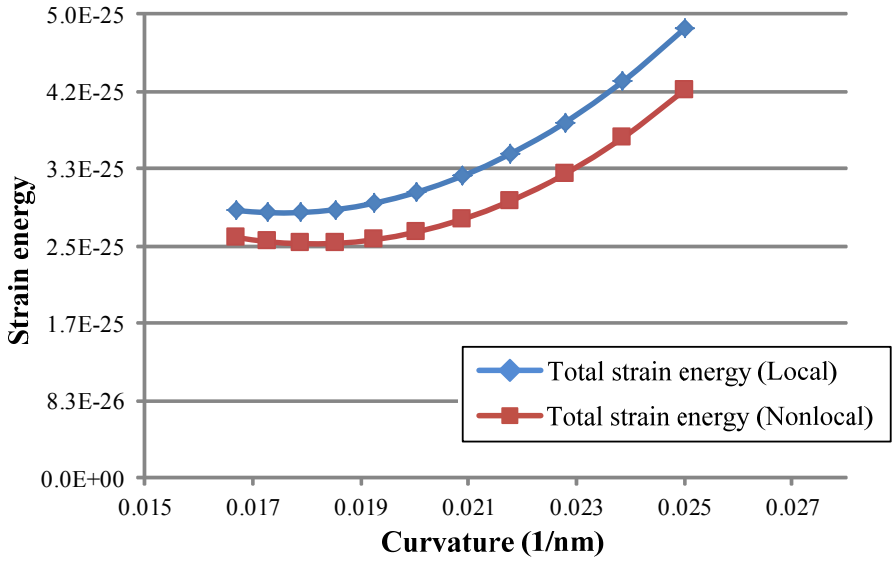

(b) Total strain energy

Figure 4.27 Variation of strain energy with curvature for a circular arch under distributed load considering nonlocal effects

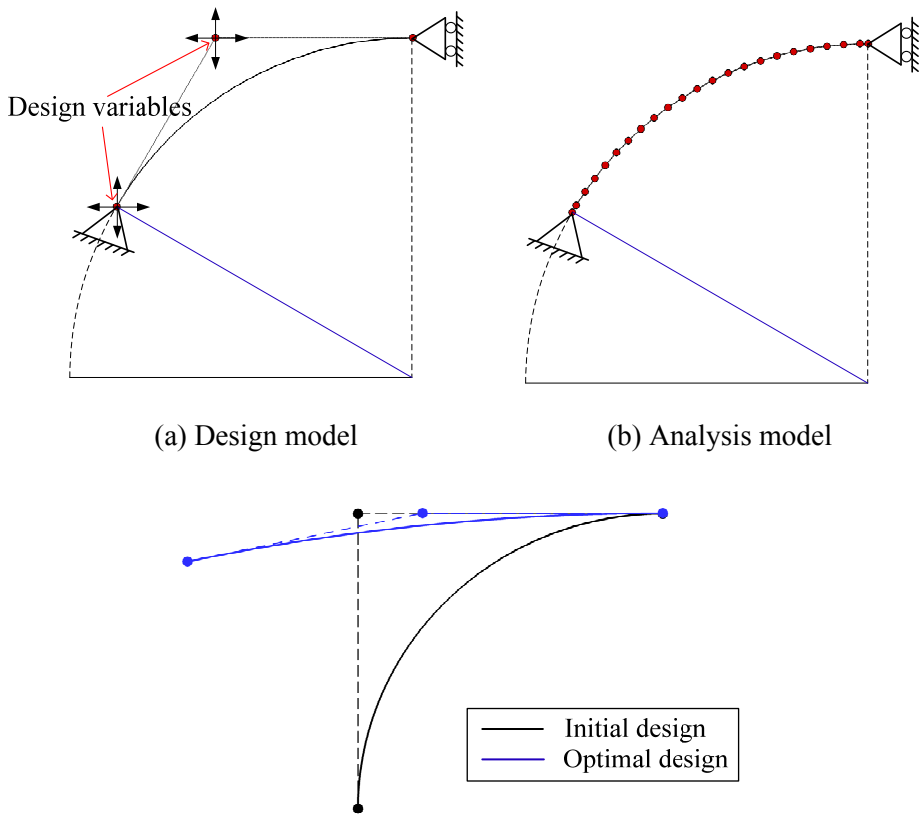

(a) Design model

(b) Analysis model

(c) Initial and optimal design

Figure 4.28 Shape design optimization of circular arch considering nonlocal effects

Figure 4.28-(a) shows the design model and design variables for the change of curvature. Analysis model in figure 4.28-(b) is obtained through h-refinement of the design model keeping the geometry unchanged. Quadratic IGA is used and total number of DOFs used for analysis is 115. Thickness is 0.34 nm and distributed load w is 1 nN/nm. Figure 4.28-(c) shows initial and optimal design and the optimal curvature is obtained as 0.018 (1/nm) through 3 iteration. This value is identical with exact optimal curvature considering nonlocal effects.

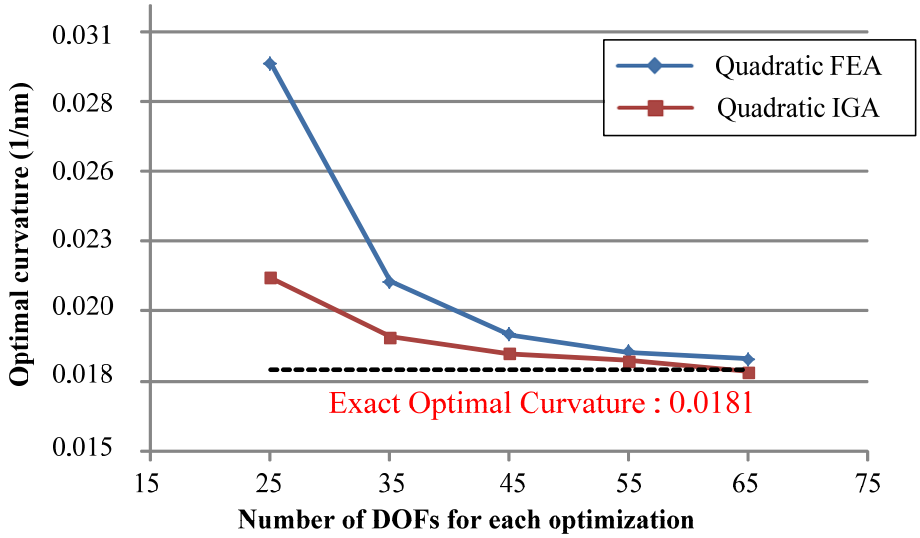

Figure 4.29 Convergence of optimal curvature of circular arch considering nonlocal effects

Figure 4.29 shows the convergence of optimal curvature for FEA and IGA case as the number of DOFs for each optimization increases. Both cases converge well to the exact optimal curvature, and IGA case shows better convergence rate than FEA case due to the exact geometry and higher-order geometric information in DSA.

Nonlocal effects are applied as the function of strain measures and contravariant component of the force given in equation (2.71). Strain measures are the function of geometric quantities such as curvature and christoffel symbol. Also, contravariant component of the forces and its derivatives are also geometric quantities if we consider design dependent load. Therefore, nonlocal effects are applied exactly by using IGA which is geometrically exact.

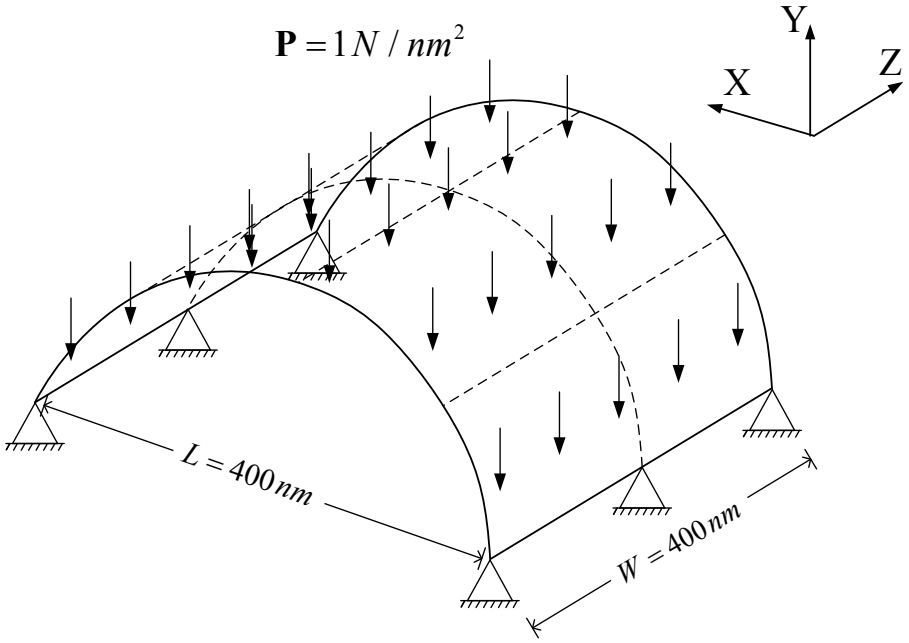

Figure 4.30 Model description of circular shell under distributed load

Circular shell example with distributed vertical load is considered as shown in figure 4.30. *L* is 400 nm, W is 400 nm, **P** is 1 N/nm^2 and μ is 10 nm. The convergence rate of terms dependent on nonlocal parameter using quadratic IGA and FEA is compared. Load linear form dependent on nonlocal parameter is written as

$$F_\mu = \mu\int_\Omega \left(f^\alpha_{,\beta}\varepsilon_{\alpha\beta}(\bar{\mathbf{z}}) + f^n\omega_{\alpha\alpha}(\bar{\mathbf{z}}) + f^n_{,\alpha}\gamma_\alpha(\bar{\mathbf{z}}) \right)\sqrt{a}d\Omega \tag{4.23}$$

Also, explicitly dependent part of shape design sensitivity dependent on nonlocal parameter is written as

$$F'_{\mu(V)}(\bar{\mathbf{z}}) = \int_\Omega \left[\left\{ \mu\left(f^\alpha_{,\beta}\varepsilon_{\alpha\beta}(\bar{\mathbf{z}}) + f^n\omega_{\alpha\alpha}(\bar{\mathbf{z}}) + f^n_{,\alpha}\gamma_\alpha(\bar{\mathbf{z}}) \right) \right\} \left(\sqrt{a}\right)^{\cdot} \right] hd\Omega$$

$$+\int_\Omega \left[\mu\left(\dot{f}^\alpha_{,\beta}\varepsilon_{\alpha\beta}(\bar{\mathbf{z}}) + \dot{f}^n\omega_{\alpha\alpha}(\bar{\mathbf{z}}) + \dot{f}^n_{,\alpha}\gamma_\alpha(\bar{\mathbf{z}}) \right)\left(\sqrt{a}\right) \right] hd\Omega$$

$$+\int_\Omega \left[\mu\left(f^\alpha_{,\beta}\left(-\dot{\Gamma}^\mu_{\alpha\beta}\bar{u}_\mu - \dot{b}_{\alpha\beta}\bar{w} \right) + f^n\left(-\dot{\Gamma}^\mu_{\alpha\alpha}\bar{\psi}_\mu \right) \right)\left(\sqrt{a}\right) \right] hd\Omega$$

$$+\int_{\Omega}\left[\mu\left(f^{n}_{,\alpha}\left(\dot{b}^{\lambda}_{\alpha}\bar{u}_{\lambda}\right)\right)\left(\sqrt{a}\right)\right]hd\Omega \tag{4.24}$$

Equations (4.23) and (4.24) are computed for the unit $\bar{\mathbf{z}}$ and normalized force and moment components are plotted in figure 4.31. Strain measures and contravariant component of the forces are function of geometrical quantities such as covariant basis, curvature and christoffel symbol. IGA is geometrically exact and represent these quantities exactly even small number of DOFs. However, quadratic FEA is not geometrically exact and these quantities cannot be represented exactly. Also, geometrical error is increased when calculating the first order derivatives of these quantities.

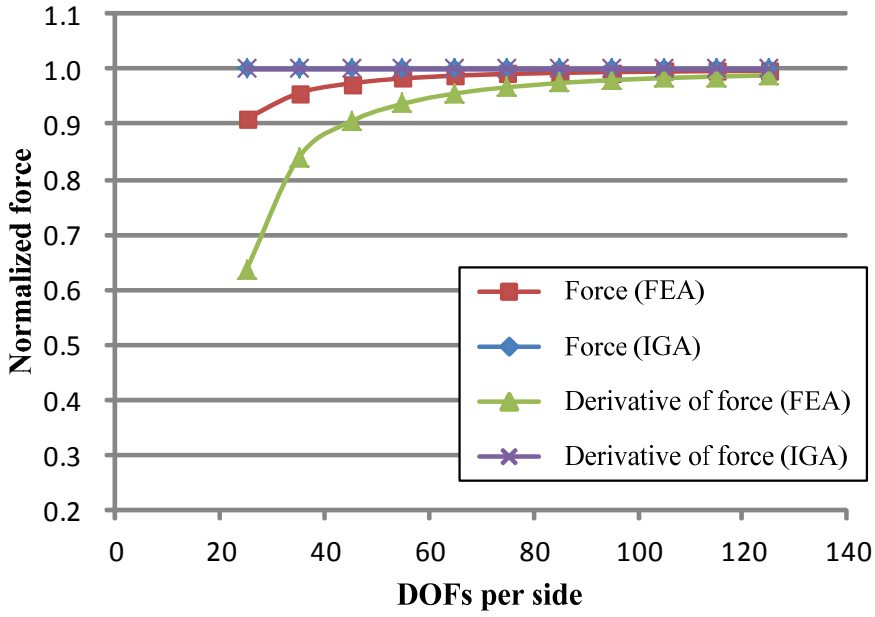

(a) Normalized force

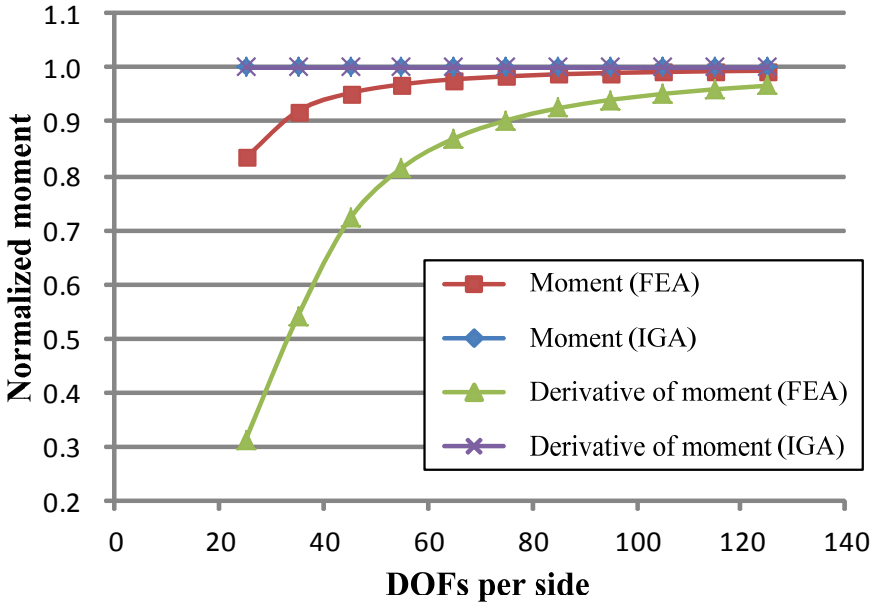

(b) Normalized moment

Figure 4.31 Convergence rate of nonlocal parameter terms

4.2.3 Shape design optimization of silver shell: optimal form

This example is suggested to illustrate the capabilities of developed method under general shell components as shown in figure 4.32-(a). The objective of this optimization problem is to minimize the strain energy under the distributed load. Design variables are specific coordinates of control points as shown in figure 4.32-(b), and 1445 DOFs are used for analysis through *h*-refinement scheme as shown in figure 4.32-(c). The length L of initial geometry is 1.0 μm and thickness h is 40 nm. The distributed load is set to 0.5 MN/m^2, and four corners are simply supported. The material is assumed as silver which is same with the example suggested in chapter 4.1. Young's modulus E is 76 GPa, Poisson's ratio v is 0.37, surface modulus E_s is 1.22 N/m, residual surface stress τ_0 is 0.89 and surface bending stiffness parameter d_s is 3.2 (1E-14Nm). Figure 4.33 shows the optimization history with and without surface effects. Figure 4.34 shows the optimization history of membrane and bending energy, respectively. When the shape of the shell if flat, the bending energy is dominant. As the curvature changes during the optimization process, membrane-oriented design is presented avoiding as far as possible bending energy to minimize total strain energy. Even at initial design with surface effects, membrane energy is caused by residual surface stress τ_0. During the optimization process, bending energy is decreased by curvature change but the membrane energy caused by τ_0 cannot be totally decreased by curvature change. Therefore, total strain energy with τ_0 mainly due to the membrane energy is higher than without τ_0. For the high-order surface effect, the structure behaves stiffer and total strain energy is decreased.

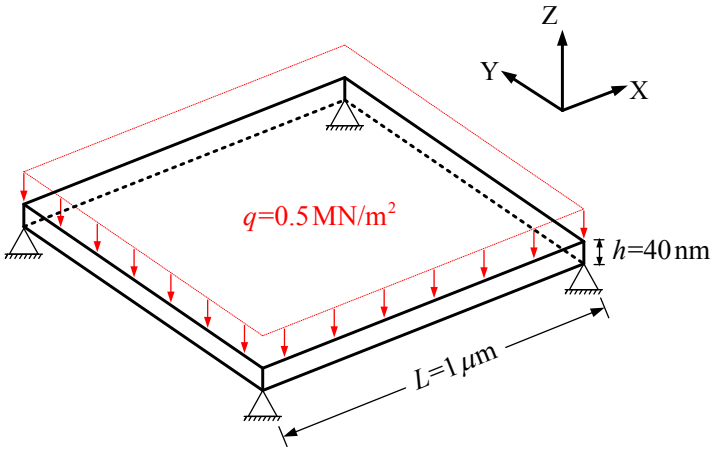

(a) Model description

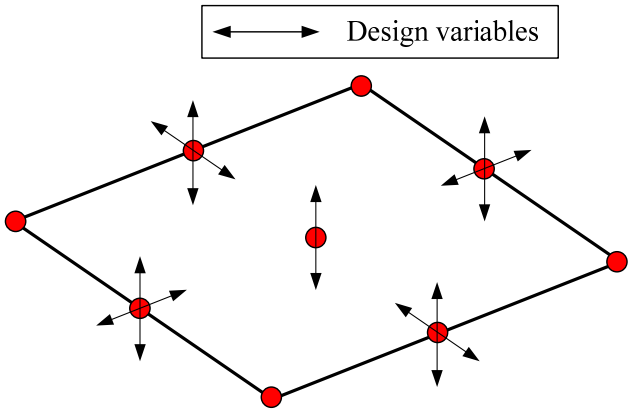

(b) Design model

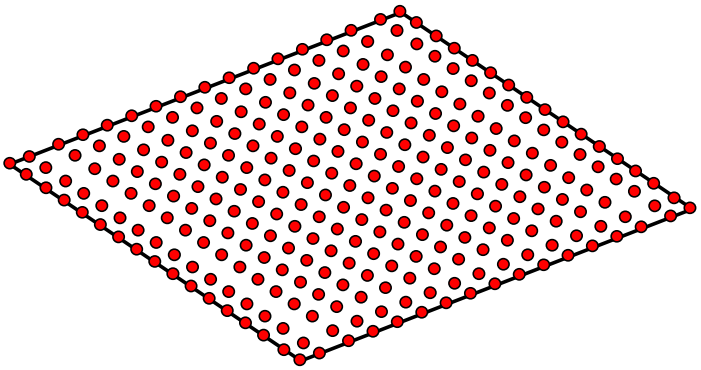

(c) Analysis model

Figure 4.32 Model description of optimal shell form

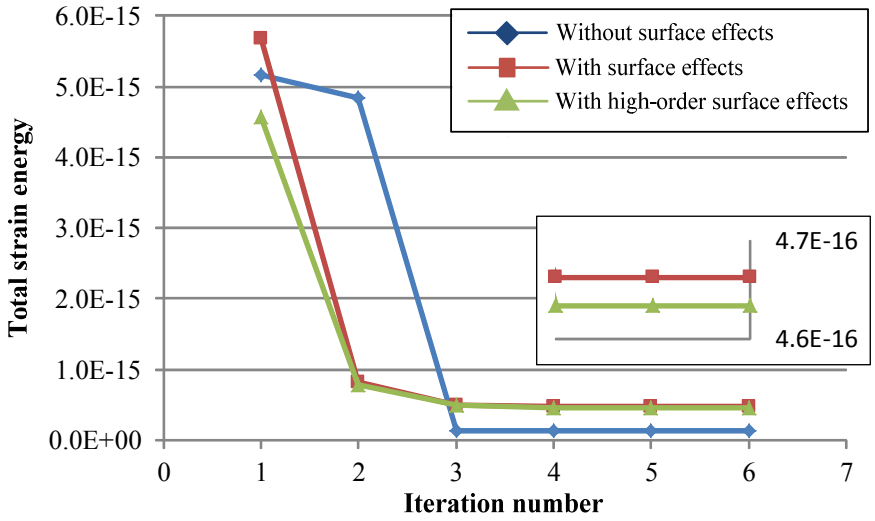

Figure 4.33 Optimization history of optimal shell form problem

Figure 4.35 shows the effect of the surface stress on the optimal shape. Similar dome shape is obtained to minimize bending energy, but maximum heights of the dome are different at each case. Maximum height of the optimal shape is 435.3 nm for the case without surface effects, and it is 298.5 nm for the case with surface effects. The effect of E_s is ignorable in this example and that of τ_0 is required to be observed carefully. Since minimizing the area is more advantageous than generating curvature to minimize membrane energy caused by residual surface stress τ_0, maximum height of optimal shape is decreased. Maximum height of the optimal shape is decreased to 294.3 nm for the case with high-order surface effects. This is because bending energy over membrane energy decreases by considering high-order surface effects. In figure 4.36, different distributed load is assumed to show the dependence on the distributed load in the optimal shape. When the distributed load is dominant compared with residual surface stress, optimal shape is almost same with that of case without surface effects. On the other hand, when the residual surface stress is dominant with relatively

small distributed load, maximum height of optimal shape is almost zero, and it has small curvature on the surface.

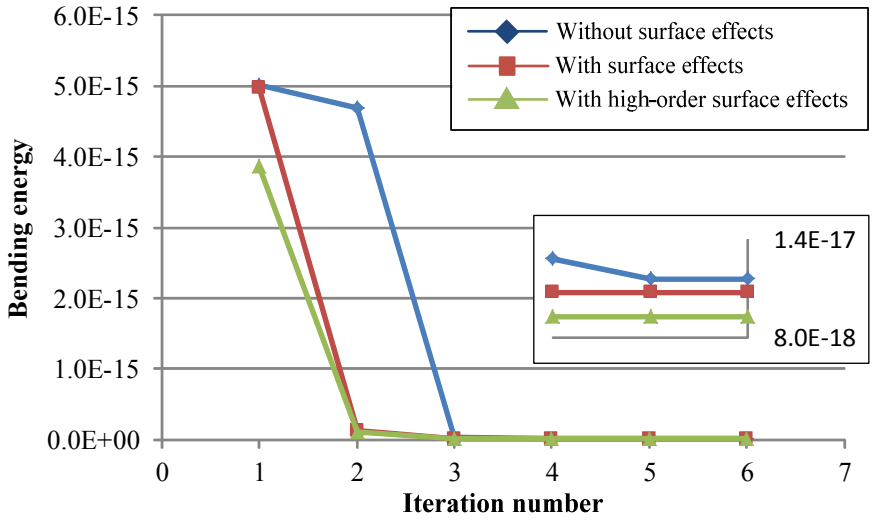

(a) Bending energy

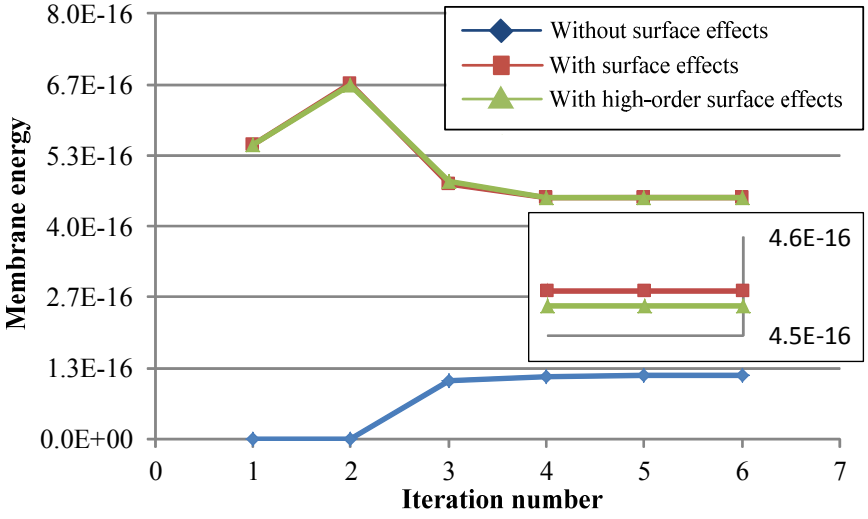

(b) Membrane energy

Figure 4.34 Optimization histories of membrane and bending energy

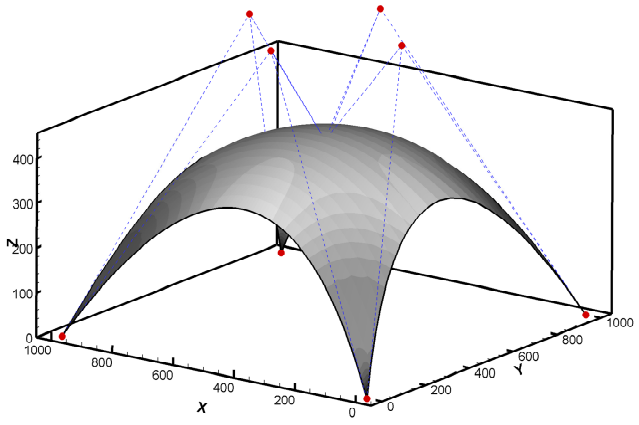

(a) Without surface effects

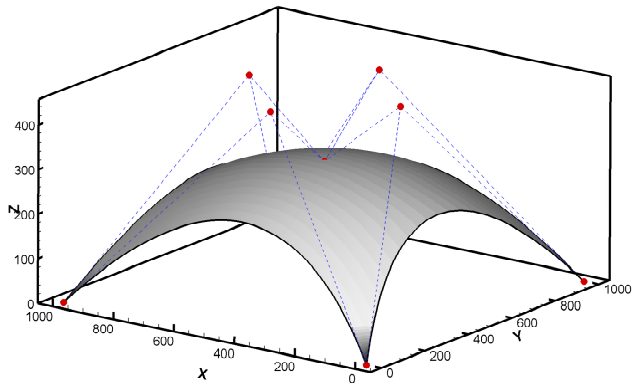

(b) With surface effects

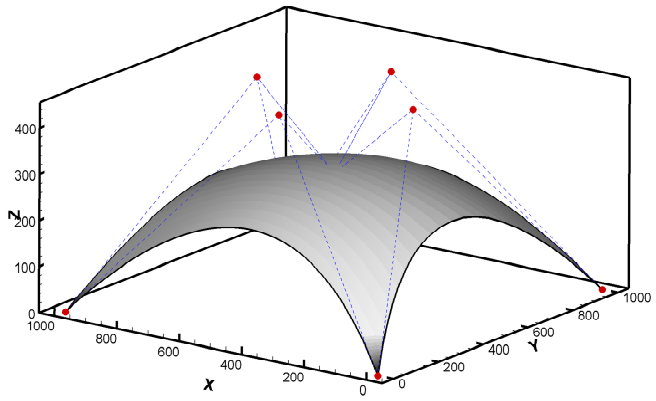

(c) With high-order surface effects

Figure 4.35 Effect of the surface stress on the optimal shape

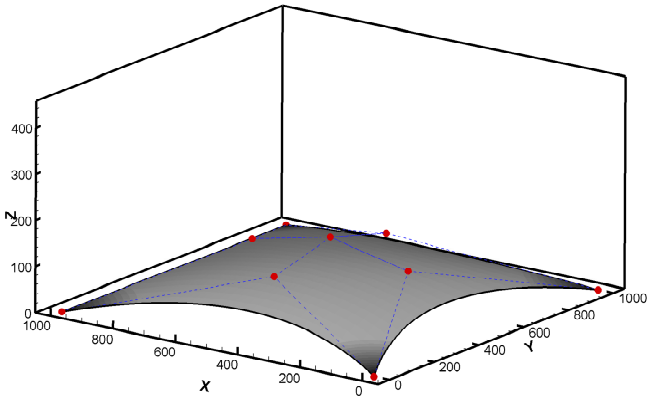

(a) q=0.1 MN/m^2

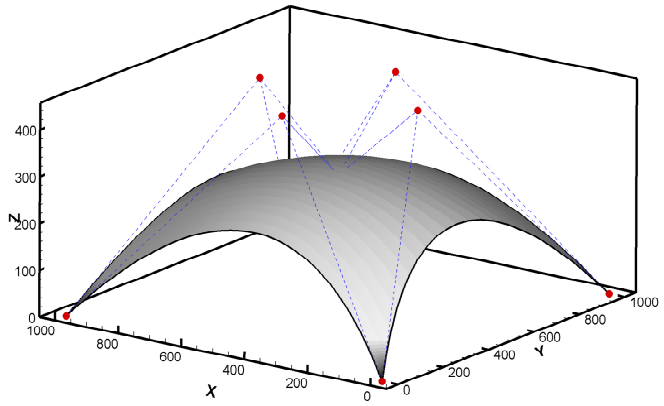

(b) q=0.5 MN/m^2

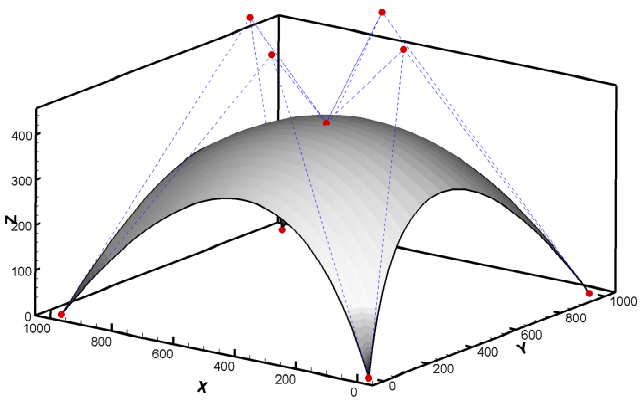

(c) q=1.0 MN/m^2

Figure 4.36 Effect of distributed load on the optimal shape

4.2.4 Crack problem of graphene: exact stress distribution without singularity

Since the behavior of crack initiation and its growing process are very crucial for the safety of ship and marine structures, obtaining exact mechanical behavior of structures with crack is important. As the size of the crack decreases to micro or nanoscale, we cannot obtain exact computation results using linear elastic fracture mechanics (LEFM). If we observe crack tip in nanoscale, it is represented as smooth boundary and it has finite stress value. However, stress computation based on LEFM contains singularity at the crack tip, which does not indicate physical nature. This led researchers to develop several fracture criteria such as *J*-integral and stress intensity factor. However, contrary to the LEFM, it is found that no stress singularity is present at the crack tip in nonlocal theory. Therefore, measuring maximum stress can be used as a natural fracture criterion in nonlocal theory. Validation of nonlocal theory using MD simulation is performed. We also analyze the structures with crack in nanoscale using nonlocal theory and maximum stress is observed using FEA and IGA.

Validation of nonlocal theory using MD simulation

In this chapter, molecular dynamics simulation is performed on the 2D graphene systems containing atomic-scale cracks using LAMMPS (Sandia National Laboratories 2009) molecular dynamics simulator. Graphene is a one-atom-thick planar sheet of carbon atoms, densely packed together into a honeycomb shaped crystal lattice. The associated atomistic interaction is covalently bonded by SP^2 hybridized electrons, and the bond angle is $2\pi/3$. (Cho et al. 2007) The interatomic distance between the adjacent atom is 1.42

Å . The total potential of the graphene sheet considering bond stretching and bond angle bending can be written as

$$U = \sum \frac{1}{2} k_r \left(r - r_0 \right)^2 + \sum \frac{1}{2} k_\theta \left(\theta - \theta_0 \right)^2 \tag{4.25}$$

where k_r and k_θ are the bond stretching force constant and angle bending force constant which are selected from AMBER force field for carbon-carbon atomic-interaction. (Cornell et al. 1995) k_r is 938(kcal/mol-Å^2) and k_θ is 126(kcal/mol-rad^2). Figure 4.37 shows the dimension of the graphene sheet with a crack. The center crack is modeled by eliminating the associated covalent bond. The crack length is 10.086 nm which is 41 lattices and total length of the domain is 10 times of the crack length. Initial state without applied deformation reaches equilibrium for approximately 100 ps with a time step of 1.5 fs. After equilibrium is reached, we perform uniaxial tension by applying a deformation. u_y=0.005y is prescribed on upper and lower surfaces. After another 100 ps, minimum potential energy of the system is obtained. Molecular mechanics simulation is carried out at a temperature of 0 K. For more detailed procedure of molecular mechanics simulation, interested readers may refer to Tsai et al. (2010) or Jin and Yuan (2005a).

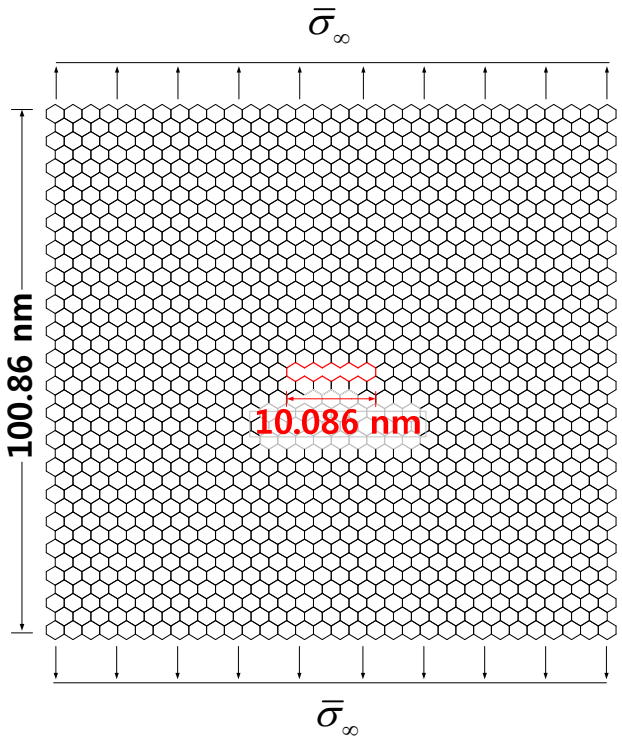

Figure 4.37 Model description of the graphene sheet with a center crack

The atomic stress is obtained from the virial theorem which gives the stress value as the function of atom coordinates and interatomic forces. Virial stress is given as

$$\sigma_i^{\alpha\beta} = \frac{1}{2V_0}\sum_{j\neq i} r_{ij}^{\alpha} f_{ij}^{\beta} \tag{4.26}$$

where $\sigma_i^{\alpha\beta}$ is atomic stress at atom i, r_{ij}^{α} is the distance between atom i and j projected in an α direction, f_{ij}^{β} is the β-component of the interatomic force exerted on atom i by atom j. V_0 is volume per atom. Figure 4.38 shows the plot of normalized virial stress of σ^{yy}/σ_0, where σ_0 is the distributed stress on the upper and lower surfaces by applying a deformation. Stress is concentrated on the crack tip and it converges to 1.0 as the distance from the crack tip increases.

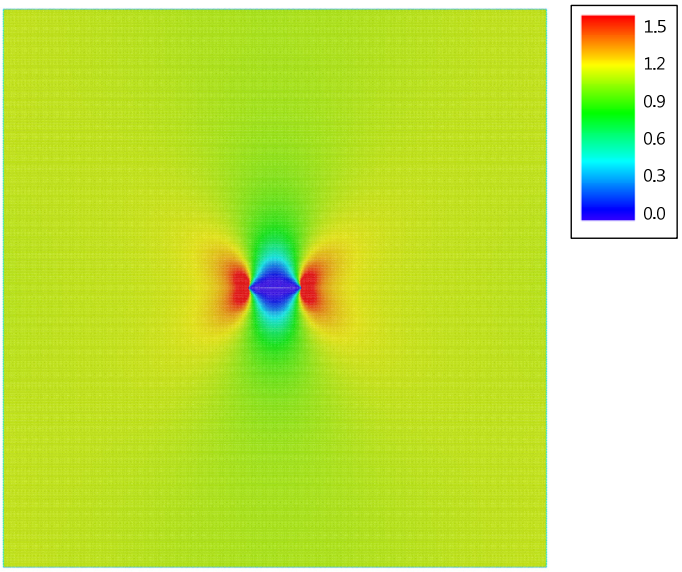

Figure 4.38 The plot of normalized virial stress value

Figure 4.39-(a) shows atomic stress plot near the crack tip. For some interested atoms in front of the crack tip, virial stress is calculated and compared with continuum stress. Figure 4.39-(b) shows the distribution of normalized virial stress in front of a crack with the comparison of continuum stress from a LEFM solution and nonlocal stress. In the nonlocal stress computation, nonlocal parameter for graphene sheets is given as 0.095 nm. (Tsai and Sie 2015) At the crack tip, stress obtained from MD simulation shows more reasonable description than the stress singularity obtained by LEFM. Also, nonlocal stress shows no crack tip singularity and the stress value is comparable with discrete virial stress.

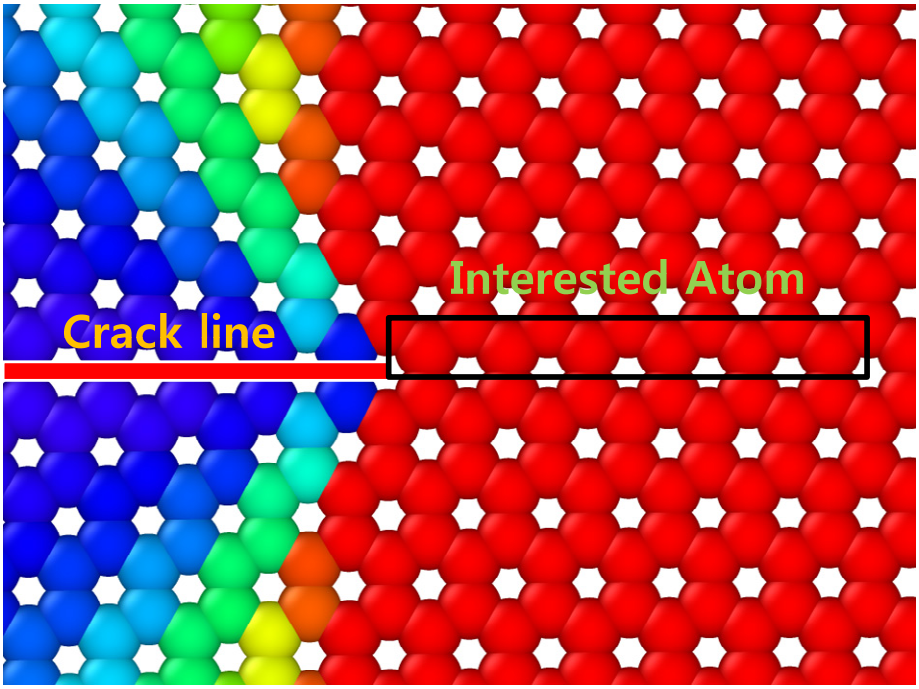

(a) Interested atom around a crack line

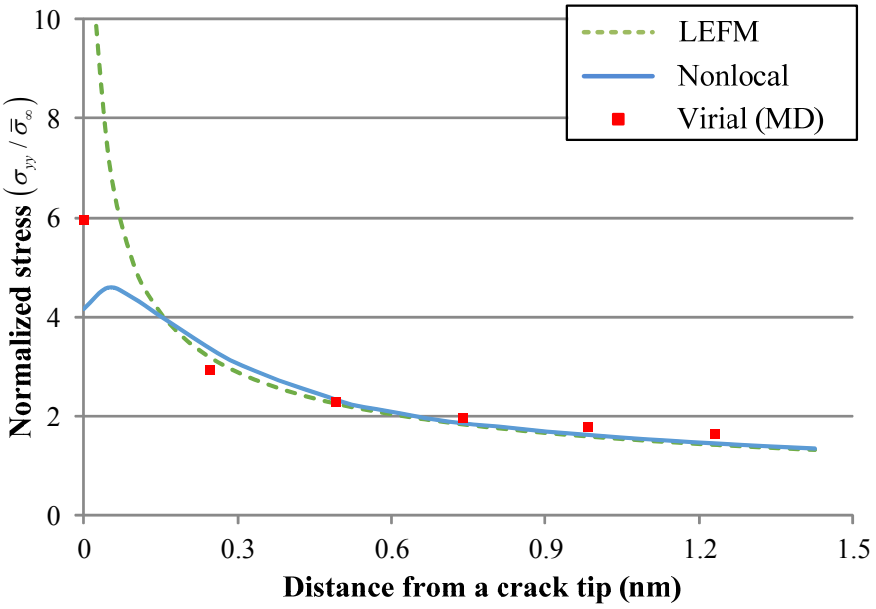

(b) Comparison of normailized stress

Figure 4.39 Distribution of the stress near the crack line

Infinite plate with a center crack

We consider infinite plate with a center crack under remote tension as shown in figure 4.40-(a). Only a quarter of the model needs to be considered due to the symmetry as shown in figure 4.40-(b). Local refinement is required due to abrupt change of the solution near the crack tip as shown in figure 4.40-(c). The crack length a is 5 nm and the length L of the plate is 100 nm for the infinite plate assumption. Discontinuity of crack geometry is represented simply by using the quarter model. For the lower edges containing crack geometry in figure 4.40-(b), boundary condition is not applied for the regions with crack but fixed boundary condition is applied for the regions without crack. For locating the crack tip at the desired position, knot repetition is used for the NURBS basis functions to be modified to have a Kronecker delta property at the crack tip. Distributed load $\bar{\sigma}_{\infty}$ is 1 nN/nm. Young's modulus of graphene is 790.7 GPa and Poisson ratio is 0.27. Nonlocal parameter μ is 0.095 nm. (Tsai and Sie 2015) Numerical nonlocal stress values obtained from IGA and FEA with same order basis function are compared with exact nonlocal stress values to show the accuracy of IGA. The process of obtaining exact local stress value of infinite plate with a center crack under remote tension is given in Appendix C. Figure 4.41 shows nonlocal stress distribution of infinite plate near the crack tip. It shows the convergence of nonlocal stress for IGA and FEA case as the number of DOFs increases. Even basis functions with same order are used in both FEA and IGA cases, IGA shows better convergence rate than FEA case.

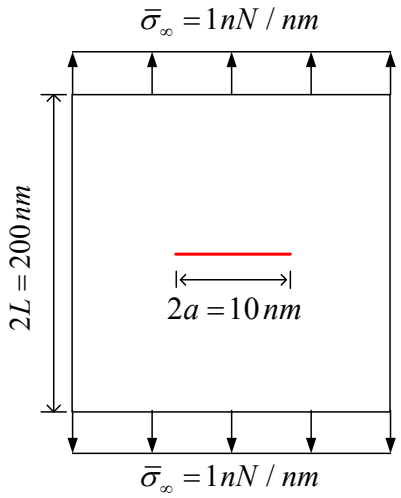

(a) Model description

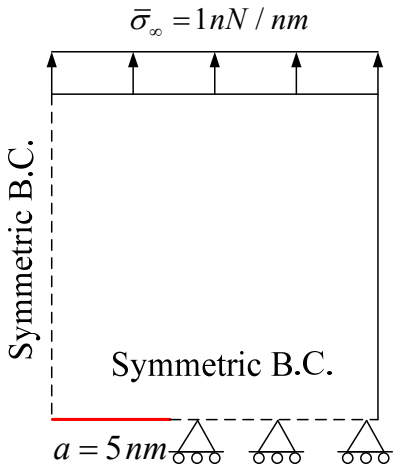

(b) Quarter model

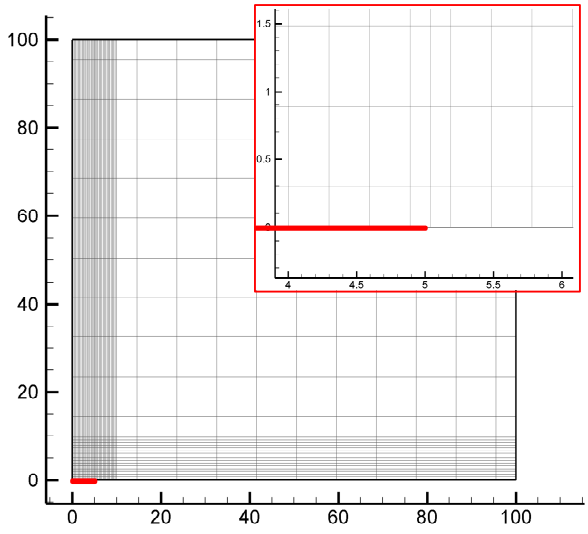

(c) Locally refined model (2726 DOFs)

Figure 4.40 Infinite plate with a center crack

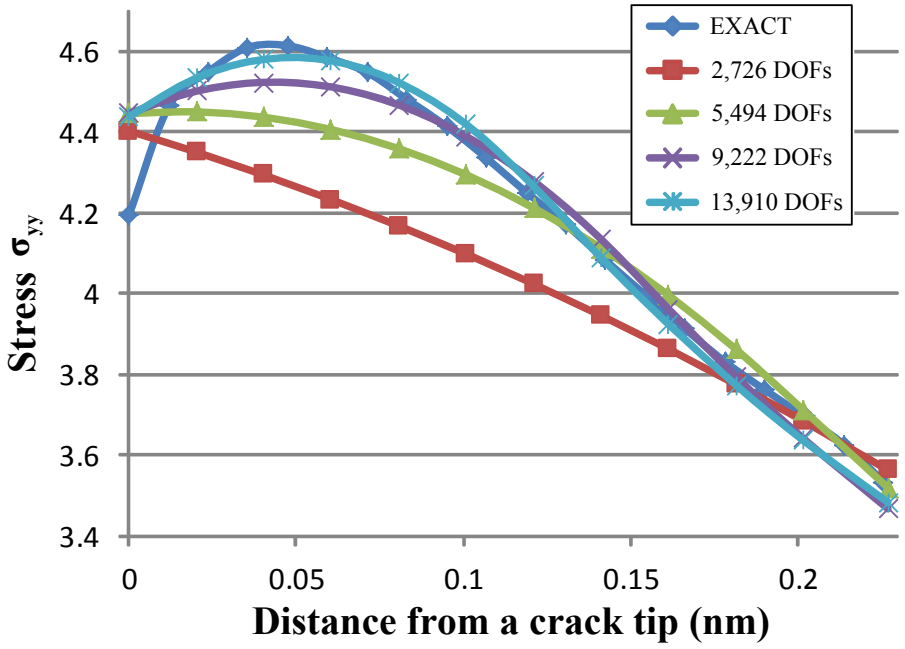

(a) Quadratic IGA

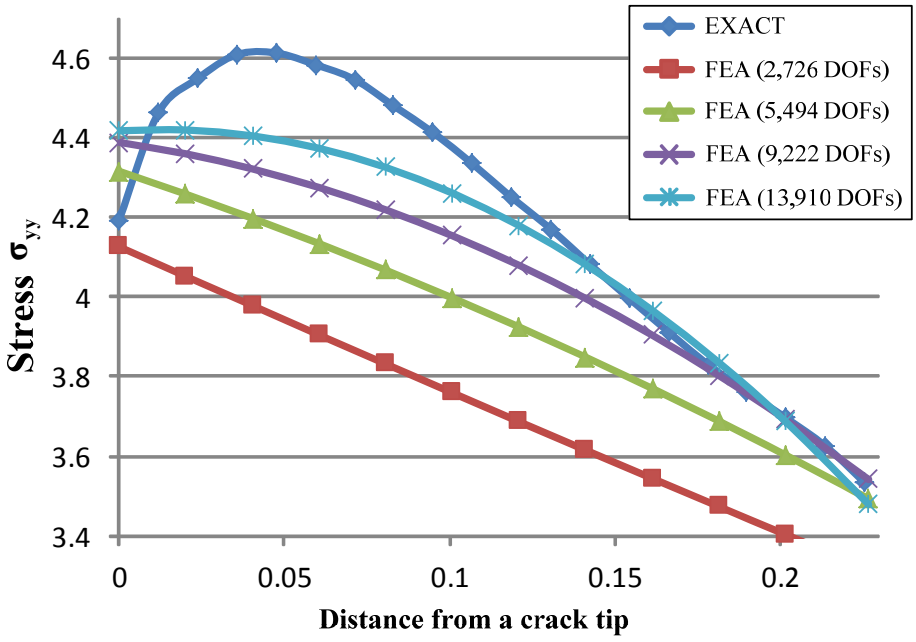

(b) Quadratic FEA

Figure 4.41 Nonlocal stress distribution near the crack tip of infinite plate

Cylindrical shell under tension loading

The next example is cylindrical shell under tension loading. The model description is shown in figure 4.42-(a). Radius R is 20 nm, thickness t is 0.5 nm, and length L is 100 nm containing a circumferential through wall crack of length 10π nm. Distributed tensile force P is 1 nN/nm. Young's modulus E is 1.0 GPa and Poisson ratio ν is 0.3. Nonlocal parameter μ is 1.0 nm. Figure 4.42-(b) shows quarter model due to the symmetry and figure 4.42-(c) shows nonlocal stress plot of σ_{yy}. Stress is concentrated on the crack tip. Numerical nonlocal stress values obtained from IGA and FEA with same order basis function are compared with converged stress values to show the accuracy of IGA. Exact solution does not exist in this example. Figure 4.43-(a) and (b) respectively show the nonlocal stress distribution near the crack tip of cylindrical shell under tension loading using quadratic IGA and quadratic FEA as total DOFs increase. The convergence rate of the IGA is superior to that of the FEA. That is because geometrical quantities such as curvature and christoffel symbol are computed exactly on the IGA framework.

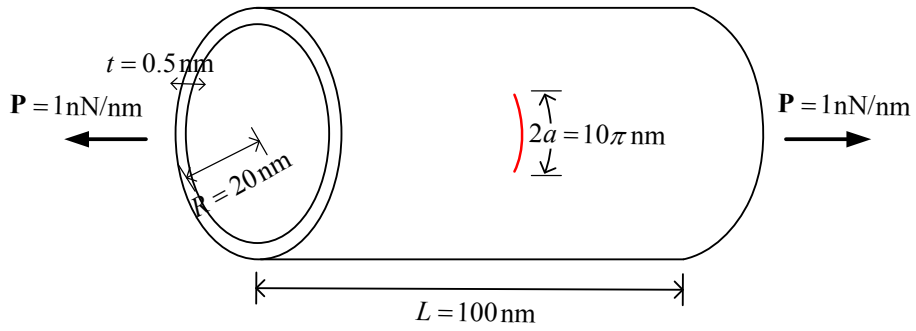

(a) Model description

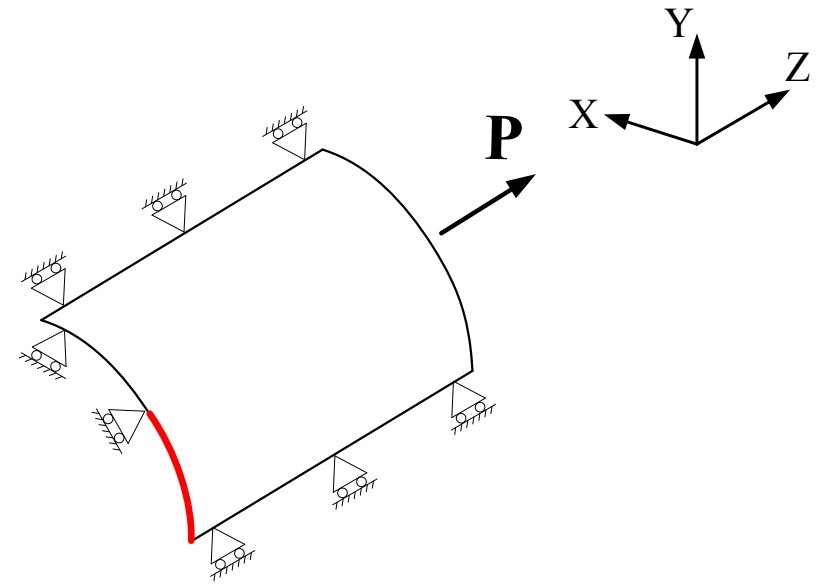

(b) Quarter model

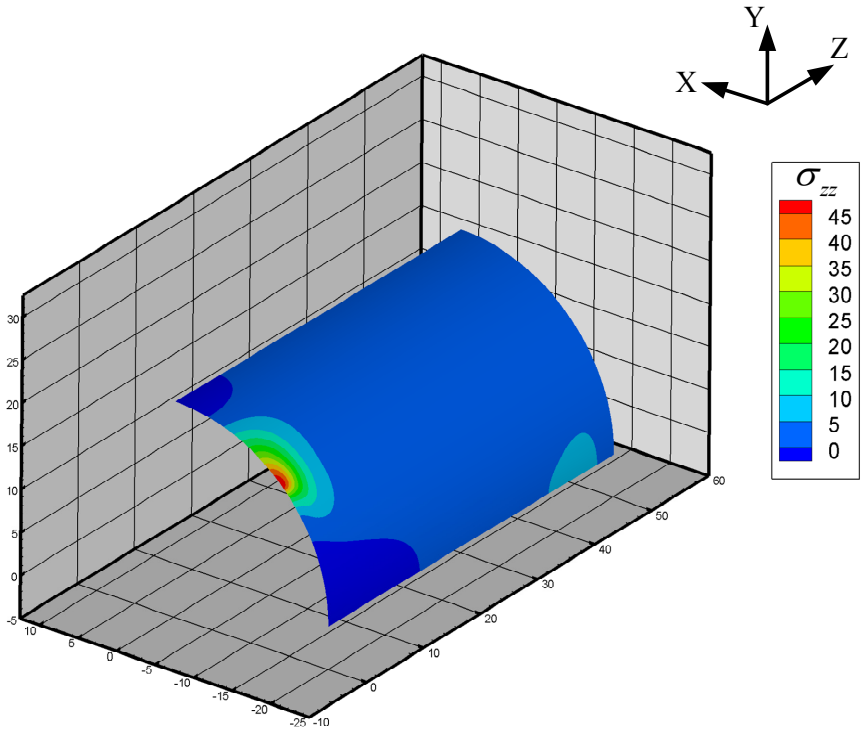

(c) Stress plot

Figure 4.42 Cylindrical shell under tension loading

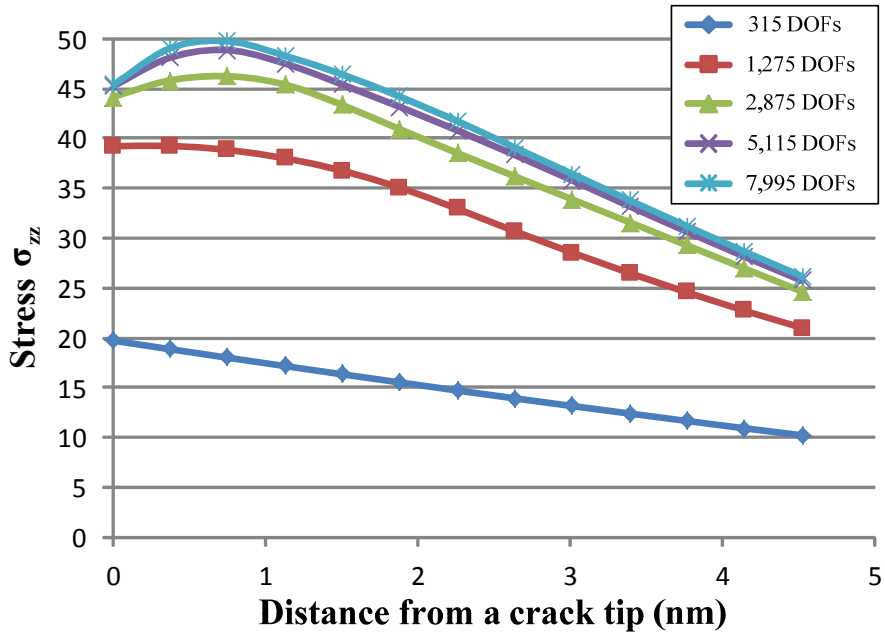

(a) Quadratic IGA

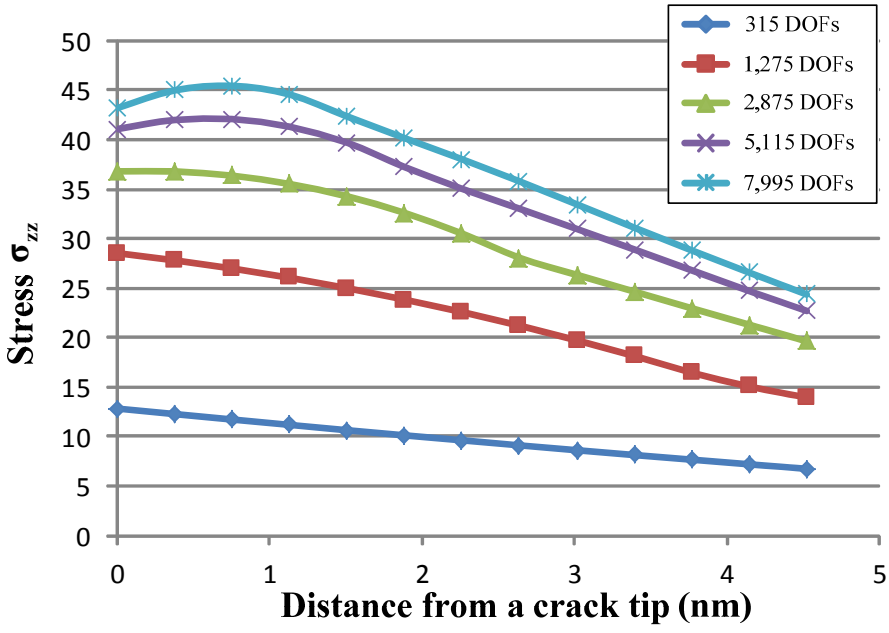

(b) Quadratic FEA

Figure 4.43 Nonlocal stress distribution near the crack tip of cylindrical shell under tension loading

Chapter 5. Conclusions and Future Works

5.1 Conclusions

In this paper, isogeometric shape design optimization method considering size effects in nanoscale structures is developed. MD simulation gives accurate results for nanoscale structures, but they are computationally expensive for systems with practical structures having relatively large sizes. Therefore, we applied continuum based model such as beam and shell for the analysis of nanoscale structures by considering size effects. Surface elasticity theory and nonlocal theory is introduced to consider size effects in nanoscale, respectively. They have different properties and should be applied properly depending on the application. We also derived the shape DSA formulation for beam and shell structures using direct differentiation method.

Through three-point bending test of silver nanowires using AFM instruments, developed continuum based model considering surface effects is validated. The behaviours of nanowires obtained from experimental results are compared with those obtained from developed method and it shows good agreement. The design sensitivity is also validated through experimental data. The design sensitivity values obtained from fitting curve of experimental data are compared with those obtained by DSA based on continuum formulation considering surface effects, and fairly good agreement is observed between them.

Several numerical examples are given to illustrate the capabilities of developed method for the shell structures. The problem obtaining optimal height of parabolic arch in nanoscale is solved by introducing surface effects. Optimal curvature of curved graphene is obtained by considering surface effects and nonlocal effects, respectively. Optimal shell form considering

surface effects and crack tip problem considering nonlocal effects are presented. We demonstrate that IGA framework shows better convergence rate than FEA case due to the exact geometry and higher-order geometric information in DSA formulation. Also, we derived exact optimal solution and showed optimal solution is affected by size effects. The new results obtained from the present research not only unveil the applicability of conventional continuum based analysis in nanoscale, but also exhibit the significance of considering size effects to obtain the proper optimal design in nanoscale devices.

5.2 Future works

In this research, design sensitivity of continuum based beam model considering surface effects is validated through experiments using AFM. However, the beam is assumed as straight one for simplicity and design sensitivity of shell structures is not validated. This is because experiments in nanoscale have limitations on manufacturing technologies and applying several boundary conditions. As the manufacturing technologies in nanoscale and experiments scheme develop, several experiments will be possible including validation of shell structures. Also, this research will be the basis for the experimental vavidation of shape design optimization in nanoscale.

It is expected that accurate prediction of mechanical behavior for nanoscale structures based on IGA can be significant research to enhance other useful properties such as electronic and electrical properties in MEMS and NEMS devices.

Bibliography

Altenbach, H., & Eremeyev, V. A. (2011). On the shell theory on the nanoscale with surface stresses. *International Journal of Engineering Science*, *49*(12), 1294-1301.

Arash, B., & Ansari, R. (2010). Evaluation of nonlocal parameter in the vibrations of single-walled carbon nanotubes with initial strain. *Physica E: Low-dimensional Systems and Nanostructures*, *42*(8), 2058-2064.

Askes, H., Morata, I., & Aifantis, E. C. (2008). Finite element analysis with staggered gradient elasticity. *Computers & Structures*, *86*(11), 1266-1279.

Askes, H., & Aifantis, E. C. (2011). Gradient elasticity in statics and dynamics: an overview of formulations, length scale identification procedures, finite element implementations and new results. *International Journal of Solids and Structures*, *48*(13), 1962-1990.

Chen, T., Chiu, M. S., & Weng, C. N. (2006). Derivation of the generalized Young-Laplace equation of curved interfaces in nanoscaled solids. *Journal of Applied Physics*, *100*(7), 074308.

Chhapadia, P., Mohammadi, P., & Sharma, P. (2011). Curvature-dependent surface energy and implications for nanostructures. *Journal of the Mechanics and Physics of Solids*, *59*(10), 2103-2115.

Chiu, M. S., & Chen, T. (2011). Effects of high-order surface stress on static bending behavior of nanowires. *Physica E: Low-dimensional Systems and Nanostructures*, *44*(3), 714-718.

Cho, S., & Ha, S. H. (2009). Isogeometric shape design optimization: exact geometry and enhanced sensitivity. *Structural and Multidisciplinary Optimization*, *38*(1), 53-70.

Cho, J., Luo, J. J., & Daniel, I. M. (2007). Mechanical characterization of

graphite/epoxy nanocomposites by multi-scale analysis. *Composites science and technology*, *67*(11), 2399-2407.

Choi, M. J., & Cho, S. (2014). Isogeometric shape design sensitivity analysis of stress intensity factors for curved crack problems. *Computer Methods in Applied Mechanics and Engineering*, *279*, 469-496.

Cornell, W. D., Cieplak, P., Bayly, C. I., Gould, I. R., Merz, K. M., Ferguson, D. M., ... & Kollman, P. A. (1995). A second generation force field for the simulation of proteins, nucleic acids, and organic molecules. *Journal of the American Chemical Society*, *117*(19), 5179-5197.

Cuenot, S., Frétigny, C., Demoustier-Champagne, S., & Nysten, B. (2004). Surface tension effect on the mechanical properties of nanomaterials measured by atomic force microscopy. *Physical Review B*, *69*(16), 165410.

Dingreville, R., Qu, J., & Cherkaoui, M. (2005). Surface free energy and its effect on the elastic behavior of nano-sized particles, wires and films. *Journal of the Mechanics and Physics of Solids*, *53*(8), 1827-1854.

Eringen, A. C. (1983). On differential equations of nonlocal elasticity and solutions of screw dislocation and surface waves. *Journal of applied physics*, *54*(9), 4703-4710.

Evgrafov, A., Maute, K., Yang, R. G., & Dunn, M. L. (2009). Topology optimization for nano-scale heat transfer. *International journal for numerical methods in engineering*, *77*(2), 285.

Farajpour, A., Dehghany, M., & Shahidi, A. R. (2013). Surface and nonlocal effects on the axisymmetric buckling of circular graphene sheets in thermal environment. *Composites Part B: Engineering*, *50*, 333-343.

Fischer, P., Klassen, M., Mergheim, J., Steinmann, P., & Müller, R. (2011). Isogeometric analysis of 2D gradient elasticity. *Computational Mechanics*, *47*(3), 325-334.

Glavardanov, V. B., Spasic, D. T., & Atanackovic, T. M. (2012). Stability and

optimal shape of Pflüger micro/nano beam. *International Journal of Solids and Structures*, *49*(18), 2559-2567.

Gosálbez-Martínez, D., Palacios, J. J., & Fernández-Rossier, J. (2011). Spin-orbit interaction in curved graphene ribbons. *Physical Review B*, *83*(11), 115436.

Gurtin, M. E., & Murdoch, A. I. (1975). A continuum theory of elastic material surfaces. *Archive for Rational Mechanics and Analysis*, *57*(4), 291-323.

He, J., & Lilley, C. M. (2008). Surface effect on the elastic behavior of static bending nanowires. *Nano Letters*, *8*(7), 1798-1802.

Hu, Y. G., Liew, K. M., Wang, Q., He, X. Q., & Yakobson, B. I. (2008). Nonlocal shell model for elastic wave propagation in single-and double-walled carbon nanotubes. *Journal of the Mechanics and Physics of Solids*, *56*(12), 3475-3485.

Hu, K. M., Zhang, W. M., Zhong, Z. Y., Peng, Z. K., & Meng, G. (2014). Effect of surface layer thickness on buckling and vibration of nonlocal nanowires. *Physics Letters A*, *378*(7), 650-654.

Hughes, T. J., Cottrell, J. A., & Bazilevs, Y. (2005). Isogeometric analysis: CAD, finite elements, NURBS, exact geometry and mesh refinement. *Computer methods in applied mechanics and engineering*, *194*(39), 4135-4195.

Jang, H. L., & Cho, S. Adjoint shape design sensitivity analysis of molecular dynamics for lattice structures using GLE impedance forces. *International Journal of Mechanics and Materials in Design*, 1-19.

Jing, G. Y., Duan, H., Sun, X. M., Zhang, Z. S., Xu, J., Li, Y. D., ... & Yu, D. P. (2006). Surface effects on elastic properties of silver nanowires: contact atomic-force microscopy. *Physical Review B*, *73*(23), 235409.

Jin, Y., & Yuan, F. G. (2005a). Nanoscopic modeling of fracture of 2D graphene systems. *Journal of nanoscience and nanotechnology*, *5*(4), 601-608.

Jin, Y., & Yuan, F. G. (2005b). Atomistic simulations of J-integral in 2D graphene nanosystems. *Journal of nanoscience and nanotechnology*, *5*(12), 2099-2107.

Kiendl, J., Schmidt, R., Wüchner, R., & Bletzinger, K. U. (2014). Isogeometric shape optimization of shells using semi-analytical sensitivity analysis and

sensitivity weighting. *Computer Methods in Applied Mechanics and Engineering*, *274*, 148-167.

Kolesnikov, D. V., & Osipov, V. A. (2008). Electronic structure of negatively curved graphene. *JETP letters*, *87*(8), 419-422.

Kosynkin, D. V., Higginbotham, A. L., Sinitskii, A., Lomeda, J. R., Dimiev, A., Price, B. K., & Tour, J. M. (2009). Longitudinal unzipping of carbon nanotubes to form graphene nanoribbons. *Nature*, *458*(7240), 872-876.

Lam, D. C. C., Yang, F., Chong, A. C. M., Wang, J., & Tong, P. (2003). Experiments and theory in strain gradient elasticity. *Journal of the Mechanics and Physics of Solids*, *51*(8), 1477-1508.

Lee, S. W., & Cho, S. (2015). Isogeometric configuration design optimization of built-up structures. *Structural and Multidisciplinary Optimization*, *51*(2), 319-331.

Li, X. F., Wang, B. L., & Lee, K. Y. (2009). Size effects of the bending stiffness of nanowires. *Journal of Applied Physics*, *105*(7), 074306.

Li, X. F., Zhang, H., & Lee, K. Y. (2014). Dependence of Young′ s modulus of nanowires on surface effect. *International Journal of Mechanical Sciences*, *81*, 120-125.

Liu, C., & Rajapakse, R. K. N. D. (2010). Surface Energy Incorporated Continuum Models for Static and Dynamic Response of Nanoscale Beams. *IEEE Trans. Nanotechnol*, *9*(4), 422-431.

McGrail, S. D. (2011). Promising, contesting and abandoning nanotechnology: dynamics of unrealised promises, expectations, and engagement with nanotechnology in the Australian context.

Miller, R. E., & Shenoy, V. B. (2000). Size-dependent elastic properties of nanosized structural elements. *Nanotechnology*, *11*(3), 139.

Mindlin, R. D., & Tiersten, H. F. (1962). Effects of couple-stresses in linear

elasticity. *Archive for Rational Mechanics and Analysis*, *11*(1), 415-448.

Naghdi, P. M. (1973). The theory of shells and plates. In *Linear Theories of Elasticity and Thermoelasticity* (pp. 425-640). Springer Berlin Heidelberg.

Nanthakumar, S. S., Valizadeh, N., Park, H. S., & Rabczuk, T. (2015). Surface effects on shape and topology optimization of nanostructures. *Computational Mechanics*, *56*(1), 97-112.

Roh, H. Y., & Cho, M. (2004). The application of geometrically exact shell elements to B-spline surfaces. *Computer methods in applied mechanics and engineering*, *193*(23), 2261-2299.

Rudraraju, S., Van der Ven, A., & Garikipati, K. (2014). Three-dimensional isogeometric solutions to general boundary value problems of Toupin's gradient elasticity theory at finite strains. *Computer Methods in Applied Mechanics and Engineering*, *278*, 705-728.

Ryerson, C. C. (2013). *Icing Management for Coast Guard Assets* (No. ERDC/CRREL-TR-13-7). ENGINEER RESEARCH AND DEVELOPMENT CENTER HANOVER NH COLD REGIONS RESEARCH AND ENGINEERING LAB.

Sandia National Laboratories, 2009. LAMMPS : large-scale atom molecular massively parallel simulator, Sandia National Laboratories: <http://lammps.sandia.gov>

Steigmann, D. J., & Ogden, R. W. (1999, February). Elastic surface—substrate interactions. In *Proceedings of the Royal Society of London A: Mathematical, Physical and Engineering Sciences* (Vol. 455, No. 1982, pp. 437-474). The Royal Society.

Tsai, J. L., Tzeng, S. H., & Tzou, Y. J. (2010). Characterizing the fracture parameters of a graphene sheet using atomistic simulation and continuum mechanics. *International Journal of Solids and Structures*, *47*(3), 503-509.

Tsai, J. L., & Sie, M. J. (2015). Characterizing the Stress Intensity Factor of Graphene Sheet with Central Crack. *Journal of nanoscience and nanotechnology*, *15*(5), 3764-3772.

Wang, Z. Q., Zhao, Y. P., & Huang, Z. P. (2010). The effects of surface tension on the elastic properties of nano structures. *International journal of engineering science*, *48*(2), 140-150.

Yebra, D. M., Kiil, S., & Dam-Johansen, K. (2004). Antifouling technology—past, present and future steps towards efficient and environmentally friendly antifouling coatings. *Progress in organic coatings*, *50*(2), 75-104.

Yoon, M., Ha, S. H., & Cho, S. (2013). Isogeometric shape design optimization of heat conduction problems. *International Journal of Heat and Mass Transfer*, *62*, 272-285.

Zhang, C., Zhu, J., Chen, W., & Zhang, C. (2014). Two-dimensional theory of piezoelectric shells considering surface effect. *European Journal of Mechanics-A/Solids*, *43*, 109-117.

APPENDIX A

Exact optimal solution considering surface effects

Parabolic arch

Strain energy of parabolic arch considering surface effects is given as

$$U = \int_0^l \frac{N^2}{2\left(EA + 4\mu_0 + 2\lambda_0\right)} ds. \tag{A.1}$$

Infinitesimal length of parabola is obtained as

$$ds = \sqrt{1 + \frac{64h^2}{L^4} x^2}\, dx \quad \left(\text{where } y(x) = \frac{4h}{L^2} x^2,\ \frac{dy}{dx} = \frac{8h}{L^2} x \right). \tag{A.2}$$

Horizontal and vertical components of axial force N are given as, respectively,

$$N_h(x) = -\frac{qL^2}{8h} \tag{A.3}$$

and

$$N_v(x) = qx. \tag{A.4}$$

Additionally, considering normal force caused by residual surface stress τ_0 yields

$$N(x) = \sqrt{N_h^2(x) + N_v^2(x)} + 2\tau_0 = \sqrt{\frac{q^2 L^4}{64h^2} + q^2 x^2} + 2\tau_0. \tag{A.5}$$

Embedding the equation (A.2) and (A.5) into equation (A.1) yields

$$U(h) = \frac{1}{2\left(EA + 4\mu_0 + 2\lambda_0\right)} \int_{-L/2}^{L/2} \left(\sqrt{\frac{q^2 L^4}{64h^2} + q^2 x^2} + 2\tau_0 \right)^2 \sqrt{1 + \frac{64h^2}{L^4} x^2}\, dx$$

$$= \frac{1}{2\left(EA + 4\mu_0 + 2\lambda_0\right)} \tilde{U}(h) \tag{A.6}$$

Taking L=2D in equation (C.6), $\tilde{U}(h)$ can be represented as

$$\tilde{U}(h)=\int_{x=-D}^{D}\left(\sqrt{\frac{q^2D^4}{4h^2}+q^2x^2}+2\tau_0\right)^2\sqrt{1+\frac{4h^2x^2}{D^4}}dx$$

$$=\int_{x=-D}^{D}\left[\left(\frac{q^2D^4}{4h^2}+q^2x^2\right)\sqrt{1+\frac{4h^2x^2}{D^4}}\right]dx$$

$$+\int_{x=-D}^{D}\left[4\tau_0\sqrt{\frac{q^2D^4}{4h^2}+q^2x^2}\sqrt{1+\frac{4h^2x^2}{D^4}}+4\tau_0^2\sqrt{1+\frac{4h^2x^2}{D^4}}\right]dx$$

$$=q^2D^3\tilde{U}_1(h)+4\tau_0qD^2\tilde{U}_2(h)+4\tau_0^2D\tilde{U}_3(h), \tag{A.7}$$

where

$$\tilde{U}_1(h)=\frac{\left(\sqrt{1+4h^2}\left(16h^3+10h\right)+3\sinh^{-1}(2h)\right)}{32h^3}, \tag{A.8}$$

$$\tilde{U}_2(h)=\frac{4}{3}h+\frac{1}{h}, \tag{A.9}$$

and

$$\tilde{U}_3(h)=\sqrt{1+4h^2}+\frac{\sinh^{-1}(2h)}{2h}. \tag{A.10}$$

The optimal height is determined numerically by the stationary point of equation (A.7), and the derivative of strain energy with respect to h is given as

$$\frac{\partial\tilde{U}(h)}{\partial h}=q^2D^3\frac{\partial\tilde{U}_1(h)}{\partial h}+4\tau_0qD^2\frac{\partial\tilde{U}_2(h)}{\partial h}+4\tau_0^2D\frac{\partial\tilde{U}_3(h)}{\partial h}, \tag{A.11}$$

where

$$\frac{\partial\tilde{U}_1(h)}{\partial h}=\frac{\left(64h^5-40h^3-14h\right)-9\sinh^{-1}(2h)\sqrt{1+4h^2}}{\left(32h^4\right)\sqrt{1+4h^2}}, \tag{A.12}$$

$$\frac{\partial\tilde{U}_2(h)}{\partial h}=\frac{4}{3}-\frac{1}{h^2}, \tag{A.13}$$

and

$$\frac{\partial \tilde{U}_3(h)}{\partial h} = \frac{1}{\sqrt{1+4h^2}}\left(4h+\frac{1}{h}\right) - \frac{1}{2h^2}\sinh^{-1}(2h). \tag{A.14}$$

Circular arch

Reaction forces are determined from the moment equilibrium. Axial force, shear force and moment are obtained from these reaction forces.

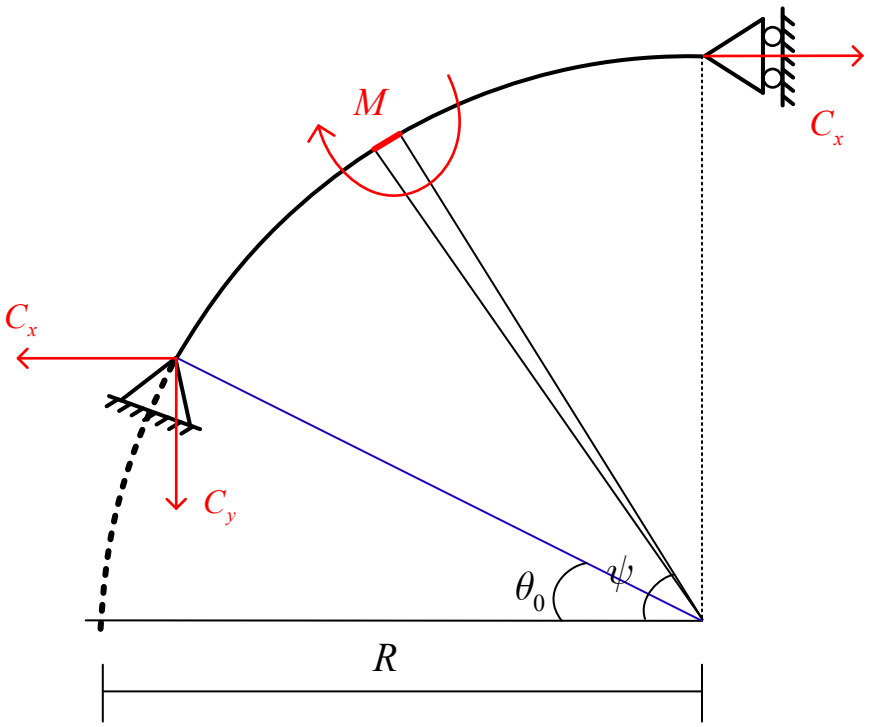

Figure A.1 Equilibrium of circular arch shell

Moment equilibrium at the left end can be represented as equation (A.15) and reaction force C_x can be written as equation (A.16).

$$C_x R(1-\sin\theta_0) - \int_{\theta_0}^{\pi/2} wRd\psi R(\cos\theta_0 - \cos\psi) = 0, \tag{A.15}$$

$$C_x = wR(T-1), \tag{A.16}$$

where

$$T = \cos\theta_0\left(\frac{\pi}{2} - \theta_0\right) / \left(1 - \sin\theta_0\right) \tag{A.17}$$

and

$$\theta_0 = \left(\frac{R - R_c}{2R}\right)\pi. \tag{A.18}$$

R_c is the radius for criteria makes θ_0 becomes zero. Moment equilibrium at the right end and reaction force C_y are given as

$$C_y R\cos\theta_0 - C_x R\left(1 - \sin\theta_0\right) - \int_{\theta_0}^{\pi/2} wRd\psi R\left(\cos\psi\right) = 0, \tag{A.19}$$

and

$$C_y = wR\left(\frac{\pi}{2} - \theta_0\right). \tag{A.20}$$

The axial force can be obtained from the force equilibrium equation as follows:

$$\begin{aligned} N &= -C_x\sin\psi - C_y\cos\psi + \int_{\theta_0}^{\psi} wR\cos\psi da + 2\tau_0 \\ &= wR\left[\left(1 - T\right)\sin\psi + \left(\psi - \frac{\pi}{2}\right)\cos\psi\right] + 2\tau_0 \end{aligned} \tag{A.21}$$

The moment can be obtained from the moment equilibrium equation as follows:

$$\begin{aligned} M &= C_y R\left(\cos\theta_0 - \cos\psi\right) - C_x R\left(\sin\psi - \sin\theta_0\right) \\ &- \int_{\theta_0}^{\psi} wRdaR\left(\cos a - \cos\psi\right) = wR^2\left[\left(1 - \sin\psi\right)T + \cos\psi\left(\psi - \frac{\pi}{2}\right)\right]. \end{aligned} \tag{A.22}$$

The shear force can be obtained from the force equilibrium equation as follows:

$$\begin{aligned} V &= -C_x\cos\psi + C_y\sin\psi - \int_{\theta_0}^{\psi} wR\sin\psi d\psi \\ &= wR\left[\left(1 - T\right)\cos\psi + \left(\frac{\pi}{2} - \psi\right)\sin\psi\right]. \end{aligned} \tag{A.23}$$

Embedding the derived N,M,V into strain energy equation yields

$$U = U_m + U_b + U_s = \int_0^l \frac{N^2}{2(EA + C_N)} ds + \int_0^l \frac{M^2}{2(EI + C_M)} ds$$

$$+ \int_0^l \frac{V^2}{2(GA_t + C_V)} ds = \frac{w^2 R^3}{2(EA + C_N)} [\alpha_m + \beta_m + \gamma_m + \tau_m]$$

$$+ \frac{w^2 R^5}{2(EI + C_M)} [\alpha_b + \beta_b + \gamma_b] + \frac{w^2 R^3}{2(GA_t + C_V)} [\alpha_s + \beta_s + \gamma_s], \quad \text{(A.24)}$$

where

$$C_N = 4\mu_0 + 2\lambda_0,\ C_M = \frac{h^2}{2}(2\mu_0 + \lambda_0),\ C_V = \mu_0, \quad \text{(A.25)}$$

$$\alpha_m = (1-T)^2 \int_{\theta_0}^{\frac{\pi}{2}} [\sin^2 \psi] d\psi = \frac{(1-T)^2}{4} (-2\theta_0 + \sin(2\theta_0) + \pi), \quad \text{(A.26)}$$

$$\beta_m = \int_{\theta_0}^{\frac{\pi}{2}} \left[\cos^2 \psi \left(\psi - \frac{\pi}{2} \right)^2 \right] d\psi$$

$$= \frac{1}{48} \left((\pi - 2\theta_0)^3 - 3\left((\pi - 2\theta_0)^2 - 2 \right) \sin(2\theta_0) + 6(\pi - 2\theta_0) \cos(2\theta_0) \right), \quad \text{(A.27)}$$

$$\gamma_m = 2(1-T) \int_{\theta_0}^{\frac{\pi}{2}} \left[\left(\psi - \frac{\pi}{2} \right) \sin\psi \cos\psi \right] d\psi$$

$$= \frac{(1-T)}{4} (-\sin(2\theta_0) - (\pi - 2\theta_0) \cos(2\theta_0)), \quad \text{(A.28)}$$

$$\tau_m = \frac{4\tau_0^2}{w^2 R^2} \left(\frac{\pi}{2} - \theta_0 \right) + \frac{4\tau_0}{wR} \left[\frac{1}{2} (\pi - 2\theta_0) \sin\theta_0 - T \cos\theta_0 \right], \quad \text{(A.29)}$$

$$\alpha_b = T^2 \int_{\theta_0}^{\frac{\pi}{2}} [(1 - \sin\psi)^2] d\psi = \frac{T^2}{4} (-6\theta_0 + \sin(2\theta_0) - 8\cos\theta_0 + 3\pi), \quad \text{(A.30)}$$

$$\beta_b = \int_{\theta_0}^{\frac{\pi}{2}} \left[\cos^2 \psi \left(\psi - \frac{\pi}{2} \right)^2 \right] d\psi$$

$$= \frac{1}{48} \left((\pi - 2\theta_0)^3 - 3\left((\pi - 2\theta_0)^2 - 2 \right) \sin(2\theta_0) + 6(\pi - 2\theta_0) \cos(2\theta_0) \right), \quad \text{(A.31)}$$

$$\gamma_b = 2T\int_{\theta_0}^{\frac{\pi}{2}}\left[(1-\sin\psi)\cos\psi\left(\psi-\frac{\pi}{2}\right)\right]d\psi$$

$$= \frac{T}{4}\Big(2\big(\sin\theta_0-4\big)\cos\theta_0+\big(\pi-2\theta_0\big)\big(4\sin\theta_0+\cos\big(2\theta_0\big)\big)\Big), \tag{A.32}$$

$$\alpha_s = (1-T)^2\int_{\theta_0}^{\frac{\pi}{2}}\left[\cos^2\psi\right]d\psi = \frac{(1-T)^2}{4}\left(-2\theta_0-2\sin\theta_0\cos\theta_0+\pi\right), \tag{A.33}$$

$$\beta_s = \int_{\theta_0}^{\frac{\pi}{2}}\left[\sin^2\psi\left(\frac{\pi}{2}-\psi\right)^2\right]d\psi$$

$$= \frac{1}{48}\Big(\big(\pi-2\theta_0\big)^3+3\Big(\big(\pi-2\theta_0\big)^2-2\Big)\sin\big(2\theta_0\big)-6\big(\pi-2\theta_0\big)\cos\big(2\theta_0\big)\Big), \tag{A.34}$$

and

$$\gamma_s = 2\big(1-T\big)\int_{\theta_0}^{\frac{\pi}{2}}\left[\left(\frac{\pi}{2}-\psi\right)\sin\psi\cos\psi\right]d\psi$$

$$= \frac{(1-T)}{4}\big(\sin\big(2\theta_0\big)+\big(\pi-2\theta_0\big)\cos\big(2\theta_0\big)\big), \tag{A.35}$$

The optimal curvature is determined numerically by the stationary point of equation (D.24), and the derivative of strain energy with respect to κ is given as

$$\frac{\partial U}{\partial\kappa} = \frac{\partial U}{\partial R}\frac{\partial R}{\partial\kappa} = \left(\frac{\partial U_m}{\partial R}+\frac{\partial U_b}{\partial R}+\frac{\partial U_s}{\partial R}\right)\left(-R^2\right), \tag{A.36}$$

where

$$\frac{\partial U_m}{\partial R} = \frac{3w^2R^2}{2\big(EA+C_N\big)}\big[\alpha_m+\beta_m+\gamma_m\big]$$

$$+\frac{w^2R^3}{2\big(EA+C_N\big)}\left[\frac{\partial\alpha_m}{\partial R}+\frac{\partial\beta_m}{\partial R}+\frac{\partial\gamma_m}{\partial R}+\frac{\partial\tau_m}{\partial R}\right], \tag{A.37}$$

$$\frac{\partial U_b}{\partial R} = \frac{5w^2R^4}{2\big(EI+C_M\big)}\big[\alpha_b+\beta_b+\gamma_b\big]$$

$$+\frac{w^2R^5}{2(EI+C_M)}\left[\frac{\partial\alpha_b}{\partial R}+\frac{\partial\beta_b}{\partial R}+\frac{\partial\gamma_b}{\partial R}\right], \tag{A.38}$$

$$\frac{\partial U_s}{\partial R}=\frac{3w^2R^2}{2(GA_t+C_V)}[\alpha_s+\beta_s+\gamma_s]$$

$$+\frac{w^2R^3}{2(GA_t+C_V)}\left[\frac{\partial\alpha_s}{\partial R}+\frac{\partial\beta_s}{\partial R}+\frac{\partial\gamma_s}{\partial R}\right], \tag{A.39}$$

$$\frac{\partial\alpha_m}{\partial R}=\frac{(T-1)}{2}(-2\theta_0+\sin(2\theta_0)+\pi)\frac{\partial T}{\partial R}$$

$$+\frac{(1-T)^2}{4}(-2+2\cos(2\theta_0))\frac{\partial\theta_0}{\partial R}, \tag{A.40}$$

$$\frac{\partial\beta_m}{\partial R}=\frac{-1}{8}(\pi-2\theta_0)^2(1+\cos(2\theta_0))\frac{\partial\theta_0}{\partial R}, \tag{A.41}$$

$$\frac{\partial\gamma_m}{\partial R}=\frac{-1}{4}[-\sin(2\theta_0)-\pi\cos(2\theta_0)+2\theta_0\cos(2\theta_0)]\frac{\partial T}{\partial R}$$

$$+\frac{(1-T)}{2}(\pi-2\theta_0)\sin(2\theta_0)\frac{\partial\theta_0}{\partial R}, \tag{A.42}$$

$$\frac{\partial\tau_m}{\partial R}=\frac{-8\tau_0^2}{w^2R^3}\left(\frac{\pi}{2}-\theta_0\right)-\frac{4\tau_0^2}{w^2R^2}\frac{\partial\theta_0}{\partial R}-\frac{4\tau_0}{wR^2}\left[\frac{1}{2}(\pi-2\theta_0)\sin\theta_0-T\cos\theta_0\right]$$

$$+\frac{4\tau_0}{wR}\left[-\sin\theta_0+\frac{1}{2}(\pi-2\theta_0)\cos\theta_0+T\sin\theta_0\right]\frac{\partial\theta_0}{\partial R}, \tag{A.43}$$

$$\frac{\partial\alpha_b}{\partial R}=\frac{T}{2}(-6\theta_0+\sin(2\theta_0)-8\cos\theta_0+3\pi)\frac{\partial T}{\partial R}$$

$$+\frac{T^2}{4}(-6+2\cos(2\theta_0)+8\sin\theta_0)\frac{\partial\theta_0}{\partial R}, \tag{A.44}$$

$$\frac{\partial\beta_b}{\partial R}=\frac{-1}{8}(\pi-2\theta_0)^2(\cos(2\theta_0)+1)\frac{\partial\theta_0}{\partial R}, \tag{A.45}$$

$$\frac{\partial\gamma_b}{\partial r}=\frac{1}{4}[2(\sin\theta_0-4)\cos\theta_0+(\pi-2\theta_0)(4\sin\theta_0+\cos(2\theta_0))]\frac{\partial T}{\partial R}$$

$$+\frac{T}{4}(\pi-2\theta_0)(4\cos\theta_0-2\sin(2\theta_0))\frac{\partial\theta_0}{\partial R}, \tag{A.46}$$

$$\frac{\partial\alpha_s}{\partial R}=\frac{(T-1)}{2}(-2\theta_0-2\sin\theta_0\cos\theta_0+\pi)\frac{\partial T}{\partial R}$$

$$+\frac{(1-T)^2}{4}\left(-2-2\cos\left(2\theta_0\right)\right)\frac{\partial\theta_0}{\partial R}, \tag{A.47}$$

$$\frac{\partial\beta_s}{\partial R}=\frac{1}{8}\left(\pi-2\theta_0\right)^2\left(\cos\left(2\theta_0\right)-1\right)\frac{\partial\theta_0}{\partial R}, \tag{A.48}$$

$$\frac{\partial\gamma_s}{\partial R}=\frac{(-1)}{4}\left(\sin\left(2\theta_0\right)+\left(\pi-2\theta_0\right)\cos\left(2\theta_0\right)\right)\frac{\partial T}{\partial R}$$
$$+\frac{(T-1)}{2}\left(\pi-2\theta_0\right)\sin\left(2\theta_0\right)\frac{\partial\theta_0}{\partial R}, \tag{A.49}$$

$$\frac{\partial T}{\partial R}=\frac{\pi\left(\frac{\pi}{2}-\theta_0-\cos\theta_0\right)}{R^2\left(1-\sin\theta_0\right)}, \tag{A.50}$$

and

$$\frac{\partial\theta_0}{\partial R}=\frac{\pi}{R^2}. \tag{A.51}$$

APPENDIX B

Exact optimal solution considering nonlocal effects

Circular arch

Reaction forces are determined from the moment equilibrium. Axial force, shear force and moment are obtained from these reaction forces as shown in Figure A.1. Moment equilibrium at the left end can be represented as equation (B.1) and reaction force C_x can be written as equation (B.2).

$$C_x R\left(1-\sin\theta_0\right)-\int_{\theta_0}^{\pi/2} wRd\psi R\left(\cos\theta_0-\cos\psi\right)=0, \tag{B.1}$$

$$C_x = wR\left(T-1\right)-\frac{1}{R}\mu w \tag{B.2}$$

where

$$T=\cos\theta_0\left(\frac{\pi}{2}-\theta_0\right)/\left(1-\sin\theta_0\right) \tag{B.3}$$

and

$$\theta_0=\left(\frac{R-R_c}{2R}\right)\pi. \tag{B.4}$$

R_c is the radius for criteria makes θ_0 becomes zero. Moment equilibrium at the right end and reaction force C_y are given as

$$C_y R\cos\theta_0 - C_x R\left(1-\sin\theta_0\right)$$

$$-\int_{\theta_0}^{\pi/2} wRd\psi R\left(\cos\psi\right)+\mu w\left(1-\sin\theta_0\right)=0, \tag{B.5}$$

and

$$C_y = wR\left(\frac{\pi}{2}-\theta_0\right). \tag{B.6}$$

The axial force can be obtained from the force equilibrium equation as follows:

$$N=-C_x\sin\psi-C_y\cos\psi+\int_{\theta_0}^{\psi} wR\cos\psi da$$

$$= wR\left[(1-T)\sin\psi + \left(\psi - \frac{\pi}{2}\right)\cos\psi\right] + \frac{1}{R}\mu w \sin\psi. \tag{B.7}$$

The moment can be obtained from the moment equilibrium equation as follows:

$$M = C_y R(\cos\theta_0 - \cos\psi) - C_x R(\sin\psi - \sin\theta_0)$$

$$-wR^2\left[(\sin\psi - \sin\theta_0) - (\cos\psi)(\psi - \theta_0)\right] + \mu w \sin\psi$$

$$= wR^2\left[(1-\sin\psi)T + \cos\psi\left(\psi - \frac{\pi}{2}\right)\right] + \mu w \sin\psi. \tag{B.8}$$

The shear force can be obtained from the force equilibrium equation as follows:

$$V = -C_x \cos\psi + C_y \sin\psi - \int_{\theta_0}^{\psi} wR\sin\psi d\psi$$

$$= wR\left[(1-T)\cos\psi + \left(\frac{\pi}{2} - \psi\right)\sin\psi\right] + \frac{1}{R}\mu w \cos\psi. \tag{B.9}$$

Embedding the derived *N*,*M* and *V* into strain energy equation yields

$$U = U_m + U_b + U_s = \int_0^l \frac{N^2}{2EA} ds + \int_0^l \frac{M^2}{2EI} ds + \int_0^l \frac{V^2}{2GA_t} ds$$

$$= \frac{R}{2EA}[\alpha_m + \beta_m + \gamma_m] + \frac{R}{2EI}[\alpha_b + \beta_b + \gamma_b] + \frac{R}{2GA_t}[\alpha_s + \beta_s + \gamma_s], \tag{B.10}$$

where

$$\alpha_m = w^2R^2\left[\left\{\frac{(1-T)^2}{4}\left(-2\theta_0 + \sin(2\theta_0) + \pi\right)\right\}\right],$$

$$+w^2R^2\left[\left\{\frac{1}{48}\left((\pi - 2\theta_0)^3 - 3\left((\pi - 2\theta_0)^2 - 2\right)\sin(2\theta_0) + 6(\pi - 2\theta_0)\cos(2\theta_0)\right)\right\}\right],$$

$$+w^2R^2\left[\left\{\frac{(1-T)}{4}\left(-\sin(2\theta_0) - (\pi - 2\theta_0)\cos(2\theta_0)\right)\right\}\right], \tag{B.11}$$

$$\beta_m = \mu^2 \frac{w^2}{4R^2}\left(-2\theta_0 + \sin(2\theta_0) + \pi\right), \tag{B.12}$$

$$\gamma_m = \frac{-\mu w^2}{4}\left[(2T-2)\left(-2\theta_0+\sin(2\theta_0)+\pi\right)\right],$$

$$-\frac{\mu w^2}{4}\left[\sin(2\theta_0)+(\pi-2\theta_0)\cos(2\theta_0)\right], \tag{B.13}$$

$$\alpha_b = w^2R^4\left[\left\{\frac{T^2}{4}\left(-6\theta_0+\sin(2\theta_0)-8\cos\theta_0+3\pi\right)\right\}\right],$$

$$+w^2R^4\left[\left\{\frac{1}{48}\left((\pi-2\theta_0)^3-3\left((\pi-2\theta_0)^2-2\right)\sin(2\theta_0)+6(\pi-2\theta_0)\cos(2\theta_0)\right)\right\}\right],$$

$$+w^2R^4\left[\frac{T}{4}\left(2(\sin\theta_0-4)\cos\theta_0+(\pi-2\theta_0)\left(4\sin\theta_0+\cos(2\theta_0)\right)\right)\right], \tag{B.14}$$

$$\beta_b = \frac{\mu^2w^2}{4}\left(-2\theta_0+\sin(2\theta_0)+\pi\right), \tag{B.15}$$

$$\gamma_b = \frac{\mu w^2R^2}{4}\left(2T\left(4\cos\theta_0+2\theta_0-\sin(2\theta_0)-\pi\right)\right)$$

$$+\frac{\mu w^2R^2}{4}\left(-\sin(2\theta_0)-(\pi-2\theta_0)\cos(2\theta_0)\right), \tag{B.16}$$

$$\alpha_s = w^2R^2\left[\left\{\frac{(1-T)^2}{4}\left(-2\theta_0-2\sin\theta_0\cos\theta_0+\pi\right)\right\}\right],$$

$$+w^2R^2\left[\frac{1}{48}\left((\pi-2\theta_0)^3+3\left((\pi-2\theta_0)^2-2\right)\sin(2\theta_0)-6(\pi-2\theta_0)\cos(2\theta_0)\right)\right],$$

$$+w^2R^2\left[\frac{(1-T)}{4}\left(\sin(2\theta_0)+(\pi-2\theta_0)\cos(2\theta_0)\right)\right], \tag{B.17}$$

$$\beta_s = \frac{\mu^2w^2}{4R^2}\left(-2\theta_0-2\sin\theta_0\cos\theta_0+\pi\right), \tag{B.18}$$

$$\gamma_s = \mu w^2(1-T)\left(-\theta_0-\sin\theta_0\cos\theta_0+\frac{\pi}{2}\right)$$

$$+\frac{\mu w^2}{4}\left(\sin(2\theta_0)+(\pi-2\theta_0)\cos(2\theta_0)\right). \tag{B.19}$$

The optimal curvature is determined numerically by the stationary point of equation (B.10), and the derivative of strain energy with respect to κ is given

as

$$\frac{\partial U}{\partial \kappa}=\frac{\partial U}{\partial R}\frac{\partial R}{\partial \kappa}=\left(\frac{\partial U_m}{\partial R}+\frac{\partial U_b}{\partial R}+\frac{\partial U_s}{\partial R}\right)\left(-R^2\right), \tag{B.20}$$

where

$$\begin{aligned}\frac{dU}{dR}=&\frac{1}{2EA}\left[\alpha_m+\beta_m+\gamma_m\right]+\frac{1}{2EI}\left[\alpha_b+\beta_b+\gamma_b\right]+\frac{1}{2GA_t}\left[\alpha_s+\beta_s+\gamma_s\right]\\&+\frac{R}{2EA}\left[\frac{d\alpha_m}{dR}+\frac{d\beta_m}{dR}+\frac{d\gamma_m}{dR}\right]+\frac{R}{2EI}\left[\frac{d\alpha_b}{dR}+\frac{d\beta_b}{dR}+\frac{d\gamma_b}{dR}\right]\\&+\frac{R}{2GA_t}\left[\frac{d\alpha_s}{dR}+\frac{d\beta_s}{dR}+\frac{d\gamma_s}{dR}\right]\end{aligned} \tag{B.21}$$

$$\frac{d\alpha_m}{dR}=\frac{\partial\alpha_m}{\partial R}+\frac{\partial\alpha_m}{\partial\theta_0}\frac{\partial\theta_0}{\partial R}+\frac{\partial\alpha_m}{\partial T}\frac{\partial T}{\partial R} \tag{B.22}$$

$$\begin{aligned}\frac{\partial\alpha_m}{\partial\theta_0}=&w^2R^2\left[\left\{\frac{(1-T)^2}{4}\left(-2+2\cos(2\theta_0)\right)\right\}-\left\{\frac{1}{8}(\pi-2\theta_0)^2\left(1+\cos(2\theta_0)\right)\right\}\right],\\&+w^2R^2\left[\left\{\frac{(1-T)}{2}\left((\pi-2\theta_0)\sin(2\theta_0)\right)\right\}\right],\end{aligned} \tag{B.23}$$

$$\begin{aligned}\frac{\partial\alpha_m}{\partial T}=&w^2R^2\left[\left\{\frac{(T-1)}{2}\left(-2\theta_0+\sin(2\theta_0)+\pi\right)\right\}\right],\\&+w^2R^2\left[\left\{\frac{1}{4}\left(\sin(2\theta_0)+(\pi-2\theta_0)\cos(2\theta_0)\right)\right\}\right],\end{aligned} \tag{B.24}$$

$$\frac{d\beta_m}{dR}=\frac{\partial\beta_m}{\partial R}+\frac{\partial\beta_m}{\partial\theta_0}\frac{\partial\theta_0}{\partial R} \tag{B.25}$$

$$\frac{\partial\beta_m}{\partial R}=-\mu^2\frac{w^2}{2R^3}\left(-2\theta_0+\sin(2\theta_0)+\pi\right), \tag{B.26}$$

$$\frac{\partial\beta_m}{\partial\theta_0}=\mu^2\frac{w^2}{4R^2}\left(-2+2\cos(2\theta_0)\right), \tag{B.27}$$

$$\frac{d\gamma_m}{dR}=\frac{\partial\gamma_m}{\partial\theta_0}\frac{\partial\theta_0}{\partial R}+\frac{\partial\gamma_m}{\partial T}\frac{\partial T}{\partial R} \tag{B.28}$$

$$\frac{\partial\gamma_m}{\partial\theta_0}=-\frac{\mu w^2}{4}\left[(2T-2)\left(-2+2\cos(2\theta_0)\right)-2(\pi-2\theta_0)\sin(2\theta_0)\right], \tag{B.29}$$

$$\frac{\partial \gamma_m}{\partial T} = \frac{-\mu w^2}{2}\left(-2\theta_0 + \sin\left(2\theta_0\right) + \pi\right), \tag{B.30}$$

$$\frac{d\alpha_b}{dR} = \frac{\partial \alpha_b}{\partial R} + \frac{\partial \alpha_b}{\partial \theta_0}\frac{\partial \theta_0}{\partial R} + \frac{\partial \alpha_b}{\partial T}\frac{\partial T}{\partial R} \tag{B.31}$$

$$\frac{\partial \alpha_b}{\partial \theta_0} = w^2 R^4\left[\frac{T^2}{4}\left(-6 + 2\cos\left(2\theta_0\right) + 8\sin\theta_0\right) - \frac{1}{8}\left(\left(\pi - 2\theta_0\right)^2\left(\cos\left(2\theta_0\right) + 1\right)\right)\right],$$

$$+ w^2 R^4\left[\frac{T}{4}\left(\pi - 2\theta_0\right)\left(4\cos\theta_0 - 2\sin\left(2\theta_0\right)\right)\right], \tag{B.32}$$

$$\frac{\partial \alpha_b}{\partial T} = w^2 R^4\left[\frac{T}{2}\left(-6\theta_0 + \sin\left(2\theta_0\right) - 8\cos\theta_0 + 3\pi\right)\right],$$

$$+ w^2 R^4\left[\frac{1}{4}\left(2\left(\sin\theta_0 - 4\right)\cos\theta_0 + \left(\pi - 2\theta_0\right)\left(4\sin\theta_0 + \cos\left(2\theta_0\right)\right)\right)\right], \tag{B.33}$$

$$\frac{d\beta_b}{dR} = \frac{\mu^2 w^2}{4}\left(-2 + 2\cos\left(2\theta_0\right)\right)\frac{\partial \theta_0}{\partial R} \tag{B.34}$$

$$\frac{d\gamma_b}{dR} = \frac{\partial \gamma_b}{\partial R} + \frac{\partial \gamma_b}{\partial \theta_0}\frac{\partial \theta_0}{\partial R} + \frac{\partial \gamma_b}{\partial T}\frac{\partial T}{\partial R} \tag{B.35}$$

$$\frac{\partial \gamma_b}{\partial \theta_0} = \frac{\mu w^2 R^2}{4}\left(2T\left(-4\sin\theta_0 + 2 - 2\cos\left(2\theta_0\right)\right)\right)$$

$$+ \frac{\mu w^2 R^2}{4}\left(2\left(\pi - 2\theta_0\right)\sin\left(2\theta_0\right)\right), \tag{B.36}$$

$$\frac{\partial \gamma_b}{\partial T} = \frac{\mu w^2 R^2}{2}\left(4\cos\theta_0 + 2\theta_0 - \sin\left(2\theta_0\right) - \pi\right) \tag{B.37}$$

$$\frac{d\alpha_s}{dR} = \frac{\partial \alpha_s}{\partial R} + \frac{\partial \alpha_s}{\partial \theta_0}\frac{\partial \theta_0}{\partial R} + \frac{\partial \alpha_s}{\partial T}\frac{\partial T}{\partial R} \tag{B.38}$$

$$\frac{\partial \alpha_s}{\partial \theta_0} = w^2 R^2\left[\frac{\left(1-T\right)^2}{4}\left(-2 - 2\cos\left(2\theta_0\right)\right) + \frac{1}{8}\left(\pi - 2\theta_0\right)^2\left(\cos\left(2\theta_0\right) - 1\right)\right]$$

$$- w^2 R^2\left[\frac{\left(1-T\right)}{2}\left(\pi - 2\theta_0\right)\sin\left(2\theta_0\right)\right] \tag{B.39}$$

$$\frac{\partial \alpha_s}{\partial T} = w^2 R^2\left[\frac{\left(T-1\right)}{2}\left(-2\theta_0 - 2\sin\theta_0\cos\theta_0 + \pi\right)\right],$$

$$-w^2R^2\left[\frac{1}{4}\left\{\sin(2\theta_0)+(\pi-2\theta_0)\cos(2\theta_0)\right\}\right], \tag{B.40}$$

$$\frac{d\beta_s}{dR}=\frac{\partial\beta_s}{\partial R}+\frac{\partial\beta_s}{\partial\theta_0}\frac{\partial\theta_0}{\partial R} \tag{B.41}$$

$$\frac{\partial\beta_s}{\partial R}=\frac{\mu^2w^2}{2R^3}(2\theta_0+2\sin\theta_0\cos\theta_0-\pi), \tag{B.42}$$

$$\frac{\partial\beta_s}{\partial\theta_0}=\frac{\mu^2w^2}{4R^2}(-2-2\cos 2\theta_0), \tag{B.43}$$

$$\frac{d\gamma_s}{dR}=\frac{\partial\gamma_s}{\partial\theta_0}\frac{\partial\theta_0}{\partial R}+\frac{\partial\gamma_s}{\partial T}\frac{\partial T}{\partial R} \tag{B.44}$$

$$\frac{\partial\gamma_s}{\partial\theta_0}=-\mu w^2(1-T)(1+\cos 2\theta_0)-\frac{\mu w^2}{2}(\pi-2\theta_0)\sin(2\theta_0). \tag{B.45}$$

$$\frac{\partial\gamma_s}{\partial T}=-\mu w^2\left(-\theta_0-\sin\theta_0\cos\theta_0+\frac{\pi}{2}\right). \tag{B.46}$$

$$\frac{\partial T}{\partial R}=\frac{R_\tau\pi\left(\frac{\pi}{2}-\theta_0-\cos\theta_0\right)}{2R^2(1-\sin\theta_0)}, \tag{B.47}$$

and

$$\frac{\partial\theta_0}{\partial R}=\frac{R_\tau\pi}{2R^2}. \tag{B.48}$$

APPENDIX C

Exact stress field near the crack tip considering nonlocal effects

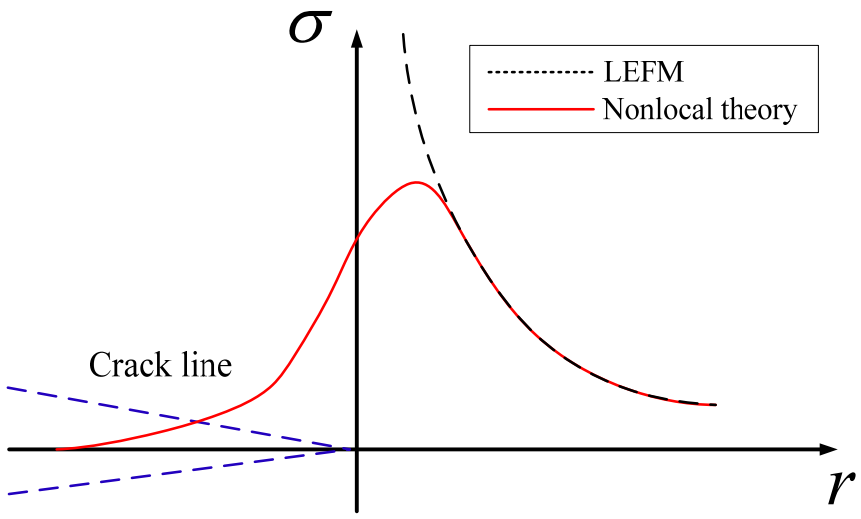

Figure C.1 Stress distribution of LEFM and nonlocal theory near the crack tip

Asymptotic solution near the crack tip is already known and stress field near the crack tip considering nonlocal effects in nanoscale can be obtained.

$$K_I = \bar{\sigma}_\infty \sqrt{\pi a} \tag{C.1}$$

where 2*a* is crack length and $\bar{\sigma}_\infty$ is distributed load per unit length. Local stress $\bar{\sigma}_{22}$ is obtained as

$$\begin{aligned} \bar{\sigma}_{22}(r,\theta) &= \frac{K_I}{\sqrt{2\pi r}} \cos\frac{\theta}{2}\left(1+\sin\frac{\theta}{2}\sin\frac{3\theta}{2}\right) \\ &= \frac{\bar{\sigma}_\infty \sqrt{a}}{\sqrt{2r}} \cos\frac{\theta}{2}\left(1+\sin\frac{\theta}{2}\sin\frac{3\theta}{2}\right) \end{aligned} \tag{C.2}$$

Nonlocal stress σ_{22} is obtained as

$$\sigma_{22}(r)=\frac{1}{2\pi l^2}\int_{R^2-l_\Sigma}\left[K_0\left(\frac{|r-r'|}{l}\right)\bar{\sigma}_{22}(r',\theta')r'\right]dr'd\theta' \tag{C.3}$$

Second order Bessel function K_0 is used as a Kernel function as

$$K_0(z)=\int_0^\infty \frac{\cos(zt)}{\sqrt{t^2+1}}dt \tag{C.4}$$

Embedding the equation (C.4) into equation (C.3) yields

$$\sigma_{22}(\xi)=\bar{\sigma}_\infty\sqrt{\frac{a}{l}}\frac{1}{2\pi\sqrt{2}}\int_0^\infty\int_{-\pi}^{\pi}\begin{pmatrix}\cos\frac{\theta}{2}\left(1+\sin\frac{\theta}{2}\sin\frac{3\theta}{2}\right)\\ \times K_0\left(|\xi-\xi'|\right)\sqrt{\xi'}\end{pmatrix}d\theta d\xi'$$

$$=\bar{\sigma}_\infty\sqrt{\frac{a}{l}}\frac{1}{2\pi\sqrt{2}}\int_0^\infty\int_{-\pi}^{\pi}\begin{pmatrix}\cos\frac{\theta}{2}\left(1+\sin\frac{\theta}{2}\sin\frac{3\theta}{2}\right)\\ \times K_0\left(\sqrt{\xi^2+\xi'^2-2\xi\xi'\cos\theta}\right)\sqrt{\xi'}\end{pmatrix}d\theta d\xi' \tag{C.5}$$

where r is a distance from the crack tip, $\xi=r/l$, $\xi'=r'/l$ and l is Nonlocal parameter. Nonlocal stress on the crack tip is obtained as

$$\sigma_{22}(0)=\bar{\sigma}_\infty\sqrt{\frac{a}{l}}\frac{4.8}{2\pi\sqrt{2}}\int_0^\infty K_0\left(\xi'\right)\sqrt{\xi'}d\xi'=0.5736\bar{\sigma}_\infty\sqrt{\frac{a}{l}} \tag{C.6}$$

To obtain the value of equation (C.5), triple integral needs to be performed numerically and it is computationally expensive. Also, asymptotic solution does not exist always on the general loading condition, so equation (C.5) is calculated only in special situation which requires exact solution. Generally, nonlocal stress field is obtained using numerical analysis given in chapter 2.3.3.

크기 효과를 고려한 연속체-나노스케일 구조물의 아이소-지오메트릭 형상 최적설계

안 승 호
산업·조선공학부
공과대학
서울대학교

초 록

최근에, 조선 해양 공학 분야를 포함한 다양한 학술 및 산업 분야에서 기존의 연속체 기반 접근법의 한계를 뛰어넘기 위한 방안으로써 원자 단위의 설계와 해석이 주목 받고 있다. 전통적으로, 나노 스케일 구조물의 거동과 물성치를 얻기 위하여 분자동역학 시뮬레이션 기법이 주로 사용되었으나 과도한 계산 시간이 필요하다는 한계점이 있었다. 특히, 분자동역학 시뮬레이션의 한계는 형상 최적 설계 분야에서 더욱 두드러진다. 원자 구조의 불연속성으로 인하여 형상 설계 민감도를 정의하기가 어려울 뿐 아니라, 반복적인 해석을 필요로 하는 최적 설계 문제를 풀기 위해서 더욱 과도한 계산 시간을 필요로 하게 된다.

본 논문에서는 나노 스케일에서의 크기 효과가 고려된 아이소-지오메트릭 형상 최적 설계 기법을 개발하였다. 나노스케일 구조물을 해석하기 위하여 크기 효과가 고려된 연속체 모델을 도입하였다. 특히, Gurtin과 Murdoch이 제안한 표면 효과를 고려한 연속체 이론과

Eringen이 제안한 비국소 효과를 고려한 연속체 이론을 각각 고려하였다. 원자 현미경을 이용한 은 나노 와이어의 굽힘 실험을 통하여 개발된 방법론을 실험적으로 검증하였다. 수치 예제에서는 연속체 기반의 Naghdi 쉘 정식화를 적용하여 곡면 구조물의 최적 설계를 수행 하였으며, 수치 해석을 위하여 아이소-지오메트릭 기법을 적용하였다. 설계 민감도를 얻기 위하여 직접 미분법을 사용 하였으며, 설계 변수는 쉘의 자유로운 형상 변화를 보장하는 NURBS의 조정점으로 하였다. 휘어진 빔 이론에 기반하여 정해를 유도 하였으며, 이를 이용하여 수치 해석 예제를 검증하였다. 나노 스케일에서의 크기 효과의 고려가 쉘 구조물의 거동 및 최적설계 결과에 미치는 영향력을 확인 하였다.

원자현미경을 이용한 은나노 와이어의 굽힘 실험을 통하여 나노 스케일에서 표면 효과의 영향력을 보였다. 실험 값과 이론 계산 값을 통하여 얻은 은나노 와이어의 거동을 비교 함으로써 일치도를 확인할 수 있었다. 실험 결과를 이용하여 은나노 와이어의 거동뿐 아니라 이의 설계 민감도를 검증하였다. 실험 값으로부터 곡선 맞춤을 얻고 이로부터 계산된 설계 민감도를 이론 값을 통해서 계산된 설계 민감도와 비교 함으로써 설계 민감도 값을 검증할 수 있었으며 좋은 일치도를 보임을 확인하였다.

아이소-지오메트릭 기법은 NURBS 기저함수의 편리성으로 인하여 기존의 유한요소 해석법에 비하여 여러 가지 이점을 갖는다. CAD에서의 NURBS 함수를 사용함에 따라 엄밀한 기하형상과 고차의 연속성을 갖는 특징 등이 응답 해석에 반영된다. 또한, 아이소-지오메트릭 방법은 법선 벡터와 곡률과 같은 고차의 기하 정보가 정확하게 반영된다. 따라서, 복잡한 기하 형상을 갖는 구조물에 대해서도 엄밀한 설계 민감도의 계산이 가능하기 때문에 곡면 구조물에서 설계 민감도를 구함에 있어 이점을 갖는다. 특히 쉘 구조물 에서는 엄밀한 기하형상의 고려가 매우 중요하게

작용하기 때문에 아이소-지오메트릭 해석법을 적용함에 따라 기존의 유한요소 해석법에 비하여 정확한 해석 결과를 얻을 수 있다.

주요어: 아이소-지오메트릭 해석법, 나노스케일, 크기 효과, 형상 설계 민감도, 형상 최적 설계, 실험적 검증

학번: 2009-21131